Structure Design and Properties Modification Based on Wrinkling of Two-Dimensional Nanomaterials

BY

SHIKAI DENG

B.E., Beijing University of Chemical Technology, 2012

DISSERTATION

Submitted as partial fulfillment of the requirements

for the degree of Doctor of Philosophy in Chemical Engineering

in the Graduate College of the

University of Illinois at Chicago, 2017

Chicago, Illinois

Defense Committee:

Dr. Vikas Berry, Chair and Advisor, Department of Chemical Engineering

Dr. Ying Liu, Department of Chemical Engineering

Dr. Brian P. Chaplin, Department of Chemical Engineering

Dr. Zheng Yang, Department of Electrical and Computer Engineering

Dr. Jiaxing Huang, Northwestern University

ACKNOWLEDGMENTS

I genuinely thank my advisor, Dr. Vikas Berry, for his encouragement, support, patience, advice, and guidance during my whole Ph.D. study period at Kansas State University, University of Illinois at Chicago, and Argonne National Laboratory. It turns out that I am the last group member of Dr. Berry group from K-State, and I still remember our first conversion in his office. I really want to thank him for leading me into this exciting research area, this work would certainly not have been possible without him.

I wish to extend my sincere appreciation to my Ph.D. committee members (Dr. Ying Liu, Dr. Brian P. Chaplin, Dr. Zheng Yang, and Dr. Jiaxing Huang) for taking time out from their busy schedules to attend my preliminary defense and final defense and for providing helpful advice. I would like to express my special thanks to Dr. Zheng Yang and Dr. Jiaxing Huang, for providing support, help and advice in my research and career.

Sincere thanks to Dr. Anirudha Sumant for providing me a wonderful research experience and opportunity at Argonne National Laboratory.

Further, I want to give my special thanks to all my collaborators (Enlai Gao, Dr. Yanlei Wang, Dr. Zhiping Xu, Soumyo Sen, Dr. Petr Král) for their contribution to my research and thesis.

I would like to thank all my colleagues from Berry Research Laboratory (Dr. Sanjay Behura, Dr. Phong Nguyen, Donovan Briggs, Songwei Che, Rousan Debbarma, Bijentimala Keisham, Kai-Chih Chang, Deisy Arrington, Yu Wen, Xin Yu, Dylan Lynch,

Cheng Wang). They provided a friendly, highly professional, and wonderful environment during my whole Ph.D. journey.

Finally, I also want to thank all my family and friends outside of research. Special thanks go to my Mom, Dad, and sister, for all the help and support they have given me over years. Their love, care, and unconditional support brought encouragement for me pursue excellence in my studies away from them. Last, but certainly not least, I really want to thank my girlfriend, Yue Liu, who always shows me the positive side of life and brings me tons of happiness and laughter to my life.

TABLE OF CONTENTS

TABLE OF CONTENTS (continued)

LIST OF FIGURES

LIST OF TABLES

LIST OF ABBREVIATIONS

2D Two-dimensional

2DNMs Two-dimensional Nanomaterials

TMDs Transition Metal Dichalcogenides

CVD Chemical Vapor Deposition

EBL Electron Beam Lithography

RIE Reactive Ion Etching

FESEM Field Emission Scanning Electron Microscopy

EDS Energy Dispersive X-ray Spectroscopy

AFM Atomic Force Microscope

TEM Transmission Electron Microscopy

SAED Selected Area Electron Diffraction

Raman Raman Spectroscopy

STM Scanning Tunneling Microscopy

PL Photoluminescence Spectroscopy

FET Field-effect Transistor

ABSTRACT

Structure and strain engineering is the process of tuning a material's properties by altering its mechanical or structural attributes. Atomically thin two-dimensional nanomaterials (2DNMs), such as graphene, boron nitride (BN), and transition metal dichalcogenides (MoS_2, WS_2, etc.), which have been extensively studied in recent years, are particularly well-suited for strain engineering because they can withstand large strains. Wrinkling has shown its great advantages to introduce well-controlled local structure and strain in 2DNMs. However, the studies on understanding of the wrinkles formation, wrinkling processes for nanoscale confined and directed wrinkles, and wrinkle-effect and application in 2DNMs are still in its infancy. This thesis first shows that parallel and self-similar hierarchical wrinkles pattern can be formed on ultrathin cobalt/chromium film atop a contracting silicone oil meniscus. Interesting, these wrinkle attributes do not follow the standard von-Kármán wrinkling scaling near the edge, attributed to the added surface energy ($L/\lambda \propto (A/t)^{0.31}$). An energy model is developed and shows a linear relation between the amplitude and the length of wrinkles at all observed hierarchic levels ($L \propto A$). Additionally, wrinkles (wavelength = 10 nm $\sim$ 10 μm) can be found in mechanical exfoliated MoS_2 flakes on silicon based substrates (SiO_2 and Si_3N_4). A mechanical energy model is proposed that equates the adhesion energy of MoS_2 on SiO_2 and Si_3N_4 to the attributes of a single wrinkle in a MoS_2 flake. The adhesion energy values of 0.170 ± 0.033 J m^{-2} for MoS_2 on SiO_2 and 0.252 ± 0.041 J m^{-2} for MoS_2 on Si_3N_4 are determined. Further, we show that selective desiccation of a bacterium under impermeable and flexible graphene via a flap-valve operation produces axially aligned graphene wrinkles of wavelength 32.4–34.3 nm, consistent with modified Föppl–von Kármán mechanics

(confinement ~0.7 × 4 μm^2). An electrophoretically oriented bacterial device with confined wrinkles aligned with van der Pauw electrodes is fabricated and exhibited an anisotropic barrier (ΔE = 1.69 meV). Finally, we show that wrinkles can induce uniaxial strain, spatially reconfigured doping distribution, phonon softening (2 cm^{-1}/% deformation for Raman E^1_{2g} mode), and reduction of the optical bandgap (40~60 meV/% deformation) in multilayer MoS_2 flakes. A larger barrier (ΔE_A= 106.6 meV) and a higher carrier mobility are exhibited in the MoS_2 devices with wrinkles in the field-effect transistor studies. Further, a 1000-fold improvement in the on/off ratio and a 10-fold photocurrent enhancement over flat MoS_2 devices are also observed in optoelectronic studies. This phenomenon is attributed to the exciton funneling and the built-in potential induced by bandgap-reduction and doping-variation in wrinkled devices. This study shades a new understanding on the mechanism for hierarchical wrinkle pattern in thin-film metal, demonstrate the bio-induced production of confined, well-oriented, and electrically anisotropic graphene wrinkles and wrinkle-induced properties modification in MoS_2. The wrinkle-induced tunability of bandgap and transport in 2DNMs devices can potentially evolve technologies in flexible electronic and optoelectronic devices based on 2DNMs.

1. INTRODUCTION

2DNMs with the thickness ranging from 1 to 3 atoms include graphene, BN, MoS_2, and other transition metal dichalcogenide (TMD) monolayers have been extensively studied since graphene was first discovered in 2004.(*1, 2*) Due to a unique combination of its crystallographic, electronic and chemical structure, graphene exhibits extraordinary properties, including highest room-temperature carrier mobility,(*3*) a weak optical absorptivity,(*4*) high thermal conductivity,(*5*) and high mechanical strength.(*6, 7*) Graphene can be produced *via* graphite exfoliation (scotch-tape method),(*1*) chemical vapor deposition (CVD),(*8-10*) sublimation of SiC(*11*), and reduction of graphene oxide.(*12*) Currently, CVD is widely employed to produce graphene with a controlled number of layers, large area, and high quality. Here, metal catalysts dissociate carbon precursors into carbon atoms which bind together to form graphene. These graphene sheets are then transferred to arbitrary substrates for further study and/or applications.(*8, 10, 13, 14*) However, graphene is a zero-bandgap material, so unlike conventional semiconductors, it cannot be switched off which scuppers its direct applications in electronics. Extensive researches have been performed to introduce band gap in graphene, like wrinkling and functionalization of graphene. Three-dimensional (bulk) TMDs show various electronic, optical, mechanical, chemical and thermal properties that have been investigated for a long time.(*15, 16*) However, a resurgence of scientific and engineering interest in TMDs was because of recent advances in their atomically 2D thin film preparation, optical detection (Raman and PL), transfer of 2DNMs, and physical properties understanding of 2DNMs based on the researches on graphene in last decade.(*17*) 2D TMDs, atomic thin nanomaterials of the type MX_2, with M, a transition

metal atom, (Mo, W, etc.) and X, a chalcogen atom, (S, Se, or Te.) have been seen as promising substitutes for graphene. The strain-dependent properties of TMDs opens the possibility of various applications by strain engineering. Manipulating the properties of the TMDs by forming wrinkles is an effective route for tailoring the performance of 2D TMDs devices.

Therefore, my research is focused on a) understanding the formation mechanisms of wrinkles in thin 2DNMs, b) wrinkle-effect on properties modification in graphene, and (c) wrinkle-effect on properties modification and further application based wrinkling structure in 2D TMDs (MoS_2).

1.1 Wrinkle formation in thin films

Under compression, 2DNMs exhibit surface corrugations (wrinkles, ripples and crumples). This phenomenon separates 2DNMs from their 0D (nanoparticals) and 1D counterpart (nanowires and nanotubes) because under compression, 1D nanomaterials exhibit bending; while 0D nanomaterials remain unchanged in their structural form. The corrugations in 2DNMs can be characterized as wrinkles, ripples, and crumples based on their aspect ratio, physical dimensions, and order. Wrinkles and ripples occur on nominally two-dimensional plane, where wrinkles have a high aspect ratio with width between 1 and tens of nm, height below 15 nm, and length of 100 nm (aspect ratio > 10); and ripples are more isotropic (aspect ratio close to 1) valleys and peaks with feature size below 10 nm. On the other hand, crumples are dense deformations (folds and wrinkles) occurring isotropically (ordered or unordered) in two or three dimensions (similar to crumpled paper).

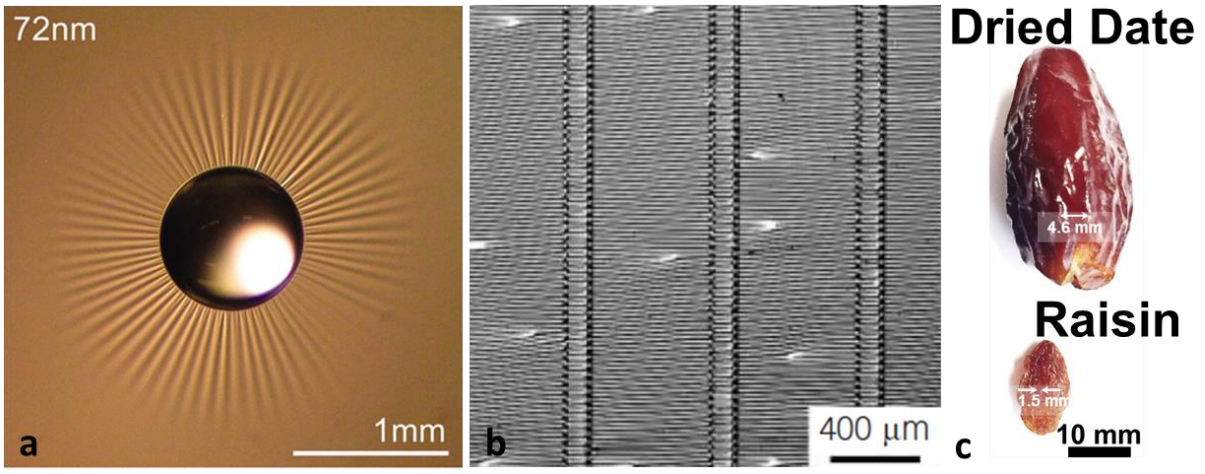

Figure 1. Wrinkles in thin films. (a) Water drop induced wrinkle in polystyrene thin film with thicknesses (72 nm) floating on the surface of water. (b) An optical image of the PDMS surface bucking after Cr/Au deposition. (c) Longitudinal wrinkles on the skin of a dried date (λ = 4.6 mm) and a raisin (dried grape) (λ = 1.5 mm). Science (2007) 5838, 650-653; Nature (1998) 6681, 146−149.

Wrinkling in soft elastic sheets is a well-established phenomenon,(*18-24*) however, wrinkles on rigid materials have received relatively less attention.(*18, 25*) As materials become thin, the bending energy, even for the rigid materials (e.g. metals), reduces significantly ($\propto$ thickness^3) making it easier to form wrinkles. For example, a thin rigid film deposited on contracting elastomeric substrates(*26-29*) (polydimethylsiloxane (PDMS)(*27*)) can readily undergo wrinkling. The transfer of the elastic energy of the substrate to the bending energy of the film creates wrinkles by reducing the projected area below the film's surface area. This process is governed by von-Kármán equations. Because of the relatively small Young's modulus of elastomers (PDMS), the bending is limited, forming large wrinkles on the rigid films (metal films: wavelength = 25 µm) (Figure 1).(*28*) Wrinkles have been observed and well-studied on thin elastomeric films floating on liquid surfaces (*18, 20*) and on films holding liquid droplets.(*19, 22, 24, 30, 31*) It has

been shown that the wrinkle patterns near the thin soft films/liquid interfaces are governed by the capillary energy (*18, 20, 31*) between liquid and films.

1.2 Mechanical properties and wrinkles in graphene

Graphene is a two-dimensional (2D) monolayer of carbon atoms with a honeycomb lattice, it has received significant interest since it was successfully exfoliated in 2004.(*1, 2*) Graphene is very thin and flexible, and ready for wrinkles and deformation as shown in Figure 2. Similar to other thin film, graphene's deformation is governed by its mechanical properties (Young's modulus, interfacial energy and number of layers). Due to the hexagonal arrangement of carbon atoms, the graphene can be terminated with a zigzag edge and an armchair edge. Further, the edge structure, and termination play important roles in the properties of graphene. Theoretically, the thickness of the graphene is ~ 0.35 nm (the thickness of one layer of carbon atom in graphite).(*32*) However, the value of thickness of graphene in the experiments is extended to much larger range (0.35 to 1.7nm).(*33, 34*) Graphene is the strongest (measured) materials with an extremely high Young's modulus (~1 TPa) and a high tensile strength (~130 Gpa).(*32*) Extensive studies have shown that the Poisson's ratio of graphene is ~0.165.(*35*) (Table I) However, recently, an investigation pointed out that the Poisson's ratio of graphene experiences a transition from positive value to negative value (independent of its size and temperature) at high strain (above 6%) and this negative Poisson's ratio results from the interplay between bond stretching and bond-angle bending in graphene lattice under strain.(*36*)

There are different mechanisms of wrinkles, ripples and crumples formation in graphene, such as (a) thermal vibration of the 2D lattice,(*37, 38*) (b) edge instability, defect and

dislocation,(*39-41*) (c) negative thermal expansion (as against positive for the substrate);(*42, 43*) (d) trapped solvent evaporation/removal,(*44*) (e) relaxation of pre-strained substrate,(*45*) (f) anchorage on substrate,(*46*) and (g) solvent surface tension.(*47*) Apart from chemical functionalization, substrate interaction, crystallography, and size, the surface corrugation on graphene can also modify its properties, e.g. electronic structure (band-gap opening (potentially > 1 eV),(*48-51*) pseudomagnetic field in bilayers,(*48*) electron/hole puddle formation,(*52*) and carrier transport).(*53*) These, in turn, can be employed to modify graphene's wettability, transmittance, chemical potential, expansion for energy storage, and conductivity. Futuristically, it is important to (a) enable control of the physical attribute of these corrugations; (b) thoroughly study the influence of wrinkles on electronic, optical, mechanical and chemical properties.(*54, 55*)

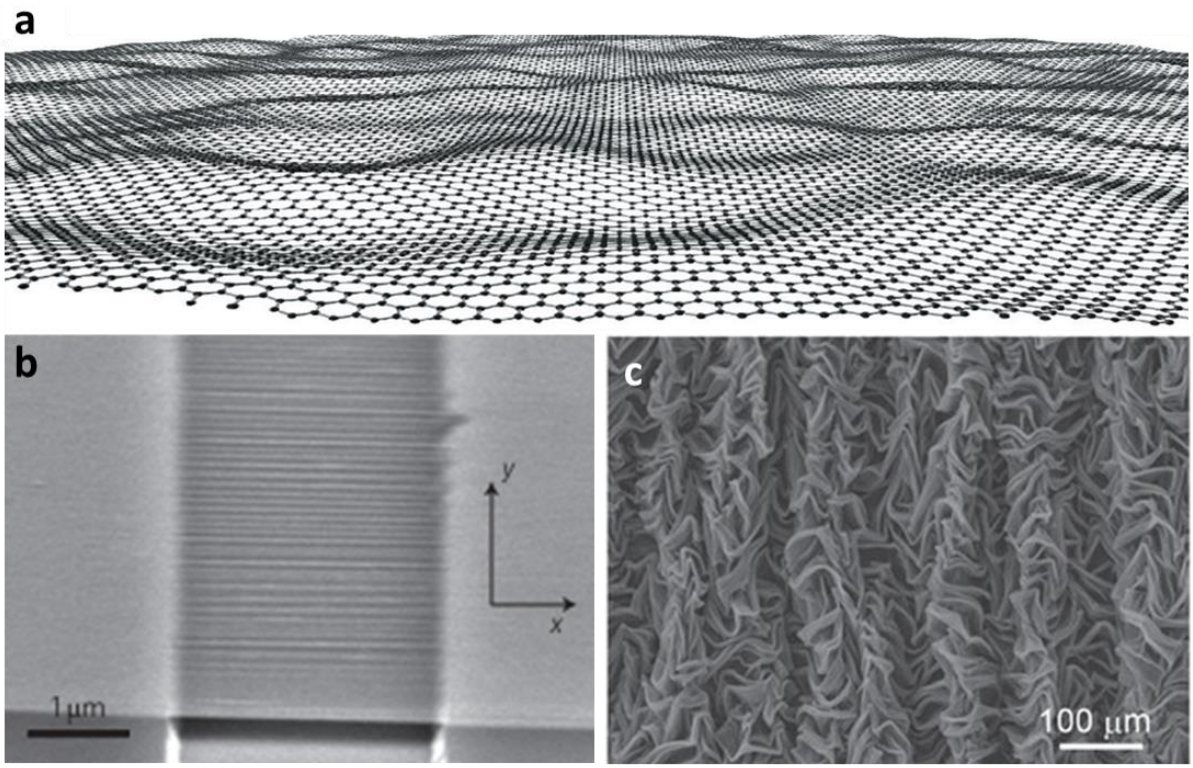

Figure 2. Rippled, wrinkled and crumpled graphene. (a) Rippled graphene; (b) wrinkled graphene and (c) crumpled graphene. Nature (2007) 446, 60–63; Nature Nanotechnology (2009) 4, 562–566; Scientific Reports (2014) 4, 6492.

1.3 TMDs and mechanical properties of TMDs

Single layer of TMDs (thickness of 6~7 Å), consist of a hexagonally sandwiched structure of metal atoms between two layers of chalcogen atoms as shown in Figure 3a.(*56, 57*) With different size of metal and chalcogen ions, the bond length of metal-metal varies between 3.15 Å and 4.03 Å. These values indicate smaller spatial overlaps of the d orbitals these TMDs thin film than that in the elemental transition metal solids. The absence of dangling bonds on the surface (chalcogen atoms) makes those TMDs relative stable against reactions. On the other hand, similar to the graphite structure, single layer TMDs are coupled by weak van der Waals forces in bulk TMDs, which leads to the crystal

to readily cleave to thin layer flakes.(*58*) Single layers of TMDs are stable, like graphene, by forming intrinsic ripple structures.(*59*) Monolayer TMDs exhibit two polymorphs: trigonal prismatic and octahedral phases. The layer-dependent properties of TMDs have attracted extensive attention.(*17*) First, the properties of buck TMDs are diverse — ranging from insulators, semiconductors, semimetals, to metals. More interesting, some bulk TMDs such as $NbSe_2$ and TaS_2 exhibit low-temperature phenomena including superconductivity and metal to non-metal transition.(*60-62*) Due to quantum confinement effect, single or few-layers not only greatly preserves their properties of bulk counterpart but also leads to additional novel properties (Figure 3b).(*63-65*) Various of TMDs have been synthesized by CVD methods, one of examples is shown in Figure 3c. Interestingly, some of them have tunable band gap structures with different layers, which offers opportunities for going beyond zero ban-gap graphene and opening novel fundamental understandings and technological applications for inorganic 2DNMs.(*58*) Wrinkles were proved to be one of promising ways to induce uniaxial strain in 2DNMs, since they can be controlled in various aspects (orientation, size, shape and number). Recent theoretical and experimental studies have shown unprecedented effects of wrinkle and strain on many physical properties of TMDs.(*66-68*) Experimentally, the in-plane Young's modulus of monolayer MoS_2 is 270 ± 100 GPa, with the average tensile strength of ~23 Gpa and ultimate strain of ~ 11%. Poisson ratio of MoS_2 is 0.27.(*59*) However, theoretically, the deformation and failure behavior are anisotropic. For example, calculations suggest that MoS_2 should undergo anisotropic nonlinear elastic deformation up to an extra-large ultimate strains with 0.24 along the armchair direction, 0.37 in zigzag direction, and 0.26

for biaxial deformation.(*69*) More anisotropic mechanical parameters of TMDs are shown in Table I. Further, MX_2 (MoS_2 and WS_2, $MoSe_2$, WSe_2, and so on) have similar lattice constants and elastic properties from theoretical simulations.(*70, 71*) In fact, strain-energy relationship of MX_2 monolayers from calculation has shown that the Young's modulus and tensile strength decrease when X varies from S to Te, and M varies from W to Mo. The calculated Poisson's ratios of TMDs monolayer ranges from 0.2 to 0.3, further, the TMDs along the zigzag direction shows higher Poisson's ratios than that along the armchair direction as shown in Table I.(*71, 72*)

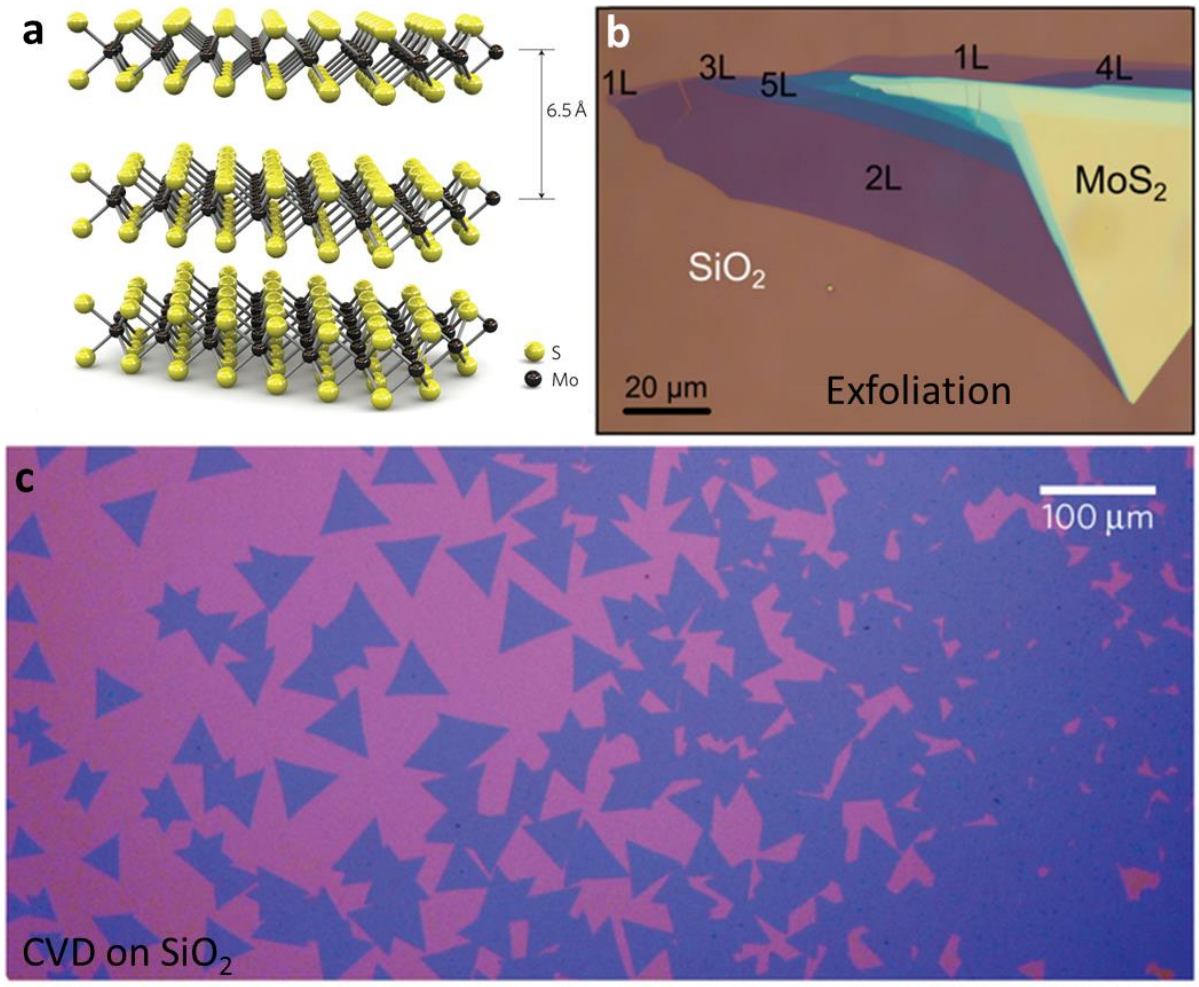

Figure 3. MoS_2 structure. (a)Three-dimensional representation of the structure of MoS_2. (b) A typical optical image of various layers of MoS_2 on SiO_2 surface. (c) A typical optical image of monolayer MoS_2 crystal on SiO_2 surface by chemical vapor method. Nature Nanotechnology (2011) 6, 147–150; 2D Materials (2015) 3, 035006; Nature Materials (2013)12, 554–561.

Table I. Summary of Structure and Mechanical Properties of the 2DNMs.

Lattice constant, Thickness, Young's Modulus, Tensile strength, Poisson ration, Ultimate strain, Zigzag direction (Z), Armchair direction (A), Experimental studies (E) and Biaxial strain (B).

2DNMs	Structure	Lattice constant (nm)	Thickness (nm)	Young's modulus (GPa)	Tensile strength (GPa)	Poisson ratio	Ultimate strain
Graphene	Planar hexagonal	0.142(*73*)	0.35(*33, 34*)	1000(*32*)	130(*32*)	0.165(*42*)	0.25(*32*)
MoS_2	Three atomic layers hexagonal	0.312(*74, 75*)	0.65(*57, 70*)	222.75 (Z)(*71*) 219.46 (A)(*71*) 270 (E)(*70, 76*)	27.35 (Z)(*71*) 16.90(A)(*71*)	0.25(*70, 72*)	0.28 (Z)(*71*) 0.19(A)(*71*) 0.11 (E)(*59*)
$MoSe_2$	Three atomic layers hexagonal	0.324(*71, 75*)	0.65(*77, 78*)	178.78 (Z)(*71*) 175.97 (A)(*71*) 177(E)(*77*)	22.68 (Z)(*71*) 12.86 (A)(*71*) 4.8 (E)(*77*)	0.23(*72*)	0.29 (Z)(*71*) 0.16 (A)(*71*) --- (E)
WS_2	Three atomic layers hexagonal	0.314(*71, 75*)	0.65(*70*)	244.18 (Z)(*71*) 240.99 (A)(*71*) 272(E)(*70*)	29.96 (Z)(*71*) 19.91 (A)(*71*)	0.22(*70, 72*)	0.28 (Z)(*71*) 0.18 (A)(*71*) --- (E)
WSe_2	Three atomic layers hexagonal	0.326(*71, 75*)	0.7(*79-81*)	196.81 (Z)(*71*) 194.13 (A)(*71*) 167(E)(*79*)	24.70 (Z)(*71*) 15.05 (A)(*71*)	0.19(*72, 79*)	0.30 (Z)(*71*) 0.17 (A)(*71*) --- (E)

2. LITERATURE REVIEW

2.1 Wrinkle formation in thin films and interfacial properties

2.1.1 Wrinkle formation in thin films

Formation of wrinkles in thin films adhered to flexible or shrinkable substrates is a common phenomenon. Wrinkles are ubiquitous and can be found almost everywhere, such as the skin of fruits,(*82*) human or animal skins or dried dates,(*29, 35*) polymers thin film floating on water,(*18*) and even in the hanging curtains on windows.(*83*) While different wrinkle wavelengths in this different films and on different substrates are due to the scaling of the wrinkles with thickness as per *Föppl-von Kármán* relationships, for example:(*28*)

$$\lambda = 2\pi t(\frac{\bar{E}_{2DN}}{3\bar{E}_S})^{1/3} \quad (1)$$

where, t is the thickness of the 2DN, $\bar{E}_{2DN}$ is the plane-strain modulus of the 2DN film and $\bar{E}_S$ is the in-plane strain modulus of the substrate. $\bar{E} = E/(1-v^2)$, with E is the Young's modulus and v is the Poisson's ratio. This equation assumes strong adhesion between 2DNMs and the substrate with no slip between the two layers. For example, graphene is the thinnest material, its wrinkle-wavelength is expected to be small. Further, wavelength of wrinkles formed in thin films depends on the strain modulus of the thin films and their substrates,(*84*) with softer films or stiffer surfaces (high strain modulus) producing wrinkles with small wavelength.

Thin metal films are stiff (high Young's modulus), which is well studied in recent years. Most of attention were focus on spontaneously form wrinkled thin metal films on polymer

solid substrates and liquid surfaces. One example is formation of controllable wrinkles

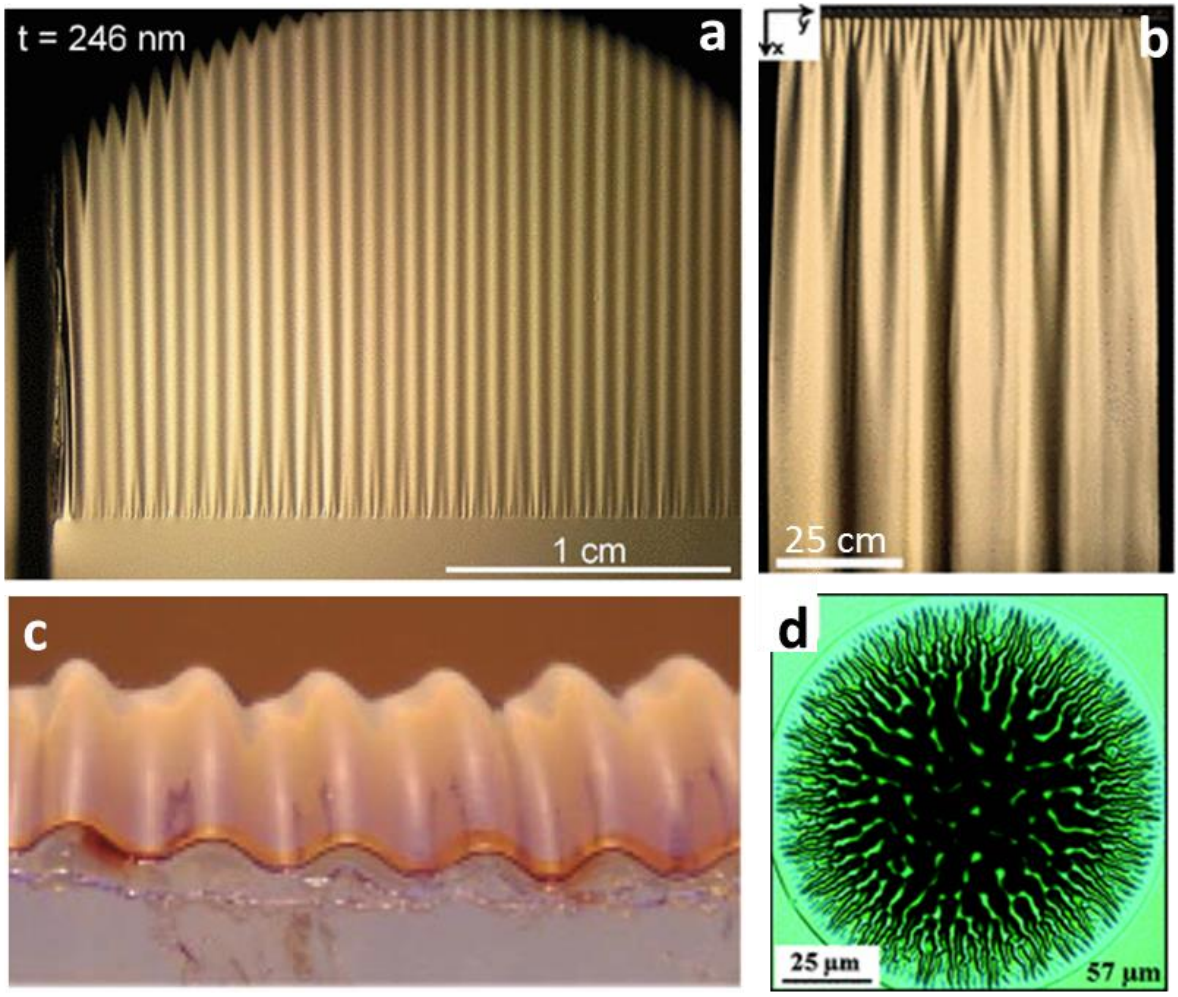

Figure 4. Wrinkles in different thin film and on various substrates. (a) An optical image of a compressed polystyrene sheet floating on the surface of water. (b) wrinkles with a wrinklon pattern on rubber curtain. (c) Wrinkled polyester film on gel. (d) Wrinkled chromium thin film on silicone oil. Physical Review Letters (2010) 038302; Physical Review Letters (2011) 224601; Science (2008) 5878, 912-916; Physical Review E (2013) 042401.

patterns in thin films of metals electrically deposited (electron beam evaporation) on an elastomeric polymer (PDMS).(*26*) Nanometer thickness of gold thin film (on a 5-nm titanium or chromium as adhesion interlayer)—were deposited on PDMS. The metal source heats and expands the PDMS substrate during deposition process. After cooling

to ambient temperature, because of different thermal expansion confidents, the shrinkage of polymer substrate induces formation of wrinkles in thin metal films on the substrate surface. Further, by varying the properties and patterning of the PDMS surfaces, eminently controllable (orientation and periodicity) wrinkles can be produced. Further, Yu et al. reported that hierarchical wrinkles formed in thin chrome film by sputtering chrome on silicone oil surface, with wrinkles formed aligned in the perpendicular direction of the silicone oil edge (Figure 4d).(*85*) Capillary force can induce wrinkles formation near a water drop placed on a thin floating film(*19*) and at the edge of the thin film floating polymer film.(*18*) Various models were established to understanding the formation mechanism of wrinkles and patterns, such as the wrinklon model and capillary force model.(*18, 19, 26, 28, 83*)

2.1.2 Interfacial adhesion energy

Most of wrinkled structures and deformations in thin films are due to the interfacial interaction between these thin films and substrate surfaces. The interactions between thin films and substrates affect the electrical, chemical and mechanical properties of thin film materials and their applications.(*86, 87*) Therefore, thin film interaction and adhesion are indispensable properties not only for understanding of wrinkles formation in 2DNMs on substrates, but also for emerging technology such as heterostructures of two-dimensional nanomaterials devices.(*88*) The adhesion energies of thin films on dissimilar rigid substrates have been measured qualitatively (tape tests),(*89*) which was used to compare the adhesion of different films; and quantitatively with numerous methods,(*90*) like, scratch testing,(*91, 92*) four point bend testing,(*93*) stressed overlayers,(*94*) and

nanoindentation.(*95*) Nevertheless, it has been a great challenge to measure the adhesion of the 2DNMs on substrates, since the thin 2DNMs is hard to handle and prone to damage in the conventional tests. Recently, new methods for the adhesion measurement of graphene on various substrates have been reported as shown in Figure 5, such as pressurized blisters,(*96*) nanoparticle blisters(*97*) and mechanical delamination.(*98*) The pressurized blisters method was introduced by Bunch's group (Figure 5a).(*96, 99*) Mechanically exfoliated or chemical vapor deposited 2D nanomaterials suspended over pre-defined microcavities in oxidized silicon wafers.(*66, 96*) Because of the excellent gas molecular impermeability of 2D nanomaterials, sealed micro cavities were formed. Samples were left in the pressure chamber at pressure P_0 for couples of days to make sure P_{int} (pressure in the blisters) to equilibrate to P_0 through the slow diffusion of gas through the SiO_2 substrate. The pressure difference ΔP between the environment P_{ext} (out of sealed micro cavities) and microcavities P_{int} deformed the 2DNMs and induced strong tensile strain in these thin films when the samples were place in a different pressure chamber (P_{ext}). The measurement of adhesion energy between 2DNMs and substrates can be achieved by analyzing the blister shapes and film delamination. Nanoparticles were utilized to form blisters in graphene by covering graphene on these nanoparticles on silicon oxide surface, as shown in Figure 5b.(*97*) Wrinkles and delamination of thin film on pre-stretched substrate were also applied to study the adhesion energy, however, this method is limited by the convolution of the AFM tip and relatively sharp ridges of buckling (Figure 5c and 5d).

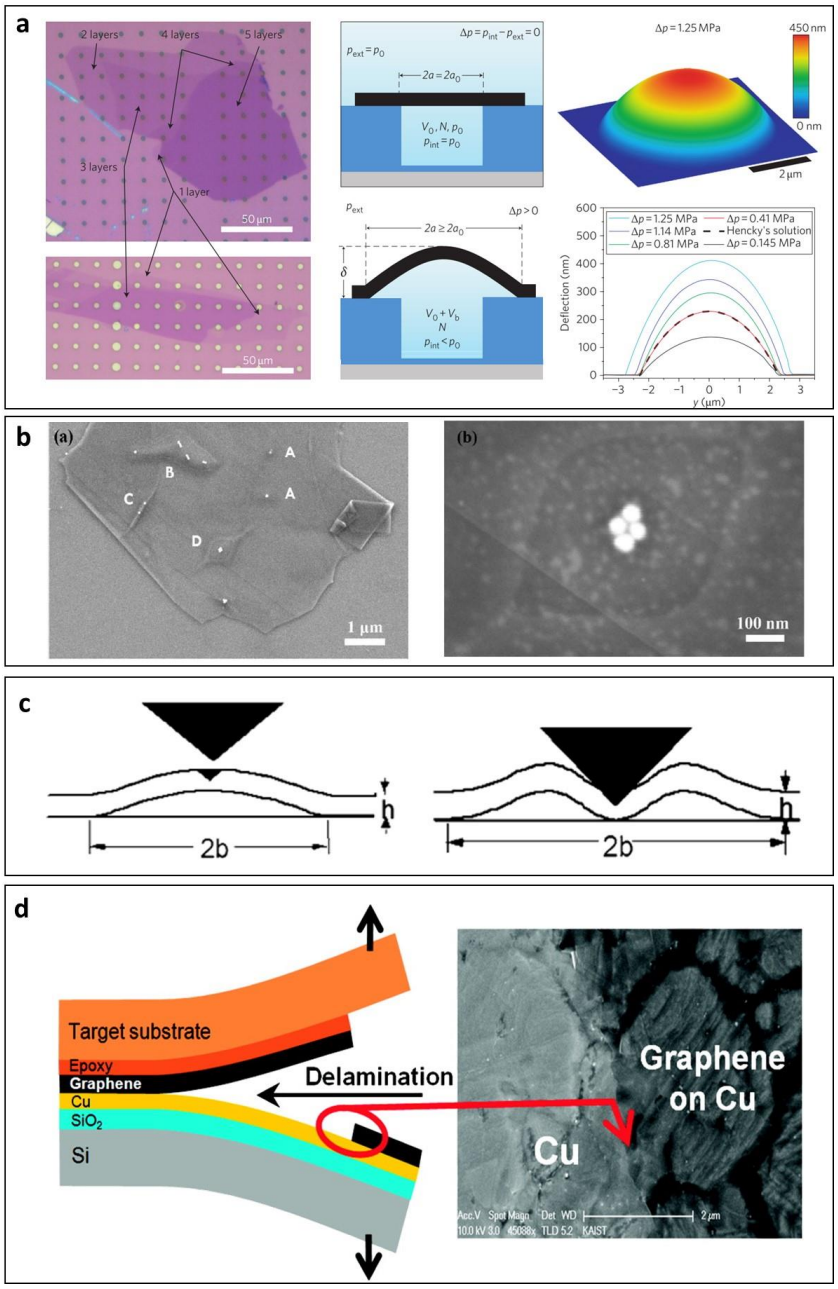

Figure 5. Adhesion energy measurement experiments. (a) Typical optical images showing different layer of graphene flakes suspended on SiO_2. Schematic of a graphene blister before and after placing in the pressure chamber. Three-dimensional rendering of an AFM image of a typical pressure blister. Deflection versus position for five different values of Δp. (b) Typical SEM images of graphene blister of gold nanoparticle on silica surface. (c) Schematic of indentation-induced blisters method. (d) Schematic Illustration of graphene transfer to a target substrate using the mechanical delamination process and SEM of a sample with graphene on copper. Nature Nanotechnology (2011) 6, 543–546. Journal of Applied Physics (2009) 2, 026104; IEEE Transactions On Device And Materials Reliability (2004) 2, 163−168; Nano Letters (2012) 3,1448-1452.

The relative weak Van der Waals force is the most common interaction that contributes to the adhesion energy between 2DNMs and thin film materials with other substrates. Therefore, adhesion energy higher than 1 J/m^2 cannot only be due to van der Waals interactions. High adhesion energies of 2DNMs on various substrates in experiments may due to several extra effects, like roughness of the substrate surface, defects, and wettability. For example, high adhesion energy of graphene was suggested due to a toughening mechanism (asperity locking of rough surfaces).(*100, 101*) Kumar et al. shown that the reactive defects on the substrate surface can induce discrete, short-range interactions and further a high shear strength as well as high sliding resistance.(*102*) Further, a layer of water at the interface has the potential to induce a long range but weak (graphene is hydrophobic) interaction through capillary bridging.(*103*)

Additionally, wrinkles in MoS_2 on soft materials have been shown in previous studies.(*67, 104, 105*) Since soft materials are stretchable, wrinkles can be formed on soft substrates by transferring MoS_2 to a pre-stretched surface and releasing the stretch after thin film deposition. It is hard to form wrinkles on unstretchable rigid substrates. However, direct measurement of the adhesion energy of MoS_2 solid on substrates (SiO_2, Si_3N_4, *etc*.) is important to better understand wrinkles formation mechanism and control the mechanical release of the wrinkles in the MoS_2 for electrical device application.

2.2 Graphene wrinkles formation mechanism and properties

Graphene, is flexible(*38*) (quasi-fluidic) and can form wrinkles,(*42*) crumples,(*45*) and folds.(*53*) In contrast, under compressive-deformation, 0D nanomaterials remain morphologically unchanged and 1D nanomaterials bend. Graphene can exhibit

wrinkles(*67, 106*) due to thermal vibrations (internal ripples),(*37, 38*) differential compressive forces,(*107*) edge instabilities,(*39*) thermodynamically-unstable (interatomic) interactions,(*108, 109*) strain in 2D crystals,(*40, 110*) thermal contraction (graphene),(*42*) solvent channel formation,(*44*) pre-strained substrate-relaxation,(*45*) multi-point surface-anchorage,(*46*) and/or high solvent surface tension during transfer.(*47*) Further, the creation of a local strain distribution and the rehybridization of π-clouds due to such structural changes influence (a) the electronic structure,(*48, 111*) local charge density,(*112*) dipole moment,(*113*) and optical properties(*45*) of graphene; and (b) its local chemical potential due to the formation of electron-hole puddles.(*114*) Thus, wrinkles on graphene with defined attributes and regulated mechanical and surface properties (*42, 45, 46, 53*) can be applied towards a wide range of applications including 2D opto/electronics and lithography. The wrinkle-formation mechanism in graphene and properties modification of wrinkle structures in graphene is shown here.

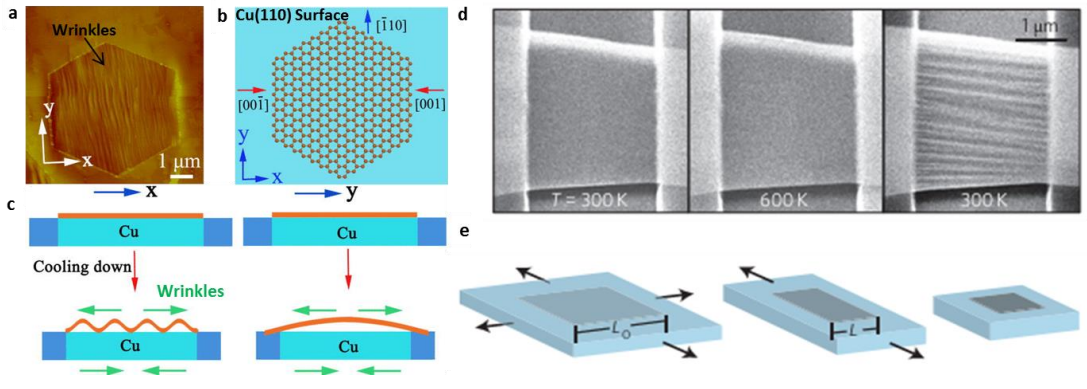

Figure 6. Examples of graphene wrinkles formation. (a)- (c) wrinkles formation cause by thermal expansion mismatch in CVD process. (d) Thermal manipulation method for wrinkles formation. (e) Pre-stretched method. Applied Physics Letter (2013), 103; Nature Nanotechnology (2009) 4, 562–566; Nature Materials (2013) 12, 321–325.

2.2.1 Formation mechanism and methods for wrinkled graphene

2.2.1.1 Intrinsic thermal fluctuations, edge stress and defects/dislocations

Strictly, 2D crystals are expected to be unstable due to the thermodynamic requirement for the existence of out-of-plane bending with interatomic interaction generating a mathematical paradox.(*108, 109*) The stability of the pseudo 2D material is achieved by ripple formation resulting from the partially decoupled bending and stretching modes.(*37, 115*) The fact that free-suspended graphene is not strict 2D was revealed by transmission electron microscopy (TEM) experiments, where suspended graphene membranes exhibited pronounced out-of-plane deformations (ripples) with height up to 1 nm.(*38*) Mechanistically, the temporal and spatial modulation of the C-C bond-lengths due to thermal-vibrations and interatomic interactions induce carbon to occupy space in the third dimension,(*37, 115-117*) thus forming dynamic ripples and minimizing the total free energy, as observed in free-standing graphene.(*107*) Further, the delocalized electrons in the π-cloud (and associated electron-hole puddles formed) lead to asymmetric distribution of bond lengths. This asymmetry forces the lattice to become non-planar to minimize free energy. Additionally, the asymmetry of bond-lengths in graphene is amplified on the edges and near defects, thus increasing the wrinkle density in these regions.(*37, 39*) Chemical vapor deposition based production of graphene sheets at large scale commonly leads to polycrystallinity and defects. Out-of-plane deformation (wrinkles and ripples) can significantly reduce the magnitude of in-plane stresses generated by the defects.(*118*) Therefore, atomic line defects like grain boundaries (or dislocations) can induce wrinkles and ripples on graphene.

2.2.1.2 Growth of graphene on metal via CVD process and epitaxial on SiC

The interaction between the substrate and graphene strongly influences wrinkle- and ripple- formation. Graphene grown on metallic catalysts exhibits high densities of wrinkles due to the opposite polarity of thermal expansion coefficients (TEC) of graphene and the metals.(*119*) This is because the TEC of graphene is negative, attributed to the displacement out of the graphene plane resulting from the flexural phonon and limited contribution from the in-plane vibrations.(*47, 53*) In an experiment where a crystalline island of graphene was grown on copper, isotropic and self-similar wrinkles were achieved as showing in Figure 6a, 6b and 6c.(*43, 50, 120*) Besides the opposite thermal deformation, the defect lines on metal substrates also play an important role in the formation of wrinkles on graphene.(*121*) Liu et al. showed that the wrinkle attributes and density are governed by the growth substrates (nickel in this case), its thickness and the process employed to transfer graphene. With the increase of nickel thickness, graphene's grain-size reduces, resulting in higher-density (and smaller) of wrinkles on graphene.(*47*) Graphene grown epitaxially on SiC (a semiconductor substrate)(*11*) also produces wrinkles due to thermal expansion of graphene during the cooling step in this process.(*122, 123*)

2.2.1.3 Graphene transfer process

Graphene grown on metals are routinely transferred to other substrate and tend to form wrinkles. Calado et al. showed that water drainage from between graphene and substrate plays an important role in wrinkle formation. Here, the wrinkles form on and along the water drain channels.(*96*) Moreover, the morphology of underlying substrates can control the orientation of the wrinkles.(*124*) For rough surfaces, the additional stress due to

adhesion may increase the number of wrinkles. For example, Lanza et al. showed that the strain-induced wrinkles on graphene can be significantly reduced by improving the adhesion between graphene and rough substrates.(*125*) The stresses due to interaction with and/or anchorage on surfaces cause the formation of wrinkles. (*26, 46*)

2.2.1.4 Controlled wrinkles formation in graphene

Due to the intimate interplay between wrinkle attributes and graphene properties, controllable fabrication of wrinkles on graphene is important. Bao et al.(*42*) reported that controlled and organized microscale wrinkles can be produced by thermal manipulation leveraging the negative thermal expansion coefficient of graphene (Figure 6 d). In their work, graphene and ultrathin graphite membranes were transferred and suspended across predefined trenches on SiO_2 /Si substrates (Figure 6d). By annealing suspended graphene, wrinkles were formed perpendicularly to the trench direction. Importantly, the orientation, wavelength, and amplitude of wrinkles are influenced by the structure, shape, and temperature of the substrate.(*42*) Zang et al. reported that the crumpling and uncrumpling of large-area graphene can be controllably achieved(*45*) by applying a pre-stretched elastomer film substrate *via* regulating relaxation and pre-strain order. Graphene (3-10 layers) grown on nickel substrates were transferred to polydimethylsiloxane (PDMS) stamps. An elastomer film was biaxially stretched with pre-strain = 200-400% to use as a pre-stretched substrate. The graphene on PDMS was stamp-transferred to this elastomer film. Relaxing one pre-stretched direction produced unidirectional wrinkles (Figure 6e), which were well developed. This was followed by biaxial relaxation of the film to produce wrinkles from two dimensions to form crumpled

graphene. Further, this crumpled graphene would unfold as the substrate film is biaxially re-stretched. The unidirectional wrinkle wavelength achieved in this work was 0.6-2.1 μm.

Table II. Summary of the correlation between corrugation attributes and graphene properties and applications.

Wavelength/Width (nm)	**Height, Aspect Ratio or other Relationship**	**Modified Properties and/or Applications**
0.1 – 10 nm	Intrinsic ripples aspect ratio of ~ 1 with height (H) ~ 0.2 nm(*38*) Thermal contraction on Cu trench: H ~ 0.05 nm and W ~ 0.7 nm(*52*) Thermal contraction on Rh foil: H ~ 7.9 nm and W ~ 8.2 nm(*48*) Transfer of SiO_2 post CVD: H ~ 3.3 nm and W ~ 6.8 nm (*124*)	Pseudomagnetic behavior(*48, 126*) Band-gap opening(*48, 50, 127*) Carrier scattering(*128*) Electron–hole puddles formation(*52*)
10 – 100 nm	Simulation Studies(*53*)	Carrier scattering Anisotropic electron transport(*53, 129*)
100 nm – 1 μm	Thermal contraction on Cu foil: H ~ 25 nm and W ~ 300 nm(*43*)	Mobility limitation Conductivity reduction Band gap opening(*49*)

	Reduced graphene oxides crumpled graphene(*130*) Pre-stretched H ~ 70 nm and W ~ 500 nm(*131*)	Charge storage enhancement(*130*) Strain sensitivity (*131*)
Above 1 μm	Pre-stretched crumpled graphene (*45*) Thermal contraction on Si trench H ~ 30 nm and W ~ 2 μm(*42*)	Tunable transparency, wettability, and thickness at different voltages(*45*) Chemical reactivity enhancement(*132*) Charge storage enhancement(*133*)
Relationships	Ratio between height and radius (R), H/R > 0.07(*134*) H > $\pi\sqrt{C/\gamma}$ (C = bending stiffness and γ = surface energy)(*135*)	Chemical activity enhancement (*134*) Self-folding (*135*)

2.2.2 Properties and applications of wrinkled graphene

Wrinkles influence several electronic phenomena, including suppression of weak localization,(*112*) electron–hole puddles,(*107, 136, 137*) band-gap opening,(*48-50, 127*) pseudomagnetic field in bilayers,(*48, 126*) and carrier scattering.(*53, 128*) They exhibit other atypical properties, such as surface and optical modification,(*45*) energy storage,(*45, 131*) chemical activities enhancement,(*138, 139*) and biointerfacing.(*46*)

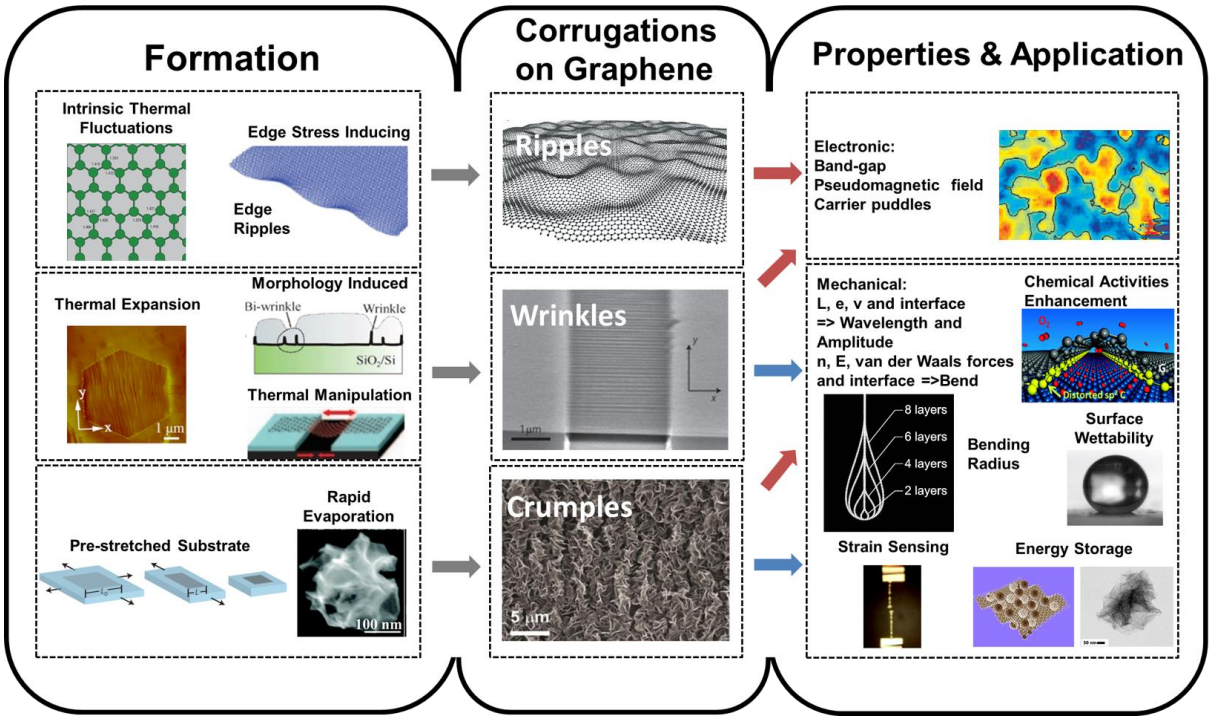

Figure 7. A summary illustration of corrugations on graphene formation, properties and application.

Nature Materials (2007) 6, 858-861; Physical Review Letters (2008) 101, 245501; Applied Physics Letters (2013), 103; Nano Research (2011) 4, 996-1004; Nature Nanotechnology (2009) 4, 562-566; Nature Materials (2013) 12, 321-325; Nature (2007) 446, 60-63; Nature Physics (2008) 4, 144-148; Applied Physics Letters (2009) 95; ACS Nano (2011) 5, 3645-3650; The Journal Physical Chemistry C (2009) 32, 14176; ACS Applied Materials and Interfaces (2014) 6, 7434-7443; ACS Nano (2011) 11, 8943; Carbon (2015) 93, 869.

2.2.2.1 Electronic properties

The curved geometry and strain in graphenic systems are known to couple with the 2D massless Dirac Fermions *via* gauge field and scattering potential to alter the electronic structure.(*49*) For planar graphene model (only an idealistic model), the Fermi level lies at the Dirac point, where the density of electronic states vanishes.(*140*) Both disorder and impurities in graphene introduce a violation of the electronic homogeneity of graphene. Amongst other causes, the corrugations on graphene suppress electron-transport,(*141,*

142) mobility, weak localization (by fluctuating position of the Dirac point(*112*)) and quantum corrections.(*143-145*) The quantum correction is a result of quantum interference of electrons moving in different trajectories.(*146*) It includes interference of time-reversed trajectories (weak localization correction) and elastic scattering induced interference of electrons on Friedel oscillations of the electron density (Altshuler–Aronov correction).(*143, 146-148*) The electron and hole puddles created due to the disorder in graphene was imaged by Suyong et.al. *via* scanning tunneling microscopy (STM) and scanning tunneling spectroscopy (STS).(*112*) The topography of monolayer graphene on a SiO_2/Si substrate exhibits a height variation of about 1.2 nm. In an ideal graphene layer, the carrier density can be continuously tuned from hole to electron doping from zero density at Dirac point (E_D).(*149-151*) The local graphene geometry and its carrier distribution were strongly correlated.(*137*)

As mentioned above, wrinkling (rippling or crumpling) can tailor the electronic structure of graphene.(*111*) Two effects are outlined: (a) π-σ rehybridization between nearest neighbors resulted an effective electrochemical-potential variation; and (b) nearest-neighbor hopping integral variation induced an effective "vector potential". The estimated electrochemical potential variation associated with the ripples (observed experimentally) is on the order of ±30 meV. The bond stretching and the dipole moment created by polarized π-cloud density in wrinkled graphene can open a relatively large band-gap and modify the local chemical potential enabling selective functionalization.(*53*) A band gap of 0.14–0.19 eV by both the periodic wrinkles and the surface chemistry was shown by modeling grid-like periodically modulated graphene.(*127*)

Yan et al. found the lattice strain and large curvature of a wrinkle in twisted bilayer graphene can result in pseudomagnetic field (~ 100 T) interacting directly with electronic states of the sheet. On strained and wrinkled monolayer graphene, this could open up a band-gap and generate hyperbolic energy dispersion. Costa. et al also reported that periodic wrinkles/folds in graphene will possess enhanced spin-orbit interaction *via* curvature, which can open gap and allow spin-polarized transport at low magnetic fields.(*152*) It is important to note that inter-wrinkle spacing greater than the mean free wavelength of carriers minimizes the influence of wrinkles/corrugations on barriers.(*124*)

Further, a distinct anisotropy in the fold resistivity on the graphene was observed and attributed to transport along and across the folded wrinkles *via* diffusive transport of charge distributed across multilayered folds (increased ON/OFF ratio) and local interlayer tunneling across the collapsed region (adds the resistance of the order of graphene contact resistance).(*53*) The quasi-periodic nanoripple arrays of graphene causes anisotropy in charge transport and affects the limitation on both the sheet resistance and the charge mobility.(*153*) Analogous results of anisotropic Landau levels quantization and thermal conductivity of wrinkling graphene were also demonstrated.(*129, 154*)

2.2.2.2 Surface properties and strain sensing

Remarkably, wrinkles on single-atom-thick graphene can also modulate its surface properties and transparency. Zang et al. found that crumpled graphene exhibits tunable wettability and high transparency (Figure 9(a,b)). The contact angle measurement for water on crumpled graphene obeyed Wenzel and Cassie-Baxter laws for conforming and non-conforming interactions (with air gaps), respectively. Further, the voltage applied

across an elastomer sandwiched between crumpled graphene leads to Maxwell stress, which reduces the thickness and increases the area of the elastomer layer. It further tuned the transmittance in the visible range with voltage, as displayed in Figure 9 (c, d).(*45*) Similarly, Wang et al. and Zang et al. demonstrated that graphene wrinkles created by releasing a pre-strained substrate can be used as a strain sensor, where the device resistance changes with strain (Figure 9f).(*45, 131*)

2.2.2.3 Energy storage

Recently, there has been a great thrust in applying graphene as electrodes for supercapacitors due to its high surface area and conductance. Wrinkled and crumpled graphene are advantageous for these applications since they make the sheets less stiff while inhibiting stacking and retaining increased surface area. Further, graphene nanosheets with a preponderance of exposed edge planes and wrinkles enhance charge storage. Supercapacitors based on graphenic electrodes have the potential to be smaller than the low-voltage aluminum electrolyte supercapacitors in electronic devices.(*130, 155, 156*) Further, the graphenic wrinkles provide fast Li^+ diffusion channels with a low activation barrier of about 0.1 eV, which is lower than that of a graphene without wrinkles (0.3 eV) for lithium ion battery application.(*157*) The wrinkles also provide the extra expansion allowance during lithiation, which addresses a major current challenge of anode cracking due to volume expansion.(*138, 158*)

2.2.2.4 Chemical activities and functionalization affinity modification

Partovi-Azar et al. found that the topology of graphene governs the formation of electron–hole puddles (*107, 137*) on graphene. Further Wang et al.(*114*) has shown the

relationship between electron-hole puddling and functionalization affinity of graphene. Clearly, wrinkles (and other topologies) in turn influence the chemical activity of graphene, as studied by Boukhvalov and Katsnelson.(*134*) Wrinkled graphene has also been applied as a scaffold to attach nanoparticles for energy applications.(*138, 158*) Further, wrinkles on graphene have been leveraged as nucleation sites for H_2 generation at the cathode in brine electrolysis experiments(*159*) (to delaminate graphene from metals). The wrinkles, ripples or crumples on graphene can also be applied to the fabrication of other graphene structures. By designing the surface morphology of growth substrate (with microscopically parallel slip lines) and subscribing to a suitable transfer technique, wrinkled graphene was synthesized on SiO_2/Si substrate. Large-area, oriented graphene nanoribbons (GNRs) arrays with a width less than 10 nm were then produced by plasma etching as confirmed by atomic force microscope (AFM) and field-effect transistor studies. (*160*)

2.3 TMDs fabrication and properties

Graphene's success has shown the possibility to create stable, single and few-atom-thick layer nanosheets from exfoliation of van der Waals bulk materials, like TMDs. These TMD materials exhibit fascinating physical properties and promising applications beyond the properties of their bulk counterparts.

2.3.1 Fabrication of TMDs

Extensive studies on bulk and exfoliated TMDs have been conducted for decades, a surging attempt on synthesis and isolation of single-layer or few-layer nanofilm exploded after the success of graphene.

2.3.1.1 Mechanical and chemical exfoliation

Similar to graphene studies, scotch-tape mechanical exfoliation method yields small quantities of the highest-quality thin layer samples, which are ideal for the demonstration of high-performance devices and fundamental phenomena study.(*58, 161-167*) On the other hand, liquid exfoliation methods are likely to be better suited for large quantities and lower quality requirement and applications, like electrochemical energy storage, catalysis, sensing or fillers for composites. It was employed to fabricate monolayer and thin layers nanosheets of various layered TMDs, such as MoS_2, WS_2, $MoSe_2$, $NbSe_2$, $TaSe_2$, $NiTe_2$, $MoTe_2$.(*168*) Thin films of TMDs were dispersed in an aqueous solution of the surfactant sodium cholate followed by sonication, and these surfactants coat the sheets, preventing their re-aggregation. Ultrasound-promoted hydration of lithium-intercalated compounds has been one of the highest efficient liquid exfoliation methods for large quantity production of TMDs nanosheets. In this method, lithium was operated to intercalate into layers of MoS_2 by both chemical and electrochemical methods.(*167, 169*) The formation of Li_xMoS_2 in the lithium intercalation process is critical for tuning the yield of the monolayer of MoS_2. Zeng et al. showed electrochemical lithiation process in a battery test system, as shown in Figure 8a. In this method, the bulk material was incorporated by binders in a test cell as a cathode. The lithium foil was used as an anode to provide lithium ions. A cut-off voltage was determined to obtain the optimized Li amount inserted in the bulk material in order to get the sufficient insertion of lithium and effective exfoliation. The lithium intercalation process was performed at a galvanostatic discharge with a current. After washing in acetone to remove the residual electrolyte, the lithium intercalated compound was ultrasonicated in water or ethanol to get exfoliated and isolated two-

dimentional nanosheets.(*167*) However, the obstruct of application of these liquid exfoliation methods is still the low yield of the single layers (instead of few layers) and the small lateral dimensions of the exfoliated sheets (size).(*58*)

2.3.1.2 Chemical vapor deposition of thin layers TMDs

CVD is also one of the most promising methods for large-scale synthesis of TMDs thin films. Same or similar strategies and methods on the fabrication of MoS_2 can be extended to other single-layered TMDs materials' fabrication. Therefore, the details of MoS_2 growth by CVD methods are highlighted here. There are several different CVD methods for synthesis of large-area ultrathin MoS_2 layers,(*17*) which can be outlined as three categories: (1) vaporization of Mo and sulfur precursors and their decomposition, (2) sulfurization of Mo film, and (3) sulfurization of MoO_3 to MoS_2.(*58*)

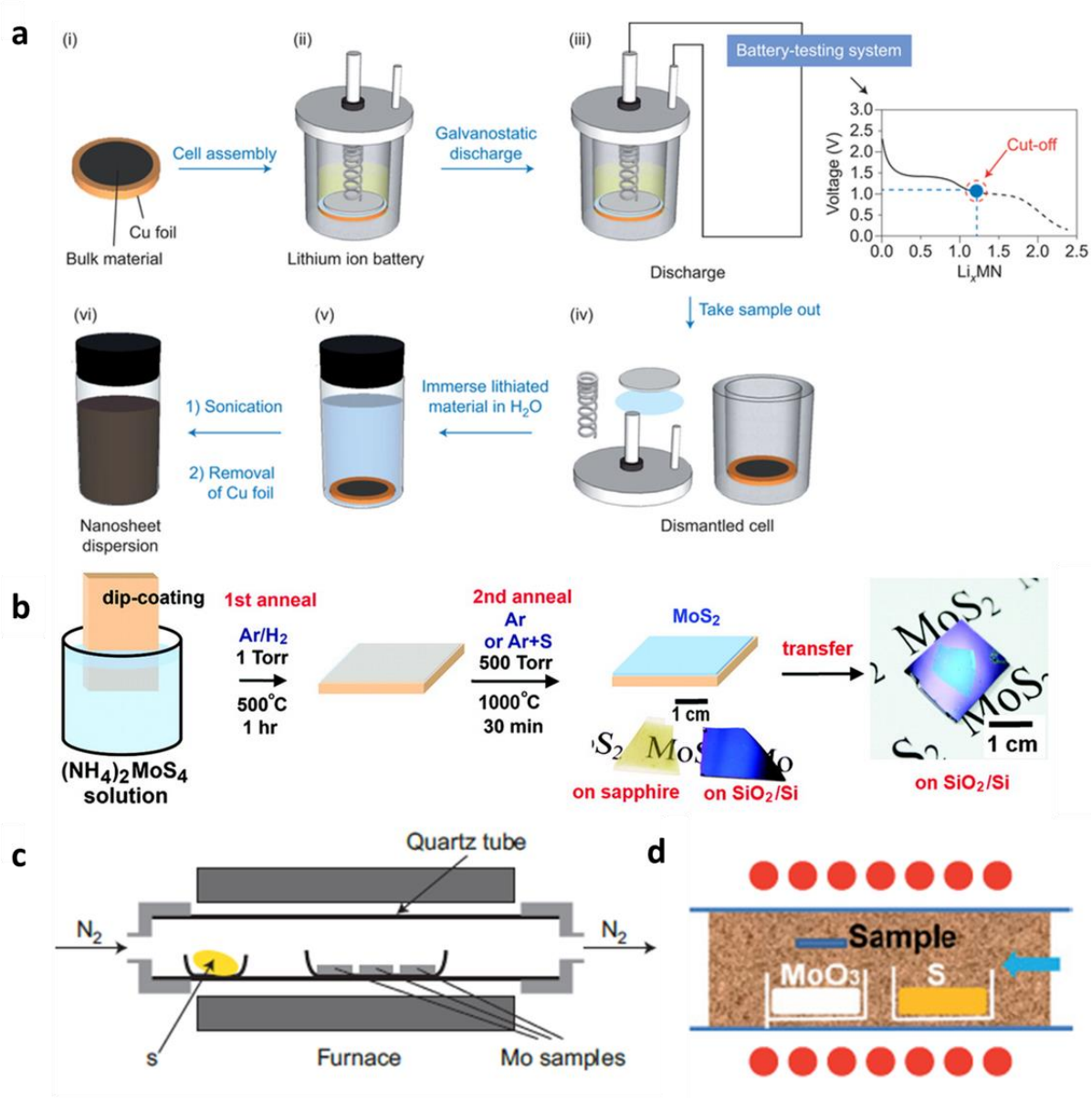

Figure 8. Schematic illustrations of TDMCs fabrication methods. (a) Schematic illustration of the electrochemical lithiation process. (b) Schematic illustration of the synthesis of MoS2 thin layers with (NH4)2MoS4 as precursor. (c) Schematic illustration of sulfurization of Mo thin film into thin layered MoS_2. (d) Growth of a MoS_2 monolayer by sulfurization of MoO_3. The red circles represent the heating reaction chamber. Nature Chemistry (2013)5, 263–275; Nano Letters (2012) 3, 538–1544.

For the two-step vaporization of Mo and sulfur precursors method:(*170*) (a) dip-coating in

ammonium thiomolybdate [$(NH_4)_2MoS_4$] in dimethylformamide (DMF) solution, and (b) crystallization of [$(NH_4)_2MoS_4$ to MoS_2 by annealing at 500 °C and sulfurization at 1,000 °C in argon gas at 500 Torr as shown in Figure 8b. Single-layer and few layers MoS_2 can be produced by sulfurization of Mo metal thin films.(*171*) First, a layer of thin Mo film (thickness <5 nm) was deposited on SiO_2 by an e-beam evaporation. Sulfur was induced from low temperature (a little above 113 °C) zone by a carrier gas (N_2) and reacted with Mo at 750 °C for 10 min. The thickness of the formed MoS_2 depends to the thickness of the pre-deposited Mo metal and therefore thickness of MoS_2 can be controlled (Figure 8c). The most popular method for synthesizing wafer-area MoS_2 monolayer flakes is the gas-phase reaction of MoO_3 with S vapor at 1000 °C, which was firstly demonstrated by Lee et al (Figure 8c).(*172, 173*) However, despite initial reports showing huge potentials, large-area, large-grain and uniform growth of monolayer TMDs using CVD remains a challenge.

2.3.2 Properties of TMDs

Thin layer TMDs materials exhibit fascinating and technologically promising properties beyond the properties of their bulk counterparts and graphene.

2.3.2.1 Electronic structure and electrical transport properties

TMDs can be semiconducting or metallic, which depends on the metal atoms. In general, MoX_2 and WX_2 compounds are semiconducting whereas NbX_2, ReX_2 and TaX_2 are metallic. When MX_2 is exfoliated, or synthesized into thin sheets, edge termination by either M or X atom is possible depending on the chemical potential of the formation environment. Due to the quantum confinement induced by the absence of d (Mo atoms)–

p_z (S atoms) orbitals interaction from MX_2 layers, band gaps widen along with the decrease of layers of TMDs. Furtherly, in some cases, there is a bandgap transition in different thickness of TMDs, for example, an indirect bandgap (1.3 eV) in the bulk MoS_2 changes to a direct bandgap (1.8 eV) in the single layer MoS_2.(*61*) This shift was also proved in first principles calculation, the indirect bandgap transition in the bulk material shifts to direct bandgap in the monolayer at the Γ-point. The direct bandgap transitions at the K-point (energy states of conduction band at K- points are mainly formed by localization of d orbitals on the Mo atoms) remain relatively unchanged with layer number (Figure 9a).(*17, 163*)

High charge carrier mobility, high on/off ratio, high conductivity and low off-state conductance are desirable for digital logic transistors.(*17*) MoS_2 is a material with high on/off ratios due to a sizeable band gap and high carrier mobilities.(*57, 174*) The first top-gated transistor based on micromechanical exfoliated single layer MoS_2 was shown by Kis et. al, as shown in Figure 9b. A significant high on/off ratio (~10^8) at a bias voltage of 500 mV (Figure 9c), n-type conduction, the room-temperature mobility of >200 $cm^2 \cdot V^{-1} \cdot s^{-1}$ in monolayer MoS_2 devices.(*57*) On the other hand, the field-effect-transistors based on MoS_2 produced by CVD exhibited n-type behaviors with the on/off ratio about 10^5 and electron mobility up to 6 $cm^2 \cdot V^{-1} \cdot s^{-1}$.(*170*) Flexibility and transparency are also promising characteristics of thin layers MoS_2 for next-generation electronics. Mechanical measurements performed on single-layer MoS_2 show that it is 30 times (effective Young's modulus of 270 ± 100 GPa) stronger than steel and can stand deforamtion up to 11% before breaking (breaking strength 23 GPa).(*175*)

2.3.2.2 Vibrational and optical and properties

Raman spectroscopy has been proved to be a very useful tool in the study of MoS_2. Typically, there are two peaks which correspond to the in-plane E^1_{2g} (382 cm^{-1}) mode (vibration of sulfur and molybdenum atoms in the crystal plane) and E_{1u} (IR active) phonon modes, and the out-of-plane A_{1g} (405 cm^{-1}) mode(that corresponds to the vibration of sulfur atoms out of crystal plane).(*176*) Additionally, positions of peaks depend on the layer of MoS_2, as shown in Figure 9e and 9f. As the layer decrease, the A_{1g} mode decreases in frequency whereas the E^1_{2g} mode increases. These relative peak position shifts allow the layer of MoS_2 thin flakes to be identified through Raman spectra, as shown in figure 9e and 9f. This is due to the Raman spectra is sensitive to the interlayer interactions in MoS_2 (e.g. effective restoring forces and long-range Coulomb interactions).(*177*)

In indirect bandgap semiconductors, the recombination of electrons and holes produced by photon energy occurs much less efficiently than that in direct bandgap semiconductors, since partial of energy has been consumed for the momentum transition .(*161, 173*) The indirect to direct bandgap transition and bandgap energy increase of MoS_2 is proven by the changes in photoluminescence absorption spectra (intensity and position) and photoconductivity.(*178, 179*) The strong photoluminescence of monolayer MoS_2, which shows the possibility of new optoelectronic applications.(*180*) A factor of 10^4 increase in photoluminescence quantum can be yielded from bulk to monolayer MoS_2. Furtherly, suspended monolayer MoS_2 shows even higher quantum yield. Typically, the optical photoluminescence spectrum of MoS_2 has two main peaks, the so-called A and B excitons (Figure 9 d), due to the direct-gap interband transitions at the K-point. (*178, 179,*

181) Further, multijunction solar cells structure could potentially be built based on TMDs with different thickness, with absorption spectra ranges from the visible to the near-infrared.(*182*)

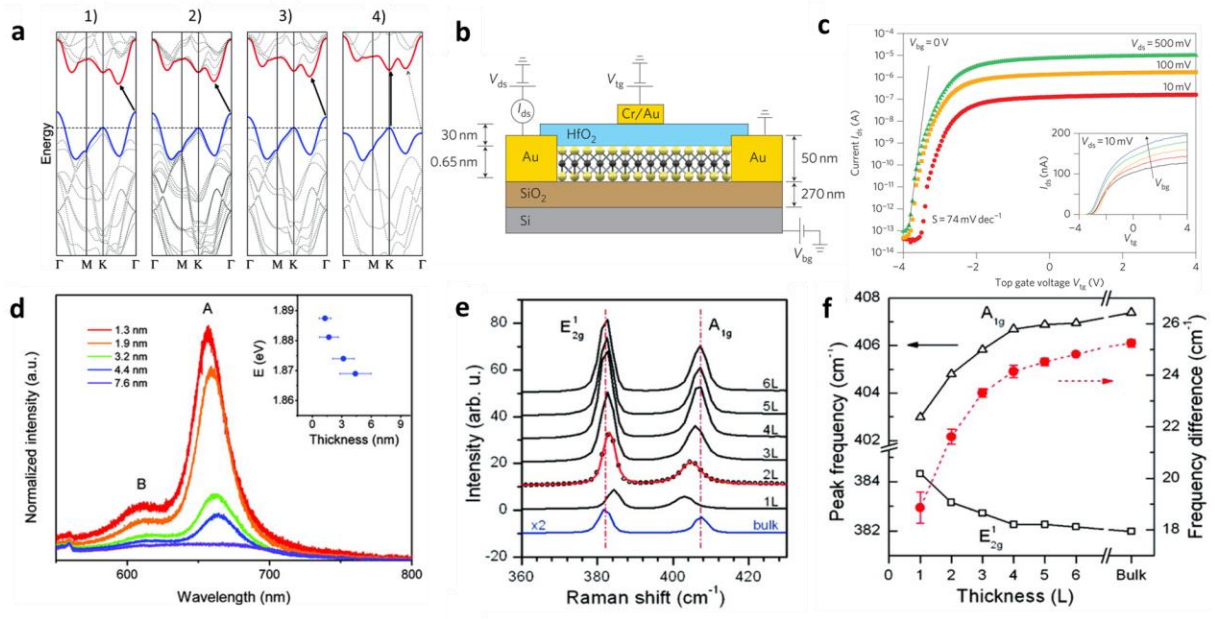

Figure 9. TDMs properties. (a) Calculated band structures of (1) bulk MoS_2, (2) quadrilayer MoS_2, (3) bilayer MoS_2, and (4) single MoS_2. The solid arrows indicate the band gap. (b) Cross-sectional view of the structure of a monolayer MoS_2 FET. (c) I_{ds}–V_{tg} characterizations (room temperature with the back gate grounded). (d) Energy of the A exciton peak for different average film thickness. (e) MoS_2 films Raman spectra as function of thickness. (f) Frequencies of E^1_{2g} and A^1_g Raman modes and their difference at different thickness. Nano Letters (2010) 4, 1271–1275; Nature Nanotechnology (2011) 6, 147–150; Nano letters (2011) 11,5111-5116; ACS Nano (2010) 5, 2695–2700.

2.4 Wrinkles and strain engineering in MoS_2

2.4.1 Wrinkles and strain introduction methods in MoS_2

Similar to the wrinkle introduction methods for graphene, there are various experimental methods and strategies for introduction of strain in MoS_2, such as (a) intrinsic thermal ripples, (b) thin film and substrate interactions (mechanical exfoliation and thermal annealing), (c) bending and stretching of flexible substrates, (d) relaxation of pre-stretched substrates, (e) substrate surface topography modification, and (f) pressurized blisters and tip indentation of suspended 2DNMs.

2.4.1.1 Intrinsic thermal ripples

Spontaneous ripples in MoS_2 was demonstrated experimentally and theoretically.(*183, 184*) Small ripples with length $L \approx 6-10$ nm and height $h \approx 6-10$ Å (typical ration of L/ h is ~10) are observed in mechanical exfoliated monolayer MoS_2.

2.4.1.2 Deformation of flexible substrates and thermal expansion mismatch

2DNMs have been transfer onto flexible substrates (PMMA, PDMS, and polycarbonate) for bendable electronics applications. By applying tensile stress or pressing on the two side of the substrates, MoS_2 experience the strain similar to that experienced by the substrate, assuming there is no relative slip.(*185*) For example, in one work MoS_2 thin films were mechanically exfoliated and deposited onto a layer of cross-linked SU-8 photoresist covered polycarbonate. Titanium clamps were then evaporated to prevent MoS_2 from slipping against the substrate. Uniaxial strain was applied to MoS_2 by controllably bending the polycarbonate substrate in a four-point bending apparatus, as shown in Figure 10c.(*186, 187*) Similar to the graphene wrinkle-engineering, MoS_2 thin

film was transferred on the pre-stretched substrates. The release of uniaxial tension in the elastomeric substrate enabled formation of well-aligned one-dimensional periodic wrinkles in the MoS_2. This method produces large-scale wrinkled MoS_2 (with micrometers in amplitude, tens of micrometers in wavelength) for thick MoS_2 flakes, while thin MoS_2 layers show smaller wrinkles that are between 50 and 350 nm in amplitude with wavelength of few micrometers (Figure 10a).(67) Here, the size of wrinkles can be controlled by tuning different parameters, like, the Young's modulus of the substrate, thickness of the thin film, and the interfacial adhesion between the thin film and substrate. In another process, MoS_2 on heated PDMS substrate causes thermal expansion of the MoS_2; however, due to its larger thermal expansion coefficient, the PDMS substrate can induce an additional biaxial strain in MoS_2. In comparison, smaller strain is induced in the reference samples with MoS_2 on SiO_2, which is due to the smaller thermal expansion coefficient of SiO_2 and smaller thermal expansion mismatch between MoS_2 and SiO_2. Laser beam can also be applied as a heat source to induce local heating and regionally controlled strain in the MoS_2; however, the maximum strain achieved by this method is small (~0.2%).(*188*) Chemical vapor deposition (CVD) is the most efficient and promising method to produce large area 2DNMs.(*9, 172, 189*) Because of different thermal expansion coefficients of substrates and MoS_2, non-uniform and local strain in the MoS_2 are expected to be formed during the CVD process. For example, it is proven that the tensile strains exist on CVD-grown MoS_2 and WS_2 on SiO_2, and these intrinsic strains in MoS_2 and WS_2 can be released after transferring to new substrates.(*190*) Using these strains, large scale bucked MoS_2 thin films were produced

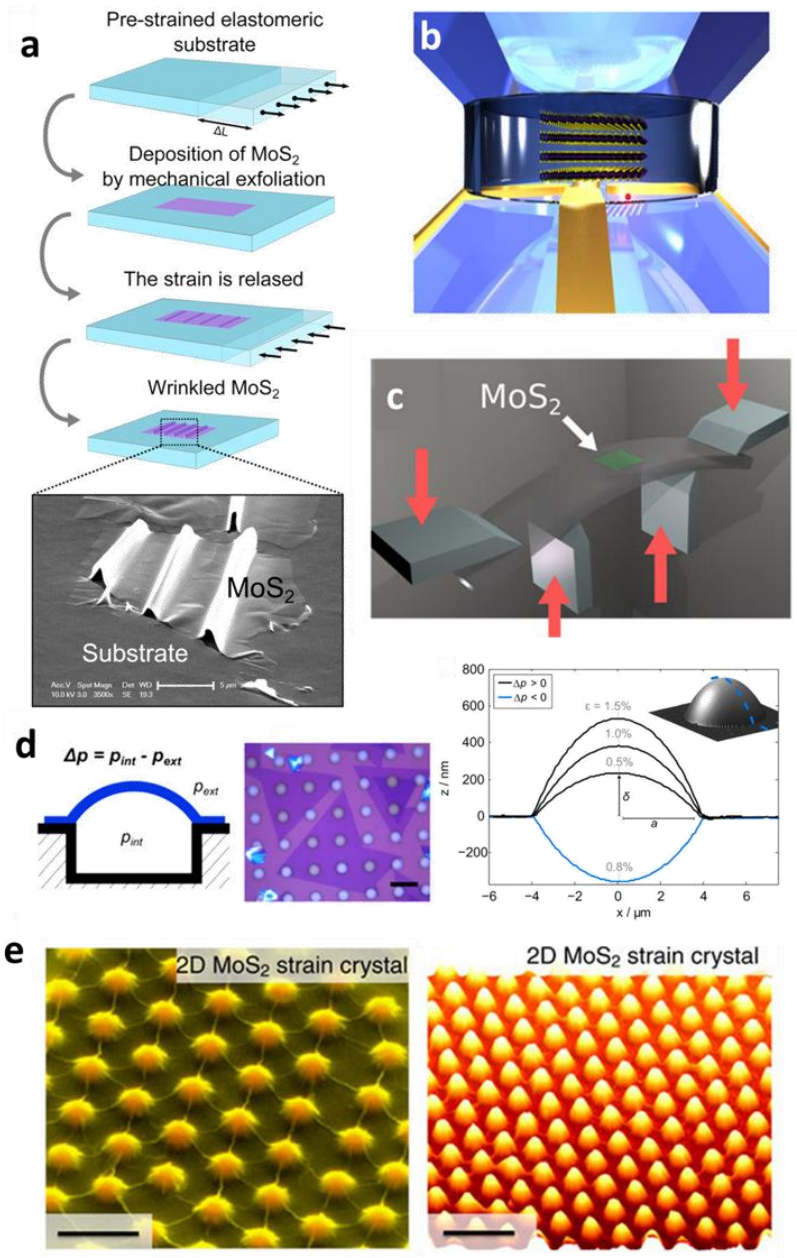

Figure 10. Wrinkles and strain engineering in MoS_2. (a) Schematic diagram of the fabrication process of wrinkled MoS_2 nanolayers by pre-stretched substrate method and a typical SEM image of winkle MoS_2 on elastomer surface. (b) A 3D illustration of bulk MoS_2 in a DAC pressure medium for hydrostatic pressure experiments. (c) Schematic of the straining MoS_2 device. (d) Schematic of MoS_2 pressure blister, a typical sample of CVD grownMoS_2 membranes suspended over cavities after transfer (scale bar is 20 μm), and an AFM cross section of a device at various pressure. (e) False-colour SEM image of the 2D strained MoS_2 (scale bar is 500 nm), and AFM image of the 2D MoS_2 strain crystal (scale bar is 1 μm). Nano Letters (2013) 11, 5361–5366; Nature Communications (2014) 5, 3731; Nano Letters (2016) 9, 5836–5841; Nature Communications (2015) 6, 7381.

by treating molybdenum metal thin films on graphene covered SiO_2 surface in sulfur atmosphere.(*191*)

2.4.1.3 Substrate surface topography modification

2DNMs are very thin (1 to 3 atomic layers), which means they are flexible enough to conform to most surface morphologies of the substrate under them. The relative strong interfacial adhesion energy between 2DNMs and substrate surface leads to strain accumulation near the protruding features on the substrate surface.(96) Therefore, the strain in the thin 2DNMs can be manipulated by tuning the attributes of these protruding feather (size, height, density, and shape). One of the examples is 'artificial atom', which is transferring monolayer of CVD produced MoS_2 on nanocones on the surface as shown in Figure 10e. The roughness of the substrate under 2DNMs plays an important role in the strain formation in the 2DNMs.(*192, 193*)

2.4.1.4 Pressurized blisters and tip indentation

The pressurized blisters method to study strain in 2DNMs was introduced by Bunch's group.(96) Mechanically exfoliated or chemical vapor deposited graphene or MoS_2 was transferred on pre-defined microcavities in oxidized silicon wafers (Figure 10d).(66, 96) Because of the excellent gas molecular impermeability of 2D nanomaterials, sealed micro cavities were formed. Samples were left in the pressure chamber at P_0 (outside pressure) for couples of days to make sure P_{int} (pressure inside the sealed micro cavities) equilibrates with P_0 through the slow diffusion of gas through SiO_2 substrate. The pressure difference ΔP between the environment (out of sealed micro cavities) P_{ext} and microcavities P_{int} deformed the 2DNMs and induced strong tensile strain in these thin

films when the samples were place in a different pressure chamber (P_{ext}). These pressurized graphene blisters were also applied to measure the adhesion energy between 2DNMs and silicon dioxides surface.(96, 99) The strain here is biaxial and relatively large (up to 5%).(66, 96) Similarly, mechanical strain can also be introduced in 2DNMs by atomic force microscope tips loading on suspended 2DNMs thin film (over two metal contacts or holes as shown in Figure 11d). This method is good for investigation of the mechanical properties of 2DNMs, like measurement of the Young's modulus and tensile stress. However, it may not be practical for device application. (*59, 76, 183*)

2.4.2 Properties modification of wrinkles and strain in MoS_2

2.4.2.1 Phonon vibration modification

The strain in 2DNMs introduces changes in the bond lengths and angles, and in some cases, lattice deformations. This structure modification under strain, in turn, leads to a considerable change in the lattice vibration (phonon), and this phonon frequency shift can be detected in Raman spectroscopy. When the uniaxial tensile strain is applied along the zigzag direction of MoS_2, the strain in zigzag direction can increases the bond lengths gradually, but the bonds lengths in the armchair direction decrease with strain, and further bond angle change, resulting in lattice distortion. Additionally, the intrisic structure of the monolayer MoS_2 could be maintained and no structural transformation appears at a large biaxial strain (up to 22%), but imaginary frequencies show up near Γ points when the strain is higher than 25%, indicating structural instability and possible structural transformation.(*194, 195*) Theoretically, the phonon mode shifts of the A_{1g} mode (out-of-plane) in MoS_2 is not sensitive to the uniaxial strain, even when the uniaxial strain is higher

than 20% in monolayer MoS_2, but it shifts to lower wavenumber significantly under biaxial strain. The frequency of the E^1_{2g} modes shows an obvious redshift under uniaxial and biaxial strain, since it is due to in-plane phonon vibration. Further, the asymmetrical shift of S-Mo-S bond in MoS_2 lattice under uniaxial strain induces a splitting of vibration frequency at point Γ, which leads to the E^1_{2g} mode splitting into two modes, as shown in Figure 11a.(*196*) This frequency splitting does not occur under the biaxial strain up to 5%, since the lattice symmetry is maintained in this case.(66) Further, both theoretical and experimental results have shown that the shift in the positions of Raman modes in MoS_2 linearly depends on applied strain, therefore, the strain in MoS_2 can be quantified in Raman spectrum.

In hydrostatic pressure study, MoS_2 undergoes a semiconductor-to-metal transition at a pressure range of 10-19 GPa. A_{1g} modes in Raman spectroscopy shown more drastic low position shift (blue shift) than that of E^1_{2g} modes in this transition pressure. At pressure higher than metallization pressure, E^1_{2g} and A_{1g} modes experience stronger but similar blue-shift than under lower pressure (Figure 11a). In contrast, when uniaxial or biaxial strains applied to thin layers of MoS_2, E^1_{2g} and A_{1g} modes are red-shifted (the vibrations soften) as shown in Figure 11a.

2.4.2.2 Electrical properties and photoluminescence modification

MoS_2 transistors exhibits a high on/off ratio exceeding 10^8,(*57*)and MoS_2 photodetectors show high responsivity.(*197*) Structurally, the π bond-like interaction between inter atomic layers in MoS_2 is strain-sensitive and leads to the reduced bandgap under strain.(*194, 198*) Since the direct gap energy is only slightly lower than the indirect gap energy in

monolayer MoS_2 in the density function theory (DFT) calculation,(*199*) relatively small tensile strains (~2%) can cause a direct to an indirect gap transition,(*200, 201*) which was proven in photoluminescence (PL) experiments. In this case, the intensity of monolayer MoS_2 decreases dramatically under strain. Even semiconductor-to-metal transitions at ~ 8% tensile strain or at ~ 15% compressive strain were shown in calculations.(*104, 185, 202*) Further, the direct bandgap structure of monolayer and bilayer MoS_2 has been unveiled to be highly sensitive to strain experimentally with showing a red-shift (Figure 6d, 6e and 6f) of absorption spectrum peaks and photoluminescence (~50 meV/% strain) for the uniaxial strain.(*185, 186*) Lloyd et al. recently reported that an up to 500 meV was tuned by large biaxial tensile strains (~5%) in a study of pressurized monolayer MoS_2 blisters. In this study, the in-plane strain has the ability to continuously and reversibly modulate the optical bandgap of monolayer MoS_2 by up to 25%.(*66*) Additionally, both theoretical and experimental results have shown that the shift in the photoluminescence energies of MoS_2 linearly depends upon applied strain, therefore, the strain in MoS_2 can be quantified in PL Spectroscopy. Therefore, strain engineering is promising for bandgap controlling and tuning in MoS_2 for novel electronic and optoelectronic applications. The strain in MoS_2 does not affect the exciton binding (the difference between the optical bandgap and transport bandgap), it is constant (~0.5eV) under a biaxial strain up 9%. However, the energies of electron and hole decrease monotonically with the increase of the strain. Feng et al. also proposed a solar energy funnel mode for devices design based on inhomogeneous mechanical strain in monolayer MoS_2.(*203*)

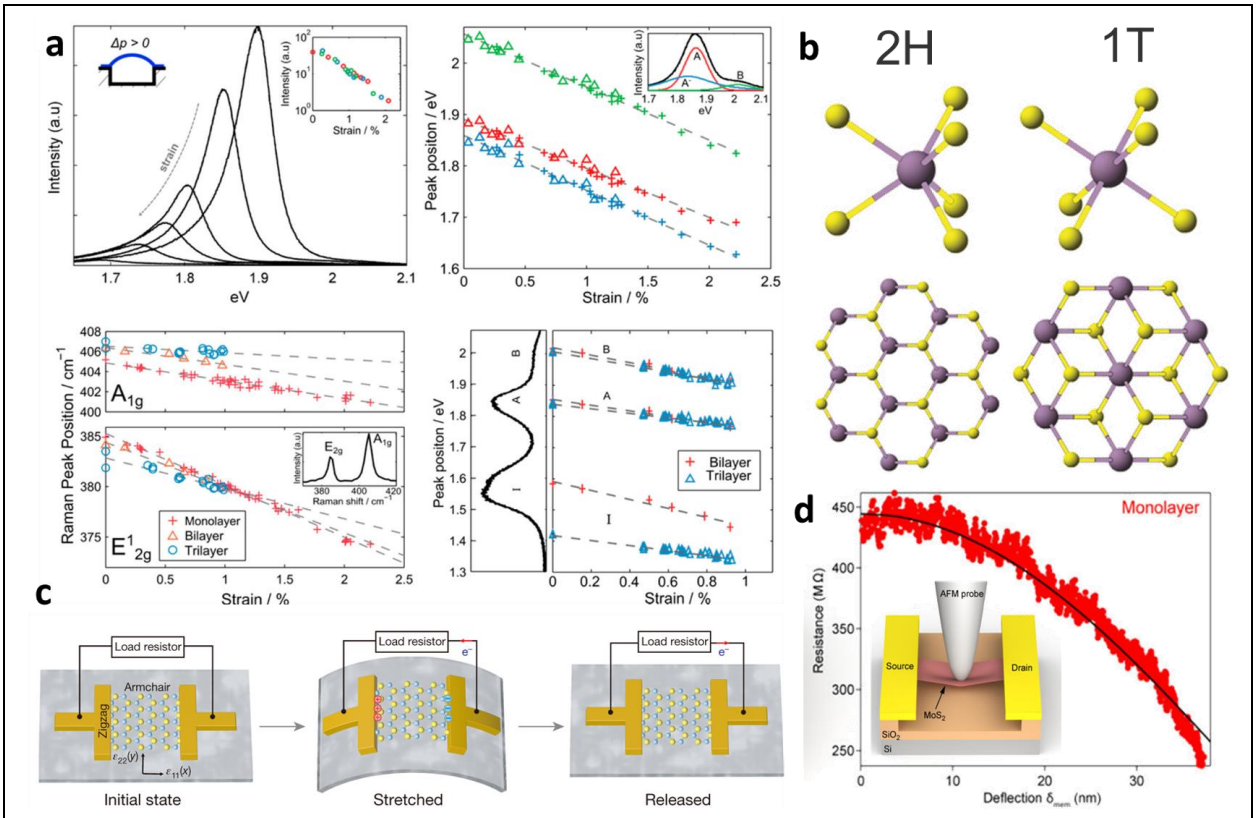

Figure 11. Raman, PL, and Piezo- and Flexoelectricity under strain. (a) The PL spectra intensity and position for monolayer MoS_2 at different biaxial strains corresponding to different pressure. The E^1_{2g} and A_{1g} Raman modes position as a function of biaxial strain for different membrane thicknesses. PL spectrum, and the peak positions of the A, B, and indirect I peak as a function of biaxial strain for different layers of MoS_2. (b) Crystal structures of the 2H and 1T phases, respectively. (c) Operation scheme of the single-layer MoS_2 piezoelectric device. (d) Schematic illustration of the setup for electrical characterization on suspended channel MoS2 devices under strain. Nano Letters (2016) 9, 5836–5841; Nature Materials (2014)13, 1128–1134; Nature (2014) 514, 470–474; Nano Letters (2015) 15, 5330–5335.

2.4.2.3 Phase modification

Besides the lattice vibration and electrical bandgap modulation, the polarization and phase properties are closely related to the lattice structure and symmetry, and are expected to be modified with the existence of mechanical strain. For example, the strain dramatically affects the polarization degree in MoS_2. When the strain is increased up to

0.8%, the PL polarization degree decreases 40% (from 10% to ~ 6%) in monolayer and ~ 100% (6% to ~ 0) in bilayer MoS_2.(*195*) TMDs can exist in multiple crystal structures, each with distinct electrical properties, and the two lowest energy crystal structures are often referred to as H and T.(*204-206*) The H phase is a semiconducting phase with for all Mo and W-based TMDs photon adsorption bandgap between 1 and 2 eV at ambient conditions.(*17*) The semi-metallic T phase has been found in lithium intercalated MoS_2.(*207*) Recently, theoretical calculations and experiments have shown that different stimuli, (*205, 207-209*) such as mechanical strain could induce phase transformation in 2D TMDs. Elastic deformations in monolayers of TMDs can be reached through tensile strain and leads to TMDs phase transformations between semiconducting 2H and metallic 1T' structures (1T' structures can be thought of as 1T after a symmetry-reducing distortion).(*210, 211*) Additionally, $MoTe_2$ needs much lower strain (tensile strain of 0.2%) than other TMDs for the phase transition.(*205, 212*) This strain induced phase transition may lead to controlled phase production in TMDs synthesis process.

2.4.2.4 Piezoelectric and flexoelectric properties

Piezoelectric property (PE) represents the ability of materials to generate electric charges under mechanical stimuli. Flexoelectric property (FE) is an extension of the PE, where PE linearly relates uniform strain to polarization and FE connects strain gradients to polarization.(*213*) These two electromechanical effects have been widely applied in sensors, transducers, power generation and electronics.(*76*) For example, Wu et al. have shown the first experimental study of the PE of MoS_2 and demonstrate that only odd

number of atomic layers produces oscillating piezoelectric voltage and current outputs (Figure 11c).(*214*)

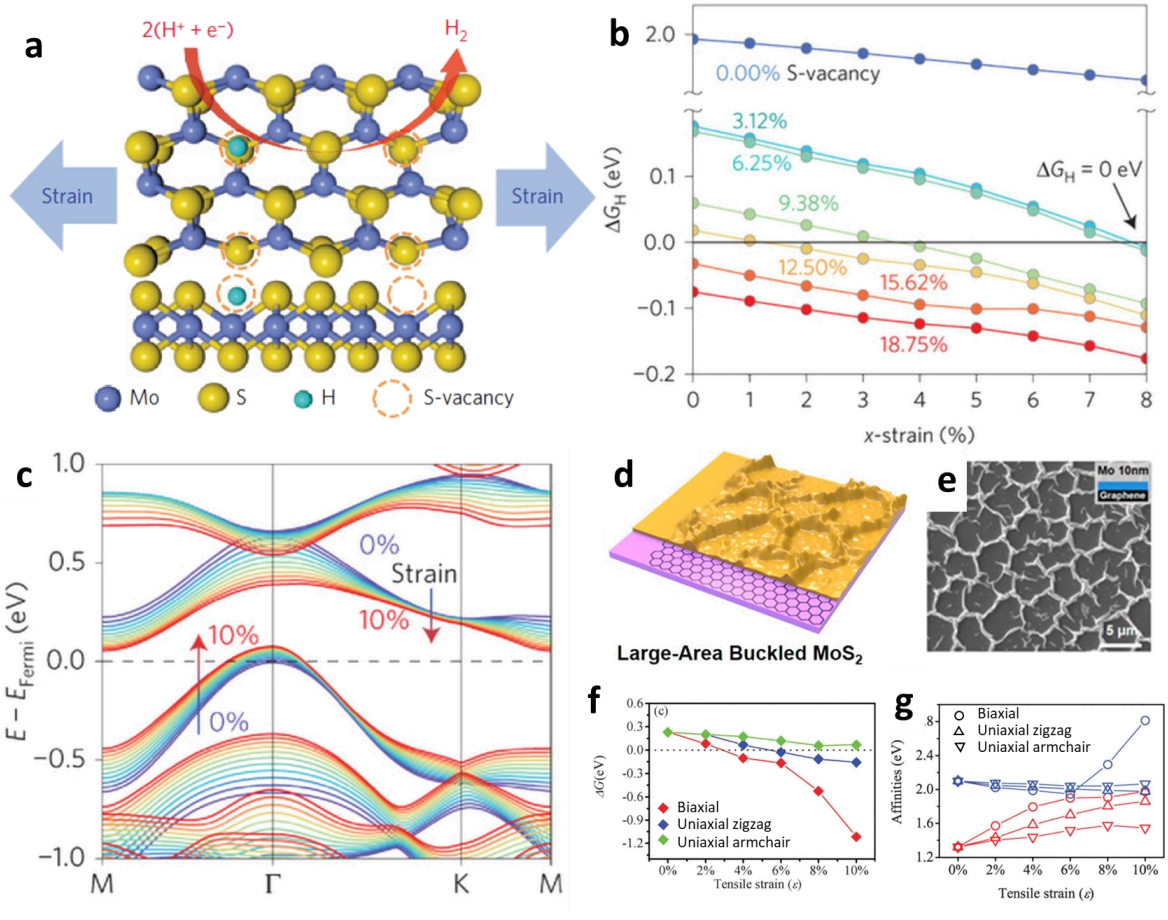

Figure 12. **Enhancement of chemical activity of strain in 2DNMs.** (a) Schematic of the applied strain further tunes the HER activity of MoS_2 (S-vacancy), (b) Hydrogen adsorption free energy ΔG_H evolution with strain at various S-vacancy; (c) Band structure for 25% S-vacancy under applied strain. Strain induces a narrow bandgap; Adapted with permission. Schematic illustration (d) and SEM image (e) of buckled MoS_2 films on graphene; Adapted with permission. (f) Gibbs free energies of H adsorption for monolayer 1T-MoS_2 as function of tensile strain; (g) Adiabatic electron and proton affinities of monolayer 1T-MoS_2 as functions of tensile strain. Nature Materials (2016) 15, 48-53. ACS Applied Materials and Interfaces (2016) 21, 13512-13519. Physical Chemistry Chemical Physics (2016) 18, 9388-9395.

2.4.2.5 Chemical activities modification

The strain in MoS_2 has shown selective enhancements on the adsorption of different gas molecules (enhanced adsorption of NO and NH_3) but insensitive to the adsorption of NO_2, CO, and CO_2. This contrasting behavior may lead to new design strategies for constructing ultrahigh-sensitivity sensors and electromechanical devices based on strain engineering of 2DNMs.(*215*) Monolayer 2H-MoS_2 has been reported to be promising catalyst for hydrogen evolution reaction (HER) by introducing Sulphur (S) vacancies and strain (Figure 12a and 12b). This is due to that new bands introduced by S-vacancies and reduction of the bandgap in MoS_2 under strain (Figure 12c).(*216*) The water-splitting catalytic ability of the buckled MoS_2 films showed a reduction of onset potential compared to unstrained MoS_2, as shown in Figure 12d and 12e.(*191, 217-220*) Tensile strain activates the inert inner valence electrons and enhances the exchange splitting of d-band as shown in electronic structure calculations, and induces an increase in the adiabatic electron affinity and a reduction of the adiabatic proton affinity, and further, enhances the catalytic activity of the system. It is found that biaxial tensile strain exhibits high enhancement on the HER activity than uniaxial tensile strain, while compressive strain decreases the HER activity (Figure 12f and 12g). Similar effect was also shown in the simulation of 1H-NbS_2.(*217*) Additionally, the local strain (the top and bottom peaks of the ripples) also shows a great enhancement of chemical activities of the phosphorene.(*220*)

Table III. Summary of strain introduction and properties modification in MoS_2.

Strain introduction	**Properties modification**
Simulations:	Phonon vibration softening(*66, 67, 185, 186, 195, 200*)
DFT(*221*), *Ab initio*(*222*)	Thermal conductivity(*186*)
Experiments:	Direct-indirect transition(*200, 201*)
Thermal vibrations(*183*)	Semiconductor-metal transition(*104, 185, 202*)
Surface adhesion(*193*)	Electron and hole energy reduction(*203*)
Thermal expansion mismatch(*188*)	Pl polarization decrease(*195*)
Substrate deformation(*185, 186*)	Chemical activity enhancement(*216, 217*)
Prestretched substrate(*67*)	Carrier's mobility modification(*222*)
Pressurized blister(*66*)	
Substrate topography modification(*223*)	

3. METHODOLOGY

3.1 Wrinkles in thin films

3.1.1 Wrinkles formation in thin metal films

To produce the wrinkles, metal was deposited on thermally expanded silicone oil drops and lines (*85, 224*) with low vapor pressure. The temperature rise in the silicone oil drops/lines ($\Delta T \sim 80$ °C) was achieved by the metal deposition process, whereupon cooling silicone oil contraction led to the formation of wrinkles. The metal deposition was tested for sputtering and e-beam evaporation. When metal was sputtered on the silicone oil, grainy and porous films were formed due to ion bombardment. The resultant structural defects and internal stresses led to random cracks and crumples. Electron beam evaporation produced uniform (nongrainy) metal deposition on liquid silicone oil at a controlled rate (1 Å/s). The silicone oil lines and drops were predeposited on the silicon dioxide surface, as shown in Figure 12. To ensure adhesion, 30 nm of chromium thin film was deposited at a base pressure of 5×10^{-7} Torr. The chromium layer improves the adhesion of the cobalt layer to silicone oil and to the SiO_2 surface. This was followed by evaporation and deposition of cobalt thin films (300, 100, and 50 nm). Thicknesses of the metal layers were measured by crystal oscillators in the electron beam evaporation process. The substrate temperature was kept at about 100 °C. Without the predeposited chromium layer, the cobalt layer breaks during the deposition process, attributed to metals' (especially noble metal) poor adhesion to the SiO_2 surface. This intimate contact or adhesion of cobalt thin film with the silicone oil and SiO_2 is essential to form well-controlled wrinklons at the edge of the meniscus.

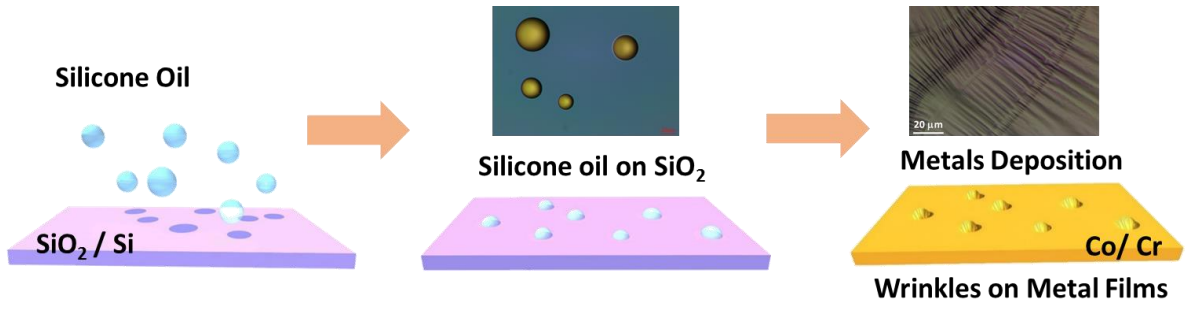

Figure 13. Schematic of fabrication of hierarchical wrinkles in thin metal films.

3.1.2 Wrinkles in MoS_2 for adhesion energy study

The study was conducted on silicon dioxide and silicon nitride substrates. The wafers were diced into about 1×1 cm^2 pieces, cleaned with acetone and isopropanol, and dried with air. MoS_2 sheets were mechanically cleaved from the surface of MoS_2 Block (SPI) by scotch-tape peeling. To transfer the MoS_2 flakes on SiO_2, the tape (width of 1 cm) was lightly pressed onto the MoS_2 block (about 0.3×0.3 cm^2), and then separated slowly. This transferred thick flakes on the tape. The tape with the flake was then brought in contact with the SiO_2 or Si_3N_4 substrate in dry condition and a small pressure is applied for 10 seconds. Finally, the pressure for released and the tape was quickly peeled off resulting in MoS_2 deposition on the substrate. The adhesion forces (van der Waals) pulled the MoS_2 sheets into intimate contact with the substrates. Mechanical equilibrium was reached when the MoS_2 contracted to form the wrinkle in MoS_2. The interfacial adhesion energies of MoS_2 and substrates were found by measuring the wrinkles size (amplitude, wavelength, and thickness of the MoS_2 flakes). Atomic Force Microscope was applied to measure the topography of the substrates and MoS_2 flakes thickness and wrinkles attributes. The resolution of the AFM in the z-direction is 0.1 nm (for thickness and

amplitude) and in the lateral direction is about 10 nm (for wavelength). Strain measurement was achieved in Raman Spectroscopy.

3.2 Wrinkled graphene on bacteria

3.2.1 Graphene growth and transfer

In this step, the high-quality monolayer graphene sheet is laid on top of the bacterial cells. Here, graphene is grown via chemical vapor deposition (CVD) process on a copper foil (25 μm) at 1000 ^{0}C with purging CH_4/H_2 (100/10 sccm) in a one-inch quartz tube for 5 min. A layer of PMMA is then spin-coated (20%PMMA at 4000 rpm for 1min) on graphene (on Cu foil), followed by dissolving the copper foil in 30% nitric acid. The PMMA-graphene composite film which floats on the top was transferred to a water bath to get rid of the acid residues. The film is then carefully transferred onto the bacterial chip prepared in the previous step. This is followed by the removal of the PMMA layer (1/3 IPA in acetone solution wash, 60 ºC for 4-5 min) to produce graphene wrapped bacteria immobilized on the chip.

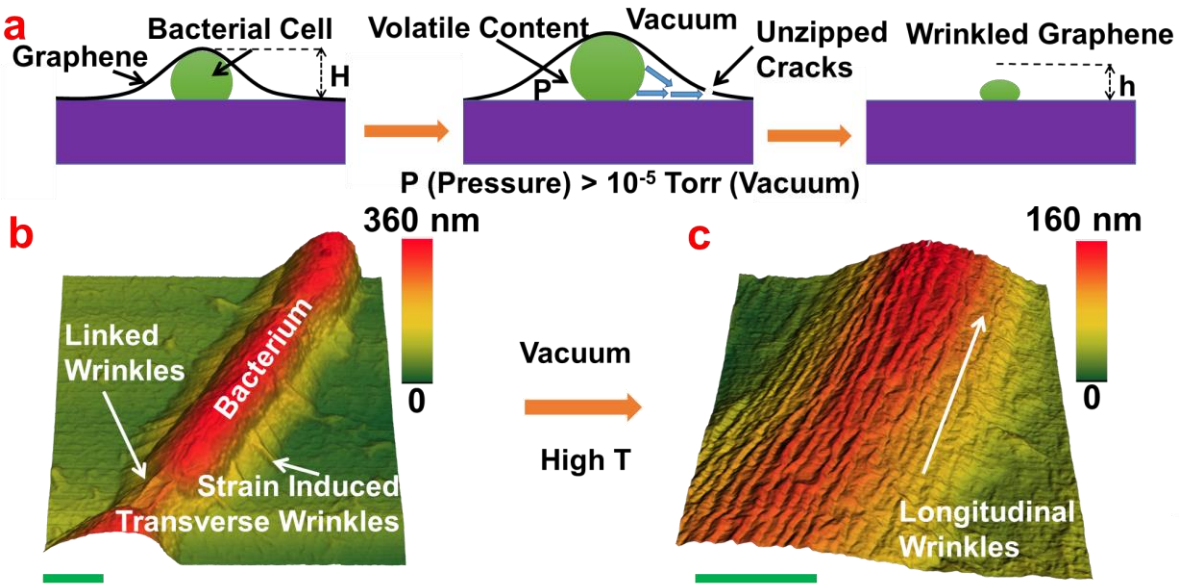

Figure 14. Graphene on bacteria process. Schematic of the wrinkles formation process on graphene via check valve actuation. (a) Cross-sectional schematic of bacterium covered graphene sample, which under vacuum bulges and undergoes unzipping. The graphene then a check valve to remove aqueous content of bacteria, subsequently contracting it to produce wrinkles (10^{-5} Torr and 250 °C). (Bottom) High magnification 3D AFM surface morphology images of graphene on bacteria before (b) and after heat/vacuum process (c). The scale bars in (b) and (c) are 0.5 μm. Copyright 2016 American Chemical Society.

3.2.2 Bacteria preparation

Rod-shaped, gram-positive *bacillus subtilis* (0.5 to 1.5 μm and in length from 1 to 5 μm) were used in this study. *Bacillus subtilis* (from ATCC) were grown in agar gel and care was taken to ensure there is no cross-contamination. A pellet of *bacillus cereus* cells was introduced into 100 mL of nutrient broth solution (0.13 g/ml nutrient broth (OXOID) sterilized in an autoclave at 121 ºC for 12 min) in an Erlenmeyer flask using a sterilized culture-transfer rod. The flask was sealed with cotton and placed in an incubator to grow

the culture at 31.0 ºC for 14-15 hours (shake frequency = 62 rpm). After the growth period, the bacterial cells were separated from the medium by centrifuging the suspension at 6000 rpm for 10 min and re-suspending the pellet in DI water. This was repeated three times to remove the nutrient broth from the bacterial suspension.

A fresh chip (285 nm silica-on-silicon substrate) was sequentially washed with acetone, isopropyl alcohol, and DI water and was dried under N_2 flow. The pre-washed chip was exposed to oxygen plasma (0.0058 psia, 100 W, 2 min) to ensure a very clean surface. The chip was then immersed in the bacterial suspension (in DI) for about 1 hour, followed by carefully washing and drying in N_2 flow. This leads to bacterial cells adhering to the substrate by excreting extra-cellular polysaccharides, which bind them on the surface.

3.2.3 Annealing process

Here, the sample was exposed to vacuum and high temperature to trigger the wrinkle formation process. For this, first, the CVD tube was flushed with H_2 gas (100 sccm) for 15min. The chip (from step 3 having bacteria covered by graphene) was placed into the vacuum chamber and the temperature was raised to 250 ºC. The sample was kept at this condition for 3h, as shown in Figure 13.

3.2.4 Electrophoretic trapping for bacteria deposition

A droplet of diluted bacteria solution (same solution from step 1) is placed in the region between the electrodes by using a syringe. These two electrodes were connected to the AC signal source generator (Agilent 33220A) through two metal probes. An AC signal with a peak-to-peak voltage (V_{pp}) of 10 V and frequency (f) of 5 MHz was applied on the

ensemble for 5 to 10 min. The bacteria are forced to move along with the electronically filed lines towards the electrodes and gets trapped between the electrodes.

3.2.5 Plus-sharp devices fabrication

Photoresist was spinning coated on samples at 4000 rpm for 40 seconds, followed by soft baking at 110 ºC for 1 min. Samples are aligned and exposed in MA6 Mask Aligner with hard contact for 12 seconds at 900 W UV power. The exposed samples were developed in the developer for 12 seconds. O_2 plasma was performed on this developed samples to remove the uncovered graphene, and followed by immersion in etcher for 5 min. Finally, samples are washed and cleaned in DI water.

3.3 Wrinkled MoS_2 devices

3.3.1 Wrinkled MoS_2 preparation

The study was performed on MoS_2 exfoliated on silicon dioxide (285 nm silicon dioxide on silicon) substrates. MoS_2 sheets were cleaved by Scotch tape from the surface of MoS_2 Block (SPI). The wafers were diced into about 1×1 cm^2 square pieces, followed by cleaning with acetone and isopropanol, and dried with Nitrogen gas. The tape attached with small flakes of MoS_2 was brought into contact with SiO_2 substrates in dry condition, and a slight pressure was applied for 10s. Then, the tape was quickly peeled off, resulting in MoS_2 deposition on the SiO_2 surface. The van der Waals force between flakes and substrates surface pulled the MoS_2 sheets to have intimate contact with the substrate and separate the attached flakes from the rest of MoS_2 on tape. Therefore, there is no tape residues and tape-induced electrostatic charge at the MoS_2/SiO_2 interface or MoS_2/air interface. During the release of the tape, adhesion between tape and MoS_2 induces partial

delamination of MoS_2 from the substrate leading to the bending and wrinkling of MoS_2. Energy equilibrium was reached when the MoS_2 contracted to form the wrinkles in MoS_2. One in ten time the sheet had wrinkles. The topography of the wrinkles on MoS_2 was characterized by atomic force microscope (AFM) (WiTech Alpha-300-RA) and scanning electron microscopy (FESEM) (Raith). Raman and photoluminescence spectra and position mapping were also collected by WiTech Alpha-300-RA (All the Raman and photoluminescence characterizations were performed at room temperature).

3.3.2 Wrinkled MoS_2 devices fabrication

For device fabrication, the source and drain regions were defined by laser pattern generator (LW405) followed by electron beam evaporation to deposit 10nm/60nm of Titanium/Gold. Photoresist (S1805) was spinning coated on samples at 4000 rpm for 40 seconds, followed by soft baking at 110 ºC for 1 min. The detail of device fabrication process and electrical characterization setup are shown in Figure 14.

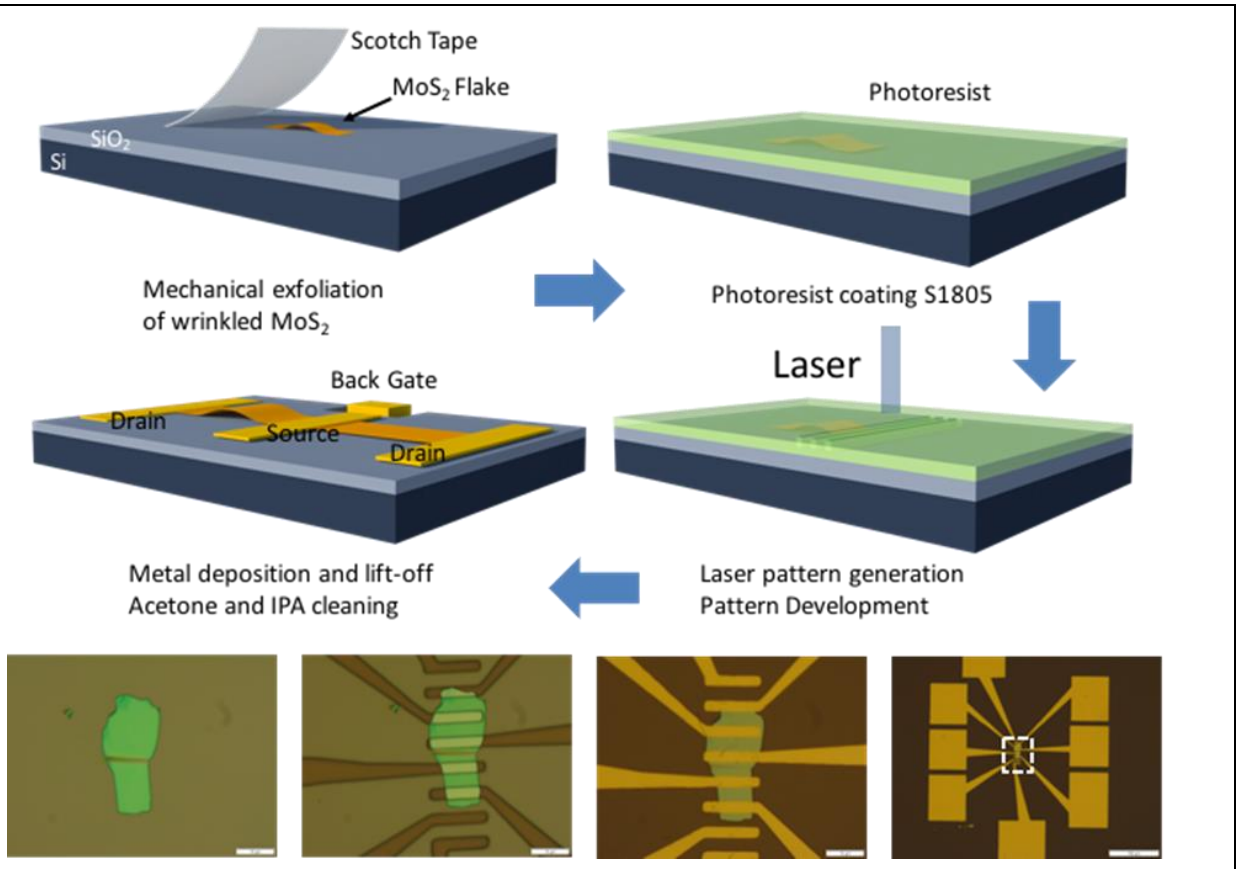

Figure 15. Schematic illustration and optical images of the device fabrication process.

4. RESULTS AND DISCUSSION

4.1 Wrinkles in thin films and adhesion energy

4.1.1 Wrinkles in thin films

The mechanism of wrinkle formation on metal deposited via electron beam evaporation on silicone oil was studied by optical and atomic force micrographs shown in Figure 16 and Figure 17. A thin chromium layer thinner than 20 nm does not fully cover the silicone oil, and a chromium layer thicker than 40nm crumples randomly. A layer of 30 nm thick Cr film can completely cover silicone oil with limited crumples. The difference in the surface energies of metal interfaced with silicone oil and with the substrate induces surface stretching at the edge, which in turn modified the wrinkling of the metal. The limited expansion of a small silicone oil drop (diameter smaller than 50 μm) restricts wrinkle formation. For larger oil drops with a long straight edge (longitudinal drop) or circular edges, the oil expands more to spread (slight delamination) and stress the metal film. The spreading causes the height of oil meniscus to decrease with an increase of its area on the substrate. The wrinkles form on metal thin film from the edge to the center of the oil (in the x direction) after cooling as shown in Figure 16b and 16c.

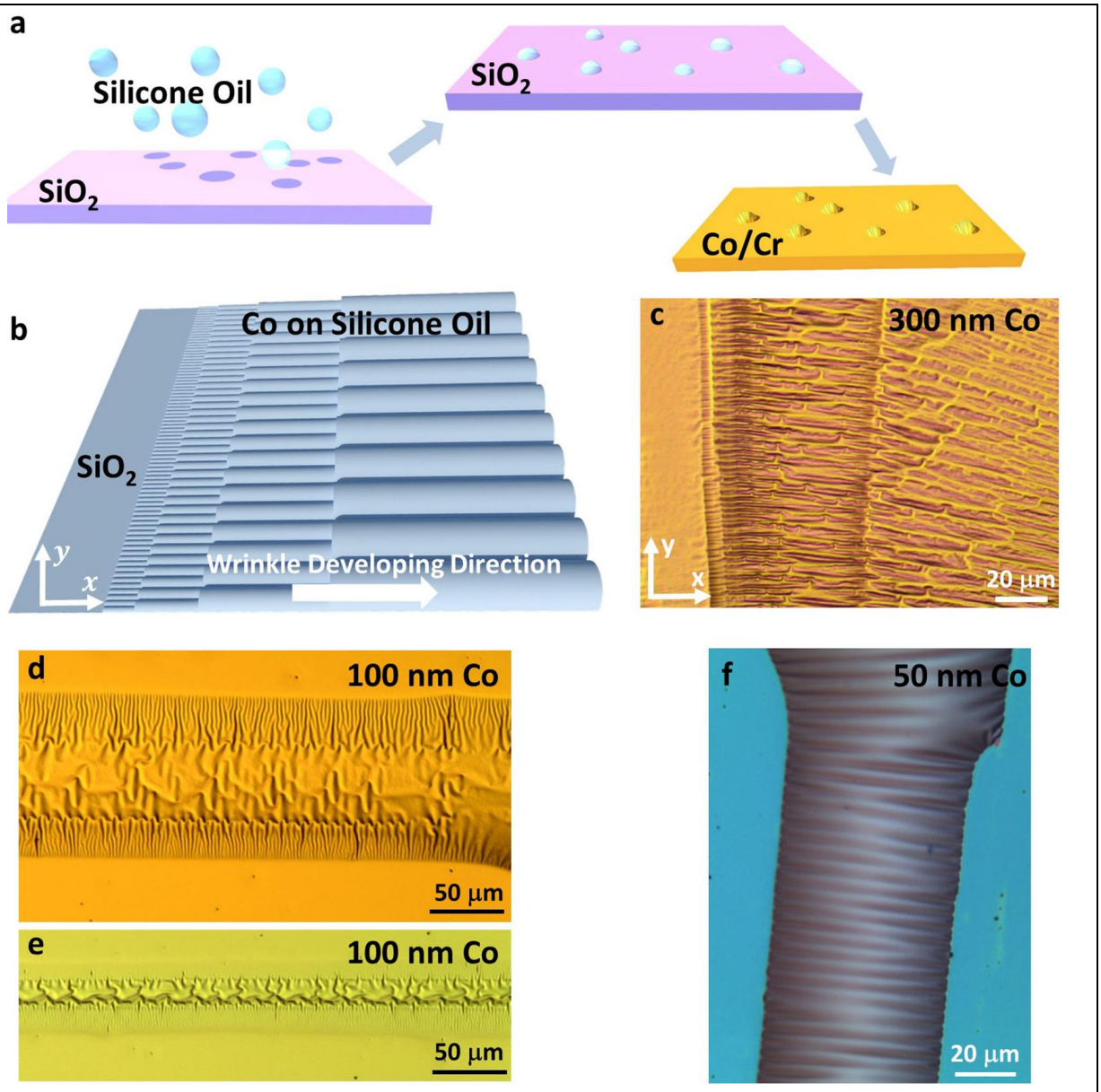

Figure 16. Schematic and optical images of the wrinkle formation on silicone oil. (a) Schematic of wrinkles on the metal thin-film formation process. (b) Schematic of hierarchical wrinkles. (c) Optical image of self-similar hierarchical wrinkles; cobalt thin-film thickness is 300 nm. (d) and (e) Optical images of hierarchical wrinkles on different sizes of silicone oil lines with 100 nm of thickness of cobalt. (f) Optical image of hierarchical wrinkles on silicone oil line with 50 nm thickness of cobalt. Copyright 2016 American Chemical Society.

Atomic force microscope surface profiles were acquired (Figure 17) to study the structural details of the wrinkles at high resolution. The wrinkles on metal films present a hierarchical

cascading step from the metal-oil-substrate edge to the center of the oil region. Smooth coverage (x direction) was observed on the top surface of oil since the penetration distance (x) is limited by an edge-induced surface energy effect (as shown in Figure 16d). The thickness of the metal thin film as well as the footprint of the silicone oil increase after metal deposition due to the associated temperature rise and expansion.(*85*) After contraction, the surface stretch from the metal-SiO_2 interface at the edge into the silicone oil drop leads to wrinkles.

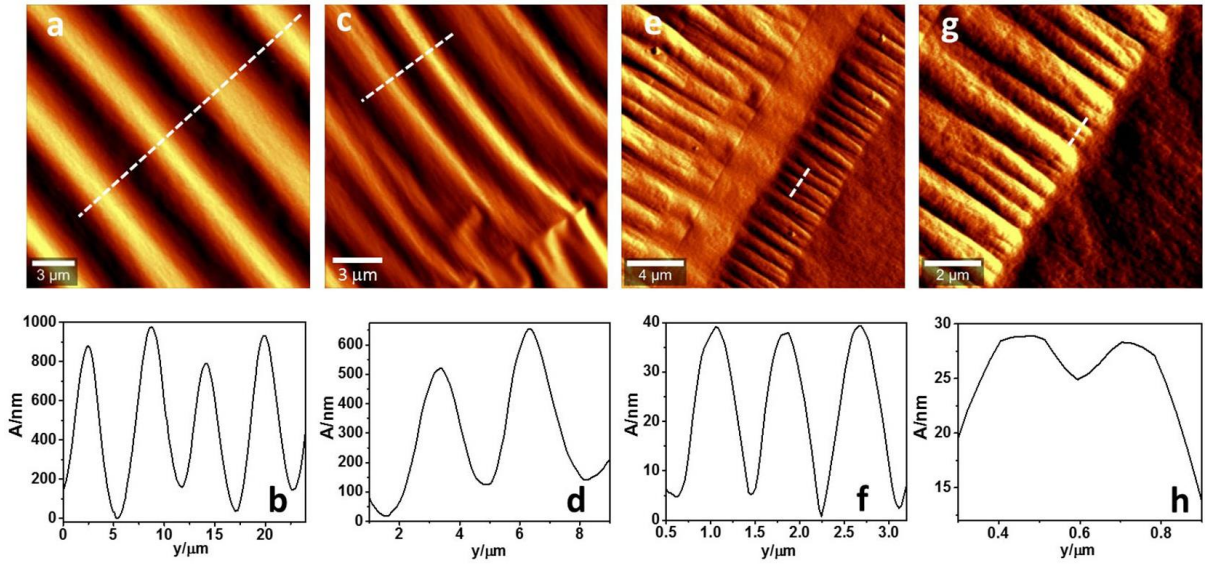

Figure 17. AFM images and height profiles of the wrinkled metal thin film surface. Left to right, parallel wrinkles in the bulk and hierarchical wrinkles on the edge. (a) and (b) wrinkles in bulk region with wavelength of about 6 μm, (c) and (d) hierarchical wrinkles near the bulk region with wavelength of about 3.5 μm; (e) and (f) hierarchical wrinkles near the edge with wavelength of about 1.0 μm; and (g) and (h) hierarchical wrinkles on the edge with wavelength of about 0.3 μm. Copyright 2016 American Chemical Society.

The evolution of the average wavelength λ with the distance from the constrained edge x is described by a power law: $\lambda \sim x^n$ with n as the power exponent.(*83, 225*) For our data,

n = 0.42 as shown in Figure 18a. However, instead of a continually increasing wavelength in the power law, the wrinkles exhibit a constant wavelength over a distance before transitioning to the next hierarchical wavelength (Figure 18b). The typical wrinklon hierarchy:(*18, 19, 27, 28, 85, 226*) $\lambda_{n+1} = 2\,\lambda_n = 2^{n-1}\,\lambda_1$ ($n \geq 1$) is clearly shown in the relative wavelength (λ/λ_1) versus number of transition of wrinkle pattern on thin metal film (Figure 18c). Further, the size of the drops or lines also affect the number of transition as shown in Figure 15. For soft film,(*83*) wrinklons exhibited a longer transition zone where two wrinkles of wavelength λ merge into one of width 2λ. The wrinklon transition in previous studies requires a distortion of the membrane, which relaxes over a distance (l). However, in our case with stiff metal, this transition range is small and the wrinkle-patterns keep a constant wavelength for different lengths before transitioning to the next wavelength.(*83, 227*) Additionally, no wrinklons were observed in the bulk regions away from the edge,(*19, 24, 31*) the wavelength reaches its maximum or equilibrium value, indicating the influence of interfacial stretch effect only near edges. Therefore, length of wrinklon (l) does not follow a clear global trend in rigid metal thin film. We further modify the definition of wrinklon length to the complete length of the region with one wrinkle-wavelength. Therefore, the wrinklon length $L = L(C) + L(T)$, where $L(C)$ is the length of the constant wavelength region and $L(T)$ is the length of transition region. It should be noted that for thin films interfaced with a fluid,(*18*) $L(C)$ and $L(T)$ can have varied relative scales. In our case $L(C) \gg L(T)$, or $L(T) \sim 0$ (Figure 18d). In wrinklon theory, the normalized length of the wrinklons, l/λ is a function of its normalized amplitude, A/t, with t is thickness of thin film: $L/\lambda \sim (A/t)^{0.5}$. For our data (hierarchical wrinkles), the exponent

is 0.31 instead of 0.5: $L/\lambda \sim (A/t)^{0.31}$ (Figure 18a). This deviation is attributed to the energy involved in the formation of wrinkles as shown later.

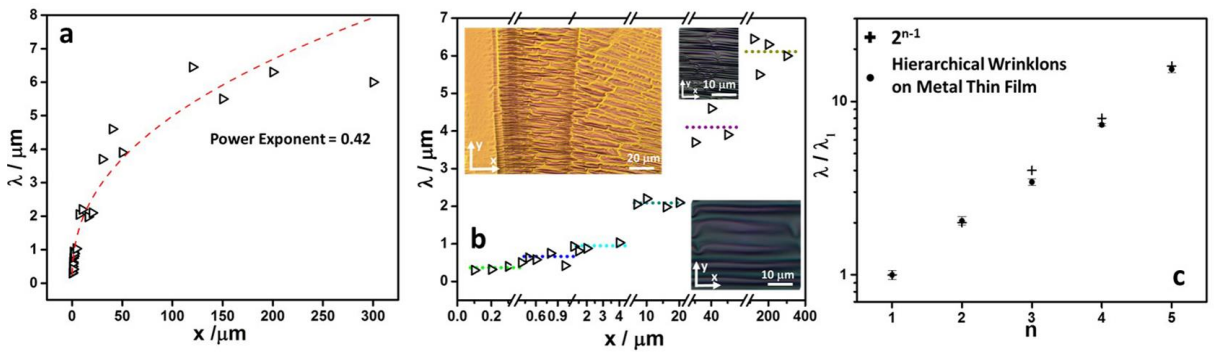

Figure 18. Evolution of the wavelength λ with the distance x from the constrained edge and the relative wavelength versus number of wrinklon transitions on thin metal film. (a) Evolution of wavelength in continuous x scale, which is fitted by a power equation and power exponent of the fitting is 0.42. (b) Evolution of wavelength in hierarchical x scale, and inserts are optical images for corresponded wavelengths. (c) The relation between the relative wavelength (λ/λ_1) and the number of wrinklon (n). λ_1 is the smallest wavelength on the boundary of oil drops. Copyright 2016 American Chemical Society.

We employ scaling arguments and energy balance to investigate the features of the hierarchical patterns. The total energy (U_T) of the wrinkled system of thin metal film on oil drop can be represented as following equation:

$$U_T = U_B + U_G + U_{Th} + U_s \quad (3)$$

Where, U_B is the bending energy for wrinkles formation in thin film, U_G is the gravitational energy of silicone oil, U_{Th} is the thermal expansion energy of silicone oil, and U_S is the surface energy applied on the metal thin film from the metal/silicon dioxide interface to metal/silicon oil interface.

The edge constraint along the x direction (Figure 16) results in expansion restricted along the y direction resulting in wrinkles forming parallel to the x direction. The film strain is defined as $\Delta = (W_0 - W)/W_0$, $\Delta \ll 1$ where W_0 and W are the original and projected widths of metal film, respectively. The wrinkle-surface height (z) along the y direction, at certain distance x from the edge can be simplified to be a sinusoidal function:(*18*)

$$z\,(x,y) = \frac{\lambda_n}{\pi}\sqrt{\Delta}sin(\frac{2\pi}{\lambda_n}y) \text{ at certain } x \quad (4)$$

This gives $\Delta \sim \left(\frac{A}{\lambda}\right)^2$ since the amplitude (A) of the wrinkles can be written as $A = \frac{\lambda}{\pi}\sqrt{\Delta}$. The wrinkling of the thin film along y direction is characterized by the curvature $\kappa \approx \frac{\partial^2 z}{\partial y^2} \sim \frac{A}{\lambda^2}$, since z is of the order of A and y is of the order of λ varying in x direction but not y. Further, we assume that the characteristic area is $L\lambda$. The bending energy(*83*) is $U_B = L\lambda E t^3 \kappa^2 \sim L\lambda^{-1} E t^3 \Delta \pi^{-2}$, where E is the Young's modulus. The gravitational energy(*18*) $U_G = L\lambda\rho g z^2 = L\rho g \lambda^3 \Delta sin^2\left(\frac{2\pi}{\lambda}\right)\pi^{-2}$ and the thermal expansion cenergy(*28*) is $U_{Th} = L\lambda\frac{1-\upsilon}{E}\sigma_0^2 t$, where, υ is the Poisson's ratio of the thin film and thermal compressive stress is $\sigma_0 = \frac{E}{1-\upsilon}(\alpha_s - \alpha_t)(\Delta_T) \approx \frac{E}{1-\upsilon}\alpha_s(\Delta_T)$, where α_s and α_t are thermal expansion coefficient of silicone oil and thin film, respectively ($\alpha_s \approx \alpha_s - \alpha_t$, since $\alpha_s \gg \alpha_t$). The mismatch of thermal expansion between cobalt and silicone oil is about 7.6 X 10^{-4} K^{-1}, which is much larger than the mismatch between the cobalt and chromium (6 X 10^{-6} K^{-1}). Therefore, we used the cobalt and silicone oil (7.6 X 10^{-4} K^{-1}) in the calculation and analysis; and Δ_T is the change of the temperature in the deposition process (Δ_T ~ 80°C), so thermal expansion energy $U_{Th} = L\lambda\frac{E}{1-\upsilon}\alpha_s^2(\Delta_T)^2 t$. It should be noted that Young's modulus of

metal film is much higher than that of soft polymer materials.(*43*) Surface energy(*18*) is given by $U_S = \frac{1}{2}Et(\frac{\partial z}{\partial x})^2 L\lambda$, where $\frac{\partial z}{\partial x}$ is the pseudo-strain(*83*) in x direction is of the order of $\lambda^2 \Delta / L^2$. This gives $U_S = \frac{1}{2}Et\lambda^5 \Delta^2 L^{-3}$.

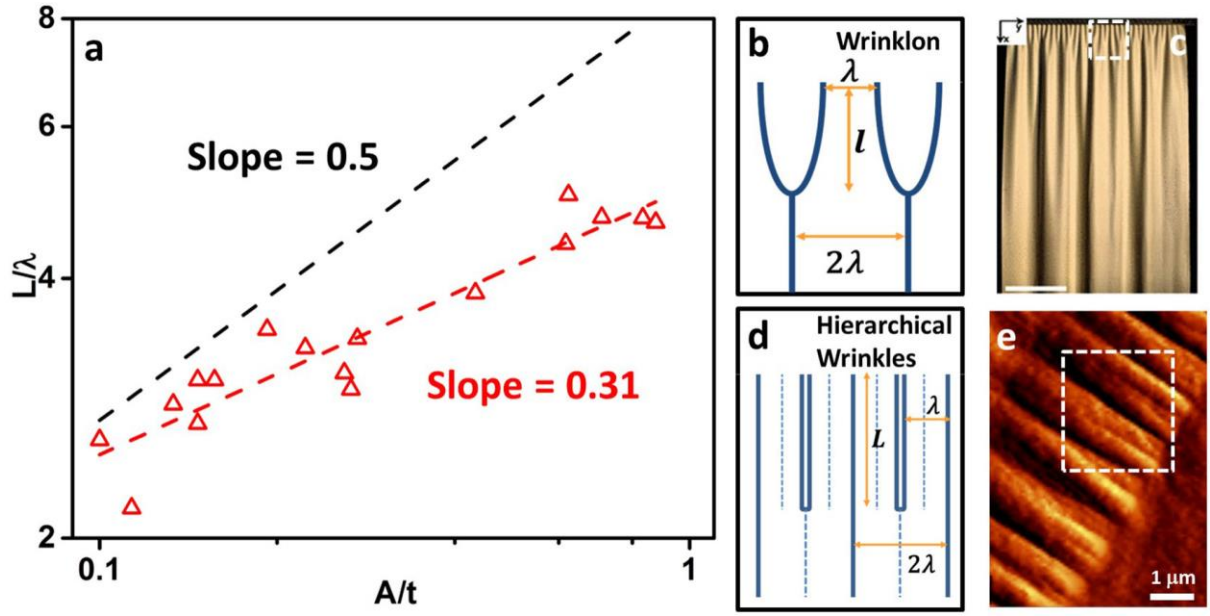

Figure 19. Evolution of normalized Length with normalized amplitude. (a) Evolution of the normalized length versus to normalized amplitude. Blackline is the power law relationship of wrinklon model (slope = 0.5), and red line is the power equation fitting (slop= 0.31) of experiment data (red triangles). (b) Schematic of the wrinklon model. l is the length of transition region. (c) Typical example of wrinklon pattern on a rubber curtain (scale bar is 25 cm), the wrinklon pattern area is highlighted in the square. Phys. Rev. Lett. 2011, 106 (22), 224301, copy right American Physical Society. (d) Schematic of hierarchical wrinkles pattern. L is the hierarchic length, and (e) AFM image of hierarchical wrinkles on the edge of thin metal film. The typical hierarchical pattern is highlighted in the square. Copyright 2016 American Chemical Society.

Therefore, the total energy in the bulk region with 300 nm cobalt thin film is:

$$U_T = U_B + U_G + U_{Th} + U_S$$

$$= L\lambda\left[Et^3\Delta(\lambda\pi)^{-2} + \rho g\lambda^2\Delta sin^2\left(\frac{2\lambda}{\pi}\right)\pi^{-2} + \frac{E}{1-\upsilon}\alpha_s^{2^2}(\Delta_T)^2 t\ +\ \frac{1}{2}Et(\frac{\partial z}{\partial x})^2 L\lambda\right]$$

$$\sim L\lambda[10^0 + 10^{-11} + 10^0 + 0] \quad (5)$$

Table IIV. The scale for all parameters for wrinkled in thin metal film.

Young's modulus of Cobalt (E_t)	2.09×10^{11} Pa
Young's modulus of Chromium (E_{Cr})	2.79×10^{11} Pa
Thickness of Cobalt (t)	300, 100, and 50 nm
Thickness of Chromium (t_{Cr})	30 nm
Poisson's Ratio of Cobalt (υ)	0.31
Bulk modulus of silicone oil (E_s)	$1 \times 10^9 \sim 1.8 \times 10^9$ Pa
Thermal expansion coefficient of silicone oil (α_s)	7.7×10^{-4} K^{-1}
Thermal expansion coefficient of cobalt (α_t)	1.2×10^{-5} K^{-1}
Thermal expansion coefficient of chromium (α_{Cr})	6.2×10^{-6} K^{-1}
Temperature Change in deposition process (ΔT)	$70 \sim 80$ °C
Density of silicone oil (ρ)	1.09×10^3 Kg/m^3
Gravitational constant (g)	9.81 m/s^2

The pseudo-strain (height variation) in x direction in bulk region is very small ($\frac{\partial z}{\partial x} \sim 0$), since the wrinkles' height in this region are invariable. Equation (5) means U_B and U_{Th} are about the same scale, however, U_G and U_S are much smaller than U_B and U_{Th} especially away from the edge, and can therefore be neglected. The surface energy decreases with increase of distance to the edge (x) and is essentially zero at the top of the meniscus. Different from previous studies on polymer thin films floating on the fluids, the gravitational energy does not play a significant role in this case. This is attributed to metal film's higher stiffness and larger bending energy than that of polymer film. Therefore, the surface energy and gravitational energy are neglected in the region away from the edge: Total energy in bulk region:

$$U_T = U_B + U_{Th} \tag{6}$$

This indicates that for region away from the edge, the liquid silicone oil substrate has similar interaction as elastic polymer substrates in previous studies on wrinkling. Therefore, we can apply the herringbone bucking model of compressed thin film,(*28*) $q^c t = (3\bar{E}_s/\bar{E}_t)^{1/3}$, where $q^c$is the critical wave number which is also the balance wave number, $\bar{E}_s$ and $\bar{E}_t$ are strain modulus of substrate and meta thin film, respectively; and strain modulus $\bar{E} = E/(1-\upsilon^2)$. Here, we approximate the bulk modulus of silicone oil to represent the Young's modulus of the substrate, $1.0 \sim 1.8 \times 10^9$Pa. The critical wavelength predicted for our bulk region is $5.98 \sim 7.27$ μm, which is consistent with 6 mm as shown in Figure 17b. The experimental wavelengths for the bulk wrinkles are close to the lower

theoretical limit. This is believed to be due to higher Young's modulus of thin chromium layer on the surface of silicone oil and the polymerization of liquid layer just below the thin film, which has much higher Young's modulus due the high film deposition temperature (100 °C).(*28, 85*) The wrinkle amplitudes away from the edge (near top of the drop) measured via AFM (about 800 nm as shown in Figure 17b) is also similar in magnitude to that from $A = \frac{\lambda}{\pi}\sqrt{\Delta}$ by substituting critical wavelengths.

Different from the bulk region, there is non-negligible interfacial surface energy applying stress to the metal thin film from the edge causing the formation of smaller wavelength wrinkles. In this regime, the total energy of the thin film is $U_T = U_B + U_G + U_{Th} + U_S$, with $(\frac{\lambda}{L})^4 \sim 10^{-2}\ to\ 10^{-3}$ as determined from the relationship shown in Figure 3b. Therefore, the total energy is given by:

$$U_T \approx U_B + U_G + U_{Th} + U_S = \sim L\lambda[10^0 + 10^{-11} + 10^0 + 10^{-1}] \quad (7)$$

and thus becomes:

$$U_T \approx U_B + U_{Th} + U_S = L\lambda^{-1}Et^3\Delta + L\lambda\frac{E}{1-\upsilon}\alpha_s^2(\Delta_T)^2t + \frac{1}{2}Et\lambda^5\Delta^2L^{-3} \quad (8)$$

Minimizing U_T with respect to L lead to:

$$L(\lambda) = (\frac{\frac{1}{6}\gamma\lambda^6\Delta^2(1-\upsilon)}{Et^3\Delta(1-\upsilon)+Et\alpha_S^2\Delta T^2\lambda^2)})^{1/4} \quad (9)$$

Scale analysis indicates the scale of $Et^3\Delta(1-\upsilon)$ is of the order of $Et\alpha_S^2\Delta T^2\lambda^2$ (about 10^{-16} and $Et\alpha_S^2\Delta T^2\lambda^2 \geq Et^3\Delta(1-\upsilon)$). This yields $L(\lambda) \sim \left(\frac{\gamma\lambda^6\Delta^2(1-\upsilon)}{6Et\alpha_S^2\Delta T^2\lambda^2}\right)^{1/4} \propto (\lambda^4\Delta^2)^{1/4} \sim \lambda\Delta^{1/2}$. Since we know $A = \frac{\lambda}{\pi}\sqrt{\Delta}$, we can deduce:

$$L(\lambda) \propto A(\lambda) \quad (\lambda \leq \lambda^c) \tag{10a}$$

$$L(\lambda) \propto A^c \quad (\lambda = \lambda^c) \tag{10b}$$

Where, λ^c is the critical wavelength $\lambda^c = \frac{2\pi}{q^c}$, which is also the maximum wavelength, and A^c is the amplitude corresponding to the λ^c, which can be calculated by $A^c = \frac{\lambda^c}{\pi}\sqrt{\Delta}$. This linear scaling law is in agreement with the results as shown in Figure 20. Therefore, wrinkling pattern in the bulk is smoothly matched to the cascade structure at the edge by this linear relationship.

The stretch from edge exists in both the wrinklon pattern and hierarchical wrinkles. The deviation of hierarchical wrinkles to the wrinklon model as shown in Figure 19 is attributed to three energies operative in the hierarchical wrinkles—bending, thermal expansion, and surface stretch ($U_T = U_B + U_{Th} + U_S$), in comparison to two energy terms —bending and stretch energy ($U_T = U_B + U_S$) in wrinklon model. Further, the substrate stiffness and thickness variation from the boundary to bulk of silicone oil also could be one of reasons that leads to this deviation. During the deposition, the silicone oil surface is crosslinked by the hot metal vapor. These thermally crosslinked silicone oil shells lead to the variation of stiffness and thickness of the substrates.(*228*)

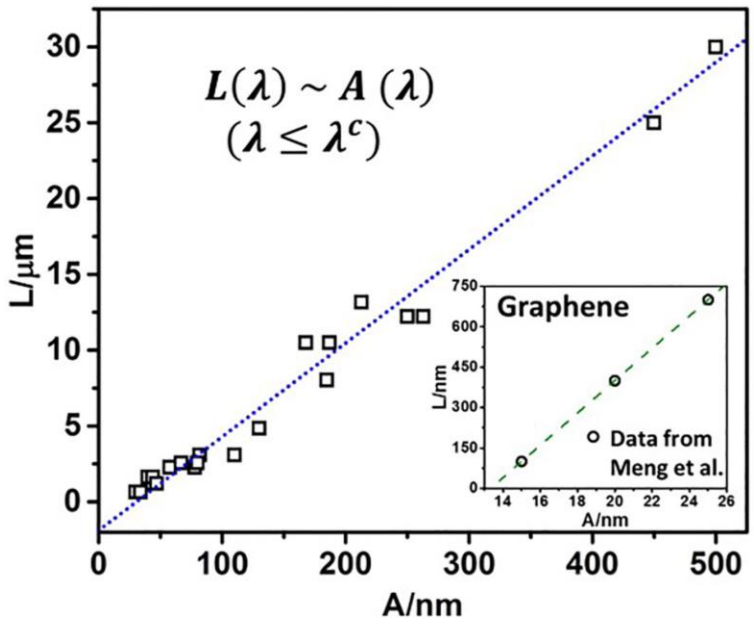

Figure 20. Evolution of hierarchic Length (L) with amplitude (A) at wavelength $\lambda \leq \lambda^c$. The relationship is fitted by a power equation with exponent equal to one. Insert images are power fitting of data from Appl. Phys. Lett. 103, 251610 (2013). Copyright 2016 American Chemical Society.

Up to 5 hierarchical wrinklon transitions occur near the edge of the silicone oil as shown in Figure 16 and Figure 17. The number of the hierarchical transitions is governed by the relative size of the wrinkle wavelength at the silicone oil boundary (shorter) and the wrinkle wavelength in the bulk region (longer). The hierarchical transition in wavelength start from the edge and increases following the hierarchical wrinkles relationship, $\lambda_{n+1} = 2\lambda_n$. These transitions stop when the wavelength reaches the bulk wavelength: $2^{n-1}\lambda_1 \geq \lambda_{Bulk}$. The number of transistors on a thinner metal film (100 nm) is 3, as shown in Figure 16d, while it is 1 or 2 for even thinner metal films (50 nm) as shown in Figure 16f. The thickness dependence is attributed to the bulk-wrinkle wavelength being a governed by the film-thickness as per the von-Karman relation. Therefore, thinner metal films lead to smaller-wavelength wrinkles in the bulk region, thus allowing fewer transitions to reach to λ_{Bulk}.

Additionally, hierarchical wrinkles on smaller silicone oil droplets and lines have fewer transition regions. This is because of the absence of bulk region, where the edge stretches to the center top surface leading to $\lambda_{max} < \lambda_{Bulk}$ as shown in Figure 16e.

We applied this scaling on wrinklons in graphene wrinkling studied by Meng et al. Here, monolayer graphene was grown on the liquid copper surface by chemical vapor deposition (CVD) and upon cooling produced one-dimensional parallel wrinkle with self-similar hierarchy. The evolution of the hierarchical length with wrinkles amplitude was near perfectly fit with the developed linear relationship as shown in the insert Figure 19. U_B, U_{Th} and U_S are linearly proportional to Young's modulus and there is no Young's modulus dependence in U_G. Therefore, a high value of Young's modulus implies relatively lower gravitational energy than other three energies. Graphene, the strongest materials with ultrahigh Young's modulus has shown similar hierarchical wrinkles on the edge after its growth on liquid metal surface. In contrast, the soft materials with lower Young's modulus have comparatively significant gravitational energy. In addition, the gravitational energy generally has an opposite effect to the bending energy leading to smaller wrinkles (amplitude and wavelength) in soft materials.

4.1.2 Adhesion Energy

The adhesion of the MoS_2 on the substrate causes the separation of thin MoS_2 flakes from the bulk MoS_2 in the mechanical exfoliation process. The curvature in wrinkled MoS_2

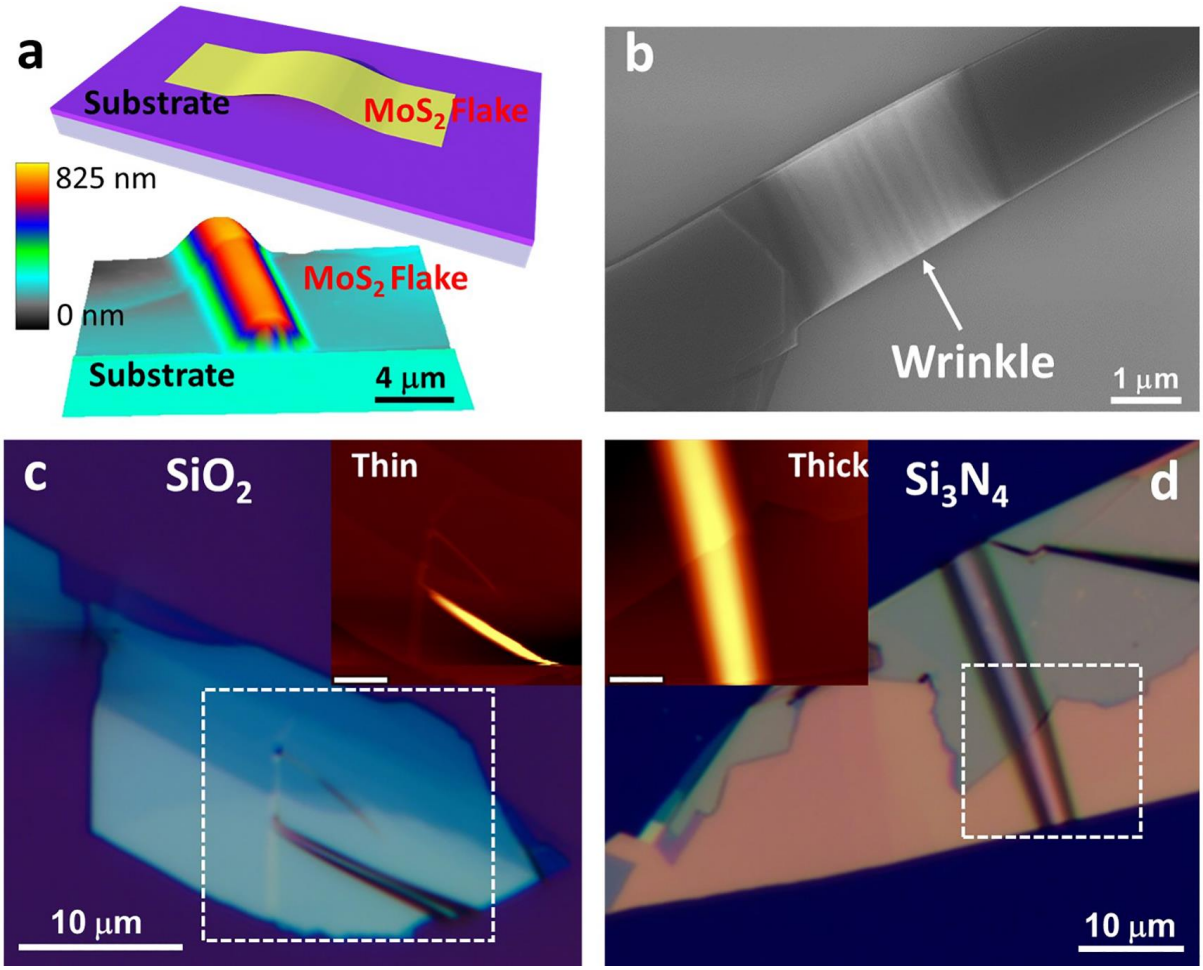

Figure 21. Typical wrinkled MoS_2 on substrates. (a) Schematic of wrinkled MoS_2 flake on substrate and AFM 3D image of a wrinkled MoS_2 flake; (b) Field emission scanning electron microscopy characterization image of a typical wrinkled MoS_2 on substrate; (c) Optical image of MoS_2 flakes on SiO_2 substrate, insert is the atomic force microscopy image of the dashed square area in (c), the thickness of wrinkled part of MoS_2 is 17 nm, and the scale bar in insert is 4 μm; (d) Optical image of MoS_2 flakes on Si_3N_4 substrate, insert is the atomic force microscopy image of the dashed square area in (d), the thickness of upper wrinkled part of MoS_2 is 80 nm and the scale bar in insert is 4 μm. Copyright 2017 American Chemical Society.

flakes leads to bending and delamination of MoS_2 on the substrate. The interplay of adhesion and bending energies results in stable partial separated, wrinkled MoS_2 on the substrates. Therefore, these wrinkles' attributes are used to calculate the adhesion

energy of MoS_2 on the substrates. Typical wrinkled MoS_2 films on substrates as observed under field emission scanning electron microscopy (FESEM) is shown in Figure 21b. Since the FESEM micrograph contrast corresponds to electron scattering due to surface curvature and electron density, the wrinkled region is brighter than the flat regions.(*229*) Wrinkled MoS_2 are formed on both SiO_2 and Si_3N_4 surfaces as shown in Figure 21c, 20d and 22. The thickness of the MoS_2 sheet is shown quantitatively in atomic force microscopy images, and they also could be qualitatively distinguished from the color in optical images in Figure 1c and 1d. The wrinkles' size (amplitude and wavelength) on relative thin MoS_2 (thickness: 17 nm, Figure 21c) is smaller than wrinkles on the thick $MosS_2$ flake (thickness: 80 nm, Figure 21d).

The height profiles of the wrinkles and the thickness of the MoS_2 flakes are shown in Figure 22. It should be noted, the horizontal axis is in micrometer scale and the vertical axis is in nanometer scale in the crossline scan of the AFM image. Therefore, wrinkles would have much smaller actual height/width ration than "displaying" height/width ratio when the horizontal and vertical axes are in the same unit scale. The wrinkles are "smooth" (small curvature) and symmetric, which is an important assumption in our model (as shown latter) since part of the bending energy will be counteracted in the sharp and asymmetric region, and weaken the adhesion of the interface.

Thermodynamically, the work of adhesion of the interface is the amount of energy required to separate thin film from the substrate and form free surfaces of thin film:(*230*)

$$W = \gamma_f + \gamma_s + \gamma_{fs} \tag{11}$$

γ_f and γ_s are the surface energies of the MoS_2 film and the substrate respectively, γ_{fs} is the adhesion energy for the film/substrate interface. Contact angle measurement is the

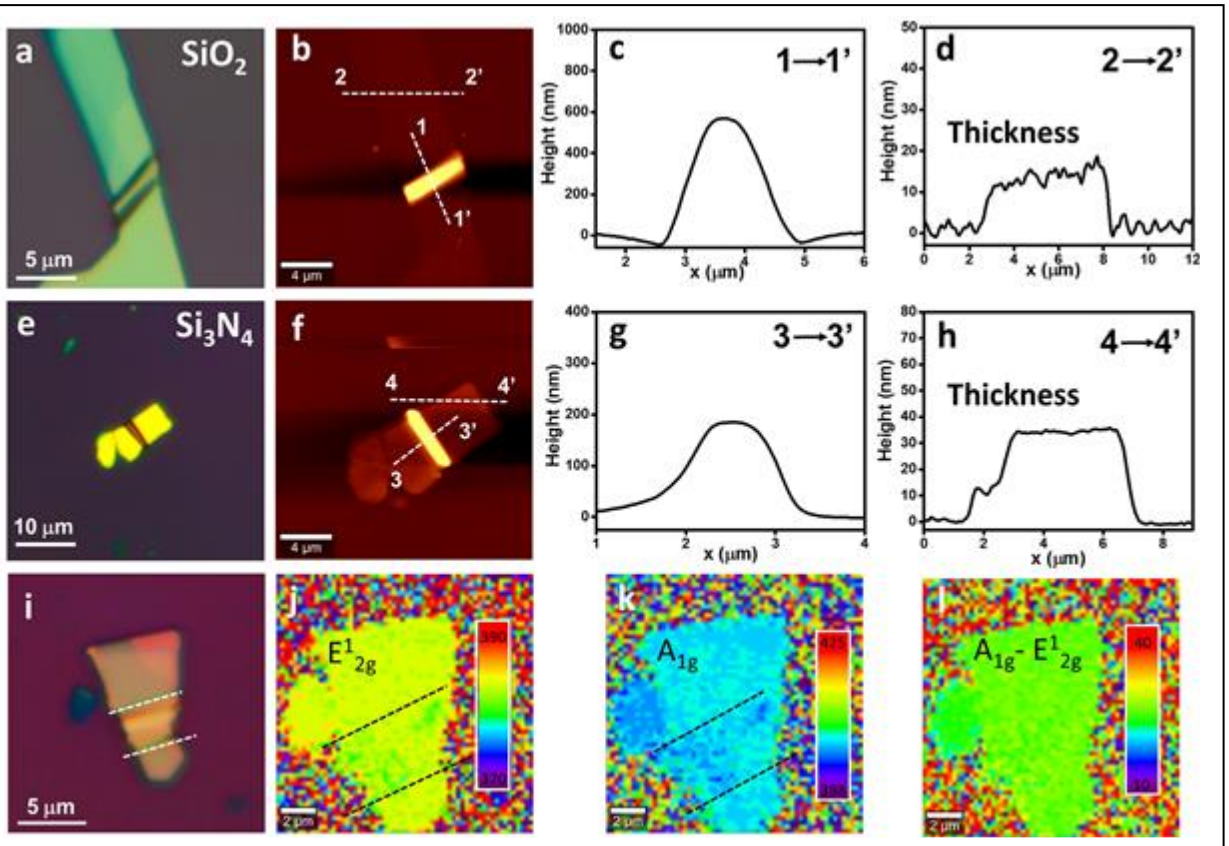

Figure 22. Characterizations of wrinkled MoS2. (a) Optical image of a MoS_2 flake on SiO_2 substrate; (b) Atomic force microscope scanning image of (a); (c)and(d) Height profiles of corresponding dash lines in (b); (e) Optical image of a MoS_2 flake on Si_3N_4 substrate; (f) Atomic force microscope scanning image of (e); (g)and(h) Height profiles of corresponding dash lines in (f). Note that the vertical scales (y-axis) are in profiles figures are nanometers, and the horizontal scales (x-axis) are in micrometers. (i) A typical optical image of wrinkled MoS_2 flakes on SiO_2. The region between white dashed lines is wrinkled region. (j) and (k) Raman position mapping of E^1_{2g} mode and A_{1g} mode, respectively. Both E^1_{2g} mode and A_{1g} mode peak in the wrinkled regions (between two dashed lines) have a red shift (low Raman position shift) comparing to that of MoS_2 in a flat region. (l) Raman position difference between E^1_{2g} mode and A_{1g} mode. No obvious color transition from flat to wrinkled MoS_2 indicates that there is not strong axial compressive strain or separation between MoS_2 layers in the wrinkled region. The units for the scale bars in (j), (k), and (l) is cm^{-1}. Copyright 2017 American Chemical Society.

most convenient and rapid method to probe the surface energy. Therefore, the Eq. (1) is often rewritten as Young's equation:

$$\gamma_{fs} = \gamma_s - \gamma_f \cos\theta \quad (12)$$

Where θ is contact angle as shown in Figure 23a, and $150^\circ \leq \theta < 180^\circ$ from the experiment data in our case. The surface energies of SiO_2 (γ_{SiO_2} = 0.115-0.200 Jm^{-2})(*96*) and MoS_2(γ_{MoS_2} = 0.0465 Jm^{-2})(*231*) give that the MoS_2/SiO_2 interfacial energy γ_{MoS_2/SiO_2} = 0.155-0.246 J m^{-2} from Equation (12). However, there is no reliable data for the surface energy of Si_3N_4 ($\gamma_{Si_3N_4}$) at room temperature, which leads to an unavailable estimation for γ_{MoS_2/Si_3N_4} in Young's equation.

The formation of wrinkles is a consequence of the interplay between bending energy of the MoS_2 flakes and interface adhesion energy,(*105*) as shown in Figure 23. The adhesion energy of the MoS_2 flakes can be measured accurately from the thickness of the flakes and the size of the wrinkles. We assume that the van der Waals forces between MoS_2 layers are strong and sufficiently enough to adhere each other, so no significant sliding or delamination occurs in MoS_2 layers as shown in Figure 22j to 22k and explained later. (*96*)

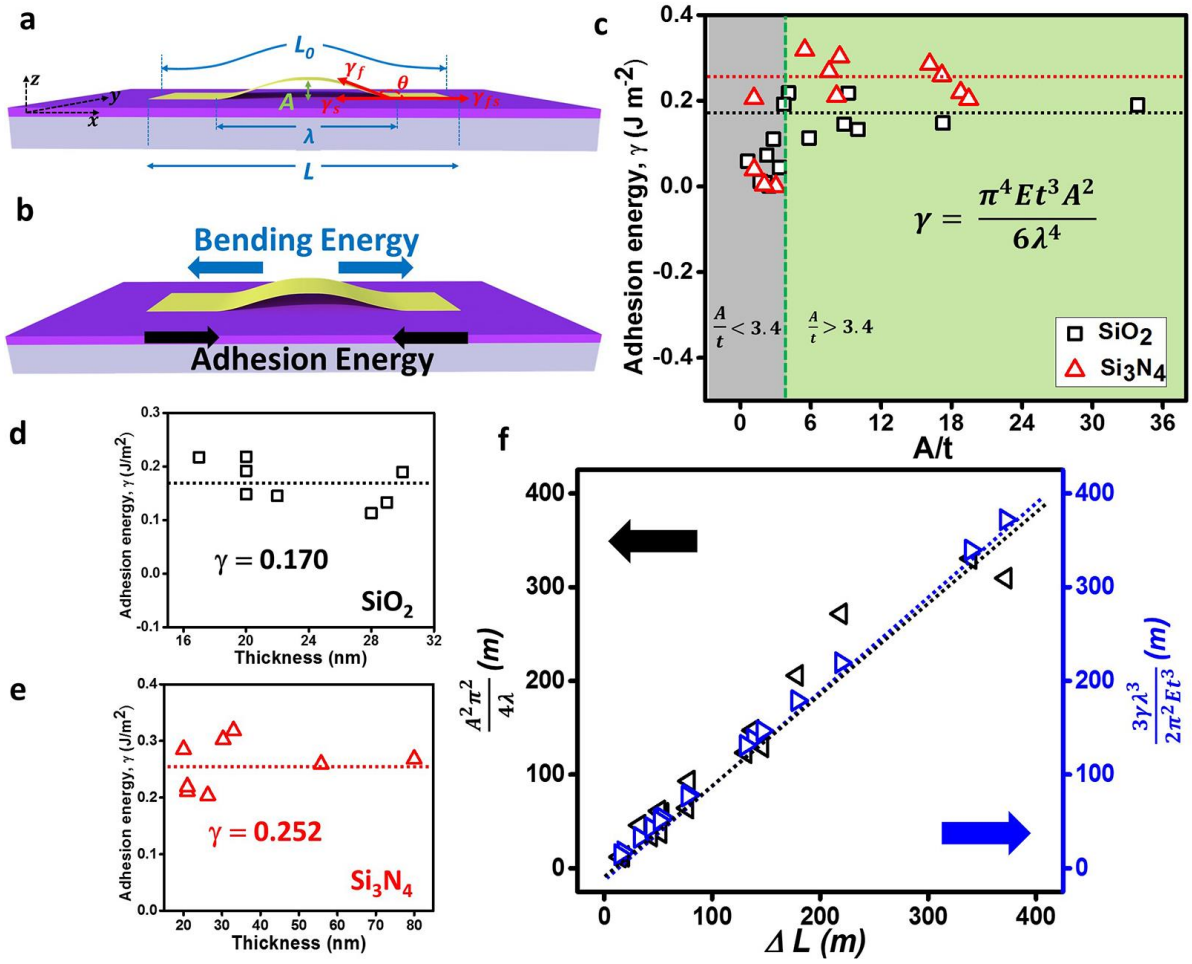

Figure 23. Wrinkled MoS2 on substrate and adhesion energy calculation and analysis.(a) Schematic the wrinkled MoS_2, L_0 is the original length of the MoS_2, L is the project length of wrinkled MoS_2 on substrate, A and λ stand for the amplitude and wavelength of the wrinkle respectively; and red arrows stand for the surface energies at contact region, γ_f and γ_s are the surface energies of the MoS_2 film and the substrate respectively, γ_{fs} is the energy for the film/substrate interface, and θ is contact angle; (b) Schematic of energy distribution in wrinkled MoS_2, sheet energy is not shown here; (c) Adhesion energy calculation of MoS_2 on SiO_2 (black squares) and Si_3N_4 (red triangles) surface versus normalized amplitude $\frac{A}{t}$. The green dashed line is the $\frac{A}{t}$=3.4. Grey area has $\frac{A}{t}$ < 3.4 and the green area has $\frac{A}{t}$ > 3.4. The black and red dash lines are the average of respective data for SiO_2 and Si_3N_4 in the green area; (d) and (e) The thickness dependence of the adhesion energies of MoS_2 on SiO_2 and Si_3N_4, the value of the black dash is γ = 0.170 and value of the read dash is γ = 0.252; (f) Length scale parameters $\frac{3\gamma\lambda^3}{2\pi^2 Et^3}$ (blue) and $\frac{A^2\pi^2}{4\lambda}$ (black) versus ΔL. Copyright 2017 American Chemical Society.

The total energy (U_T) of the wrinkled MoS_2 system can be represented as the following equation: $U_T = U_B + U_A + U_S$, where, U_B is the bending energy for wrinkles in MoS_2 sheet, U_A is the adhesion energy of MoS_2 on the substrates, and U_S is the interlayer sheet energy in the MoS_2 wrinkles. Assume the wavelength of a wrinkles is constant in $the\ y$ direction as shown in Figure 23a, therefore, the wrinkles energy analysis can be simplified to a two-dimensional model in xz plane. Units of all energies are J m^{-1}. The corresponding out-of-plane displacement in the wrinkled MoS_2 sheet can be simplified to be a function: $z = \frac{A}{2}[1 + \cos(\frac{2\pi x}{\lambda})]$,[23,24] which satisfies the boundary condition of zero slope at the two ends ($x = \pm\frac{1}{2}\lambda$), where A is the amplitude and λ is the wavelength of the wrinkle, respectively. The bending energy can be written as $U_B = \frac{\pi^4 E t^3 A^2}{12\lambda^3}$,[23] where E is Young's modulus of the MoS_2 sheet and t is the thickness of the sheet. Adhesion energy $U_A = -\gamma\ (L - \lambda)$, where γ is the adhesion energy between MoS_2 and substrate per unit area (J m^{-2}) and L is the projected length of the wrinkled MoS_2 on substrates (xy plane in $the\ x$ direction), and L_0 is the original length of winkled MoS_2 sheet in x direction. Sheet energy $U_S = \frac{1}{2}\ EtL(\frac{\pi^2 A^2}{4L\lambda} - |\Delta|^2)$ with $\Delta = (L - L_0)/L$ is the plane strain.(*105, 232*) However, the sheet energy in our case is negligible as shown in Raman strain study in Figure 22. In the wrinkled region, the two most prominent Raman peaks, E^1_{2g} mode (near 384 cm^{-1}) and A_{1g} mode (near 405 cm^{-1}), are red-shifted (the vibrations soften) as shown in Figure 22j to 22k. These red shifts indicate the strain in the plain of MoS_2 flake and the existence of wrinkles. Further, there is no obvious change of the difference between E^1_{2g} mode and A_{1g} mode in the wrinkled region comparing to that of the flat part as shown in Figure 22l. This means no separation between MoS_2 layers in the wrinkled region. Therefore, the

sheet energy U_S can be ignored in the total energy. The linear total energy can be rewritten as:

$$U_T = U_B + U_A = \frac{\pi^4 E t^3 A^2}{12\lambda^3} - \gamma\,(L - \lambda) \tag{13}$$

Minimizing U_T with respect to A and λ leads to $A = \frac{2\lambda}{\pi}\sqrt{(|\Delta| - \frac{\pi^2 t^2}{3\lambda^2})\frac{L}{\lambda}}$ and $\frac{\pi^2 t^3}{3\lambda^3}\left(\frac{\pi^2 t^2}{3\lambda^2} - |\Delta|\right) + \frac{\gamma}{2EL} = 0$. Assuming, $|\Delta| \gg \frac{\pi^2 t^2}{3\lambda^2}$ and $|\Delta| - \frac{\pi^2 t^2}{3\lambda^2} \sim |\Delta|$. This yields:

$$\frac{\lambda}{t} = \sqrt[3]{\frac{2\pi^2 E(L_0 - L)}{3\gamma}} \tag{14}$$

$$A = \frac{2\lambda}{\pi}\sqrt{\frac{L_0 - L}{\lambda}} \tag{15}$$

Combine equation (14) and (15):

$$\frac{A}{\lambda} = \frac{2}{\pi}\sqrt{\frac{\frac{2}{3}\sqrt{L_0 - L}}{t}\sqrt[3]{\frac{3\gamma}{2\pi^2 E}}} \tag{16}$$

Therefore,

$$\gamma = \frac{\pi^4 E t^3 A^2}{6\lambda^4} \tag{17}$$

The calculation results of adhesion energies for MoS_2 on SiO_2 and Si_3N_4 are shown in Figure 23c. However, it should be noted, Equation (14) to Equation (17) are also based on the condition ($|\Delta| \gg \frac{\pi^2 t^2}{3\lambda^2}$). The axial compressive strain $\Delta = \frac{A^2\pi^2}{4\lambda L}$ is given by rewriting Equation (15) and $\frac{A^2\pi^2}{4\lambda L} \gg \frac{\pi^2 t^2}{3\lambda^2}$. From the experiment data, we know that L is in the scale of 10 μm and λ is in the scale of 1 μm, this leads to $\frac{A^2}{t^2} \gg \frac{L}{\lambda} \approx 10$ and the value of

normalized amplitude $\frac{A}{t}$ should be great than 3.4 for the validity of $|\Delta| \gg \frac{\pi^2 t^2}{3\lambda^2}$. Therefore, the data with $\frac{A}{t} \geq 3.4$ are favorite for the calculation of the adhesion energy in our model. The adhesion energies for a MoS_2 nanoscale thin film on SiO_2 and Si_3N_4 are 0.170 ± 0.033 J m^{-2} and 0.252 ± 0.041 J m^{-2}, respectively. This adhesion energy for MoS_2/SiO_2 interface closely agrees with the value we estimated thought Young's equation (Equation (12)).

The calculation of adhesion energies based on selected data versus thickness of the thin film are shown in Figure 23d (SiO_2) and 23e (Si_3N_4). The results show a thickness-independence in a broad range (thickness larger than 15 nm) for both substrates. This validity is guaranteed by the normalized amplitude condition ($\frac{A}{t} \geq 3.4$). Rewriting Equation (14) to a length scale parameter $= \frac{3\gamma\lambda^3}{2\pi^2 E t^3}$, and Equation (15) to the same length scale parameter $\Delta L = \frac{A^2\pi^2}{4\lambda}$, therefore, we have:

$$\frac{3\gamma\lambda^3}{2\pi^2 E t^3} = \frac{A^2\pi^2}{4\lambda} \tag{18}$$

Equation (18) also can be used verify the value of the adhesion energies, the comparison of these two parameters' in the two sides of the Equation (8) as shown in Figure 23f. The overlapping of linear fittings for experiments ($\frac{3\gamma\lambda^3}{2\pi^2 E t^3}$) and theory ($\frac{A^2\pi^2}{4\lambda}$) shows that our data is well fit our model.

Additionally, transformations of Equation (14) and Equation (15) also give the plane strain as:

$$\Delta = \frac{A^2\pi^2}{4\lambda L} = \frac{3\gamma\lambda^3}{2\pi^2 E t^3 L} \quad (19)$$

This means, for certain thickness of thin film on substrates (known t and γ) formed wrinkles, two-dimensional size characteristics—wavelength of wrinkles (λ) and length of thin film (L), but not the third dimensional measurement—amplitude (A), are need for the plane strain (Δ) measurement. Since the amplitude measurement is slow, expensive and destruct process as shown later, Equation (19) will provide a fast, low-cost and damage-free plane strain measurement approach for thin 2D nanomaterials.

Mechanisms and Analysis

The adhesion is affected by the film thickness, microstructure, chemistry and test temperature.(*230*)[21] For the adhesion study on graphene, monolayer graphene showed larger adhesion than the two to five layer graphene, this was due to that graphene is extreme flexible, which allowed it to conform to the substrate surface topography, leading to a topography interaction with the substrate.(*96*)[11] The result shown in Figure 23d and 23e does not mean the adhesion is thickness-independent for any thickness of MoS_2 film. Ultrathin (monolayers) MoS_2 may have higher adhesions on substrates than multilayers MoS_2 due to higher flexibility.(*96*)[11] However, this effect in MoS_2 is expected to be reduced because of the three atom thick network in monolayer MoS_2 instead of one atomic layer in monolayer graphene. The liquid–like interaction is expected to be absent for thickness larger than 15 nm (20 layers). Thinner films fit better in our model as shown in our calculation, the value of $\frac{\pi^2 t^2}{3\lambda^2}$ decreases and the value of normalized amplitude $\frac{A}{t}$

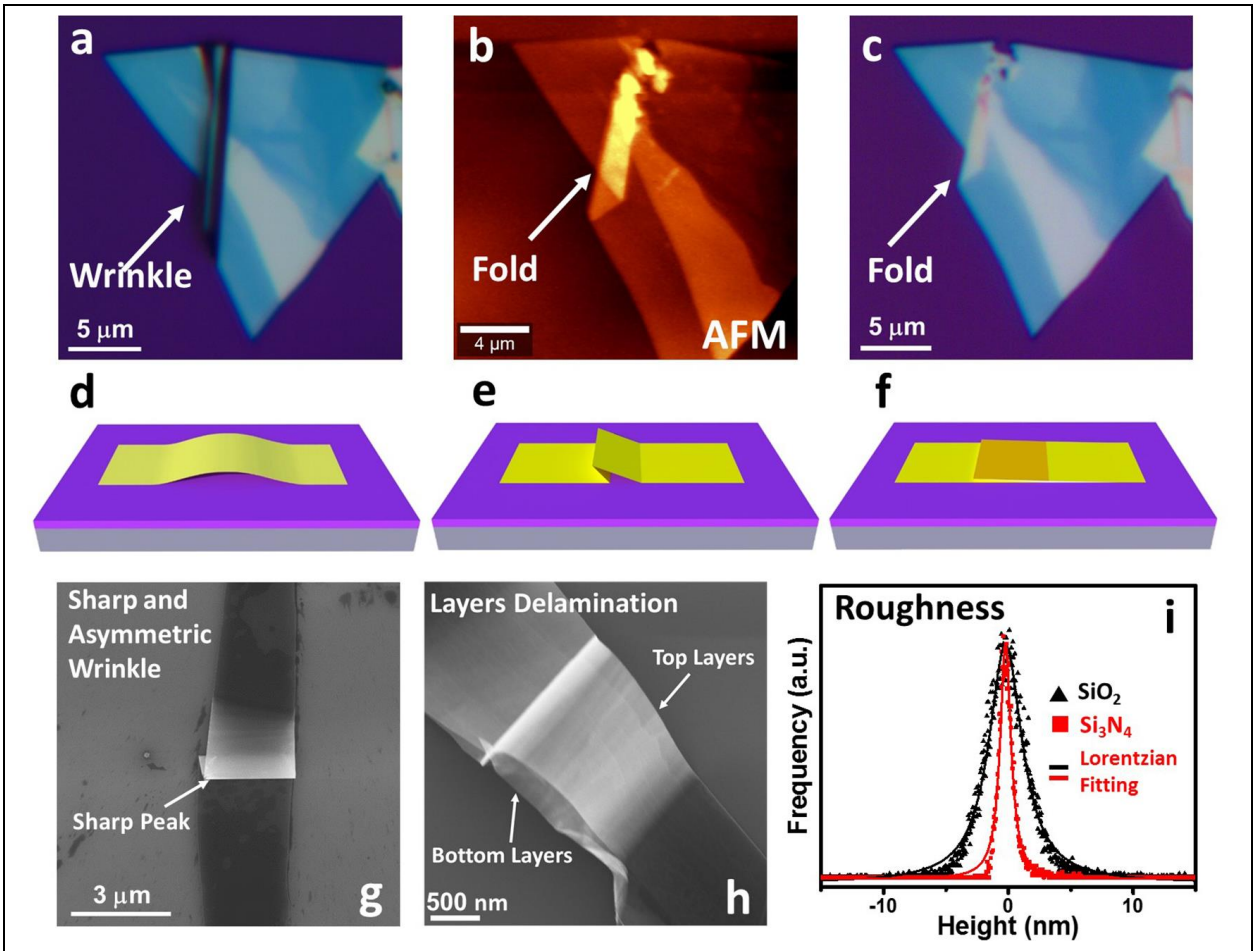

Figure 24. MoS2 wrinkling on SiO2 and Si3N4 surface mechanism analysis. (a) Optical image of the thin MoS_2 flakes on SiO_2 surface right after mechanical exfoliation. The dark bar region is the wrinkle; (b) Atomic force microscopy scanning of the same area in (a). The wrinkle collapsed and formed fold in the scanning process. The thickness of the flake in wrinkled region is 10 nm; (c) Optical image of the thin MoS_2 flakes on SiO_2 surface after scanning, the wrinkles collapsed and disappeared and fold was formed; (d), (e), and (f) Schematics of symmetrical, asymmetrical and folder wrinkles on substrates; (g) Scanning electron microscope image of a sharp and asymmetry wrinkled MoS_2; (h) Scanning electron microscope image of a layers delamination in MoS_2, the top layers is thin and wrinkled and delaminated form the bottom layers; (i) Surface roughness analysis of SiO_2 and $Si3N_4$ substrates. Solid lines are the Lorentzian fittings for the roughness data. Copyright 2017 American Chemical Society.

increases for the thinner MoS_2 film. However, thin layers of MoS_2 (below 10 nm) is not applicable for the adhesion calculation due to reduced bending rigidity of thin layers of

MoS_2 sheet. In our case, the thin film wrinkles will collapse and form folds, especially in the AFM scanning process, which are unstable wrinkles with one side collapsed on the other side of wrinkles. This formation of folds leads to smaller adhesion energy in the calculation since the collapsing leads to smaller wrinkle amplitude but larger wavelength, as shown in Figure 24a to c. In this case, the symmetrical wrinkles are expected to experience external forces (AFM measurement), then transform to asymmetrical and sharp wrinkles, and collapse into folded wrinkles in the end, as shown in Figure 24(d) to (f).

Further, small wrinkles, even on relative thick flakes, are unreliable in the calculation of the adhesion, since the values of normalized amplitude $\frac{A}{t}$ would be smaller than 3.4. Additionally, small wrinkles do not fit our model and can form due to several reasons. One is that only a partial flake layers may be involved in the formation of wrinkles: only a few top layers are wrinkled and these wrinkles are supported on the bottom layers of MoS_2 instead of the substrate, as shown in Figure 24h. The top layers are very thin and partially delaminated from the bottom layers, which is visible through the top layers (Figure 24h). The wrinkle is the consequence of bending of top layers and adhesion between MoS_2 layers, which can be applied to study the interlayer adhesion. Another reason could be contamination in the interface between substrates and flakes results in the deformation of the flakes. Further, the line defects and deformations in the bulk MoS_2 also can induce wrinkles-like topography of the surface of the flakes. Since part of the bending energy is partially counteracted in the sharp and asymmetric region, the adhesions are weak on the interface, as shown in Figure 24g. This would result in false high adhesion in the

calculation with Equation (17). Further, these wrinkles also cannot be eliminated through the condition $\frac{A}{t} \geq 3.4$, since they have distorted high amplitudes comparing to the smooth wrinkles. This type of wrinkles can be excluded from AFM height profiles, as shown latter. All these situations were avoided in the data collection for the adhesion calculation.

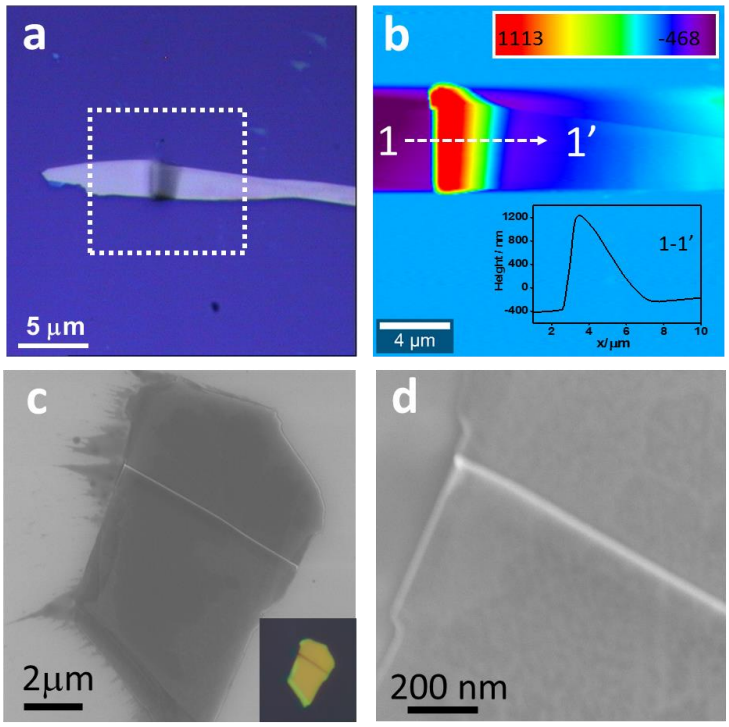

Figure 25. Asymmetric Wrinkled MoS_2 on SiO_2. (a) Typical optical image of a wrinkled MoS_2 (b) Atomic force microscopy characterization image of the same wrinkled in (a), insert is the height profile along the dashed line (1-1'). (c) and (d) SEM image of an asymmetric wrinkle.

These values of adhesion of MoS_2 on SiO_2 are smaller than previous study(*96*) for the graphene sheet on SiO_2, which can attribute to the MoS_2 flakes being not that flexible so as to conform to the topography of the substrate, especially the relatively "thick" MoS_2 flakes are used in our study. On the other hand, the MoS_2 flakes show larger adhesion on the Si_3N_4 surface than the SiO_2 surface. This may be caused by the roughness

difference between these two surfaces. The roughness of the SiO_2 and Si_3N_4 surface can be detected in the AFM, as shown in Figure 24i. Both SiO_2 and Si_3N_4 are very smooth. However, the Si_3N_4 surface is smoother than the surface of the SiO_2. Theoretical studies suggested that adhesion energy shows a jump increase to a decrease of the substrate's roughness (idealized sinusoidal profiles).(*232*) Therefore, Si_3N_4 makes closer and more intimate contact with MoS_2 than that of SiO_2 and results in larger adhesion energy.

In conclusion, a wrinkled MoS_2 can be used to determine the adhesion energy of MoS_2 on rigid and flat substrates (SiO_2 and Si_3N_4). The adhesion energies of 0.170 ± 0.033 J m^{-2} for MoS_2 on SiO_2 and 0.252 ± 0.041 J m^{-2} for MoS_2 on Si_3N_4 were obtained, respectively. The different values on these two substrates are attributed to the roughness of the surfaces. This method is suitable for wrinkles with ($\frac{A}{t} \geq 3.4$). Wrinkles in ultra-thin film ($< 10\ nm$) were not stable in the AFM measurement. We also propose a method to measure the strain in three-dimensional wrinkle without measuring the amplitude of wrinkles. For known thickness of a thin film on substrates (known t and γ), two-dimensional size characteristics—wavelength of wrinkles (λ) and length of the thin film (L), but not the third-dimensional measurement—amplitude (A), are needed for the strain measurement. Therefore, the plane strain measurement for wrinkles on ultra-thin film can be attained without damaging the wrinkles. The method may be extended to study the surface interaction, 2DNs properties modulations, and thin film device fabrication.

4.2 Wrinkled in graphene on bacteria

Integrating the quantum mechanical phenomena of structurally-intact nanomaterials with the functionalities of interfaced biological components can produce advanced

bionanotechnologies: cell actuated sensors(*233*), cell-driven FETs (*234*), cell-excretion based FETs(*46, 235*), and cell electrochemical transponders(*236*). Understanding the interface between soft biological cells and quasi-fluidic 2D nanomaterials (2DNs) can evolve important applications in sensing(*46*), bio-actuated devices(*236, 237*), and bio-gated FETs(*234, 238*). While most of the current effort has been focused on intact graphene, its structural modification can alter its properties (*48, 111-113*) and open new avenues for bioelectronics. Producing nanoscale 2D wrinkles in confined and position-controlled micro-scale region requires a substrate, which (a) has strong adhesion with wrinkling film and a high Young's modulus, (b) is 'localized' in micro-scale region, (c) can induce large strain *via* surface-area change, (d) has structural integrity, and (e) can be controllably positioned on devices with precision. Here, we demonstrate that a microorganism may possess all these attributes and can induce compression on an overlaying graphene sheet to produce nanoscale-wavelength wrinkles in a confined region.

Bacillus subtilis, which provides a unique combination of properties for this task: (i) nominally rod-shaped, (ii) 1 X 5 μm^2 in size, (iii) high-adhesion, amphiphilic surface-architecture made of peptidoglycan membrane: crosslinked chains of hydrophobic fatty acids and hydrophilic groups (teichoic acid, sugar, etc.), (iv) high volatile intracellular content (~75-80% water), (v) water in cytoplasm is exchanged with the surrounding *via* aquaporins (porins for water molecules) on the cell wall, and (vi) squeezable: cell contracts with water reduction. Although, water-swelling polymers or hydrogels that can

also retain water, however, their structures are challenging to be robust and confined into 1 X 5 μm^2 area.

4.2.1 FESEM characterization

The wrinkles formed are highly selective, longitudinal and confined on graphene sheet atop bacterial cells as observed under FESEM (Figure 26). This is attributed to bacterium's radial shrinkage being energetically more favorable than axial shrinkage.(*239*) Further, *Bacillus subtilis* is strepto-Bacillus bacteria, which form long, connected chains; thus, the wrinkles can cross from one bacterium to the next to produce longer. Figure 23a shows a magnified FESEM micrograph of wrinkled graphene on bacteria and the inset depicts contrast scan for the dashed line. Since the FESEM micrograph contrast must correspond to the wrinkles on the graphene,(*229*) the contrast scan provides the number of the wrinkles (n) on each transverse bacteria: n = 20 with an average wavelength (λ, the distance between two wrinkles) of 32.4 nm. Angular spectrum analysis (SPIP™ software package) was conducted to investigate the anisotropy of the wrinkles on graphene (Figure 9 (c), and (d))(*240*). The texture direction (TD) – the angle of the dominating texture in the image (angular range = 0 to 180; X-direction = 0^0) – for Figure 26 (cropped along the wrinkled area with longitudinal bacterium as horizontal) is 89.7^0 (close to 90^0) implying longitudinal wrinkles. The texture aspect ratio (TAR) – the ratio of the fastest to slowest decay to correlation at 37% (the equivalent of 1/e) of the autocorrelation function – is a measure of texture uniformity. Strongly anisotropic surface has TAR (value between 0 and 1) < 0.3, while an isotropic surface texture will have TAR ~ 1. A TAR value of 0.125 (Figure 9 (c)) for the wrinkled graphene indicates strong spatial

anisotropy. Further, we observed the diameter of the bacterium D_B (~1 μm) shrinks to D_W (~0.6 μm), which is the width of the wrinkled region. The wavelength of wrinkles is independent of the diameter of bacteria as showing in FESEM studies.

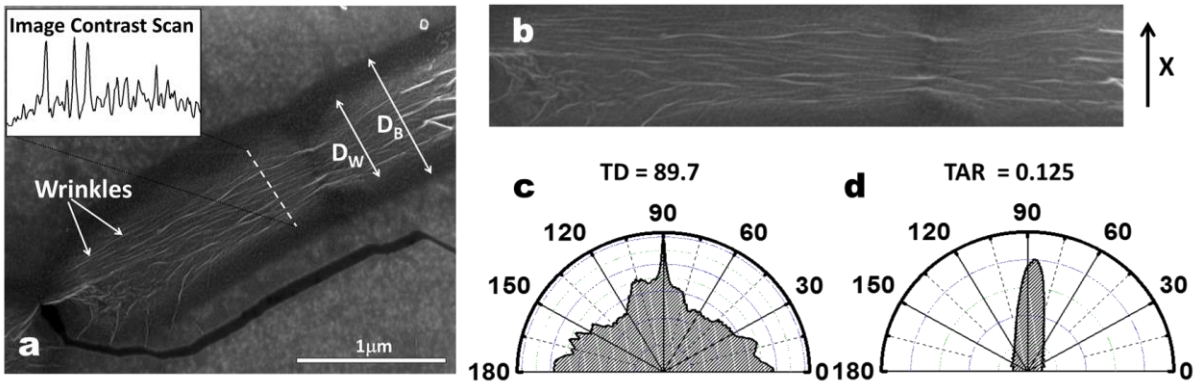

Figure 26. FESEM image of wrinkles on graphene and angular spectrum investigation. (a) FESEM micrograph of one and a half bacterium. The inserted figure is the brightness contrast scan. D_B is the diameter of the bacteria and D_W is the diameter of the wrinkle area atop the bacteria surface, (b) The texture direction Study of rectangular area in (a), and (c) The texture aspect ratio study of rectangular area in (a). Copyright 2016 American Chemical Society.

4.2.2 AFM characterization

The AFM scans shown in Figure 27 are consistent with FESEM image analysis in Figure 26. The height of the wrinkles varied from 7 to 10 nm. Unlike FESEM operation under high vacuum, AFM allows inspection of graphene before and after vacuum/heat exposure under ambient conditions. In contrast to a continuous and smooth surface of graphene on bacteria before the vacuum/heat treatment (Figure 27a), the surface becomes wrinkled after vacuum/heat treatment (Figure 27b)and stays wrinkled at atmospheric pressure for > 48 h, as shown in Figure 27c. Further, the average height of the bacterial cell reduces

from 0.278 μm to 0.186 μm, which is attributed to a reduction in aqueous content. Cracks near the bacteria after vacuum/heat treatment are also observed in AFM images.

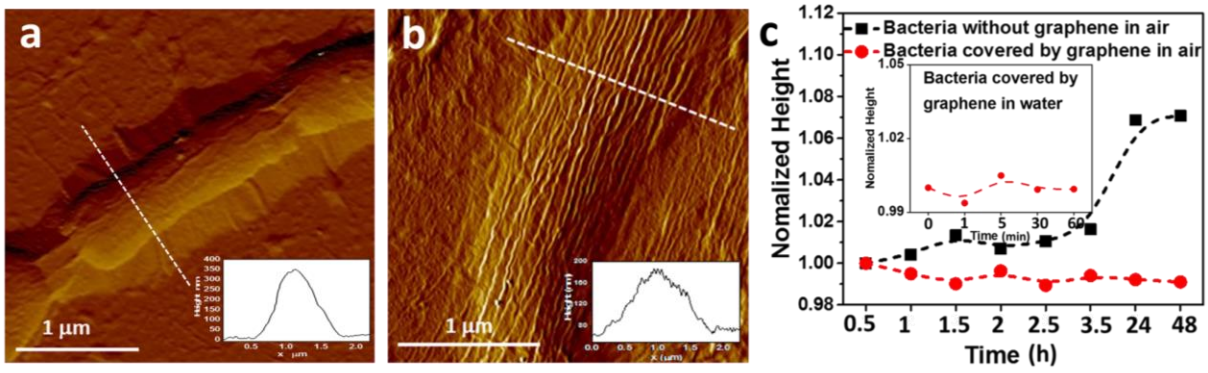

Figure 27. AFM and simulation studies of graphene on bacteria before and after vacuum/heat treatment. (a) Image of grapheme on the bacteria before vacuum and temperature; (b) Image of bacteria area under graphene after vacuum and temperature treatment. Insert figures are height scanning of white dash line in figure (a) and (b), respectively. (c) Time study of height bacteria in air after vacuum. Bacteria without graphene covered (Black dash line), bacteria with graphene covered; (d) Bacteria with graphene covered in water after vacuum. Copyright 2016 American Chemical Society.

4.2.3 Raman spectroscopy characterization

The relative strain on graphene at different stages of the process was investigated *via* Raman shift measurements of the G and 2D peaks and their shapes.(*241*) The elongation and weakening of the C-C bonds lead to a Raman-redshift, lowering the vibrational frequency,(*241*) and the full width at half maximum (FWHM) increases upon application of tensile stress.(*242*) The Raman mapping of graphene on bacteria surface before and after the vacuum is displayed in Figure 28 (a) and (b), respectively. Both the G and 2D peak positions of graphene on bacterial surface (Figure 28 (c) and (d)) are redshifted compared to graphene on flat substrate (darker on bacterium than on SiO_2), indicating

the existence of tensile strain induced by bacterial curvature as discussed earlier (FESEM, AFM and CGMD simulation results). The strain also increases the FWHM of the G peak from 15 to 33 cm^{-1} (more than two-fold increase). After vacuum/heat annealing and wrinkle formation, graphene on bacteria exhibits a blueshift in the G-peak with respect to graphene on SiO_2 (brighter on bacterium than on SiO_2). This Raman blueshift can be attributed to the release of tensile strain or addition of compressive strain due to the formation of wrinkles. Note that after vacuum/heat annealing, the entire graphene region exhibits blueshift (~15 cm^{-1} increases in G and 2D peak positions) attributed to desorption of O_2 and other adsorbents(*243*). Note also that the D-peak of graphene coincides with the Raman peaks for bacteria. The Raman 2D frequency can be related to the strain by:

$$\frac{\Delta\omega}{\omega_0} = \gamma.(\varepsilon_a + \varepsilon_p) \tag{20}$$

Where γ =1.24 is the Güneisen parameter(*244*) and ε_a is the axial strain, ε_p is the relative strain in the perpendicular direction from the Poisson's ratio of graphene ε_p = -0.186 ε_a, ω_0 is the Raman band frequency and $\Delta\omega$ the shift. Therefore;

$$\varepsilon_a = \Delta\omega/[-\omega_o.\gamma.(1-0.186)] \tag{21}$$

Before annealing, graphene exhibits a strong 2D-peak feature centered around 2675 cm^{-1}, G-peak at 1578 cm^{-1}; while graphene on bacterium exhibits redshifted 2D peak (2665 cm^{-1}) and G peak (1566 cm^{-1}). The 10 cm^{-1} redshift implies a strain, ε_a of 0.37% for graphene on the bacterium. This is close to the CGMD calculations, which measures the in-plane strain along the cross-section profile of graphene/bacterium contact as 0.42% ± 0.01%.

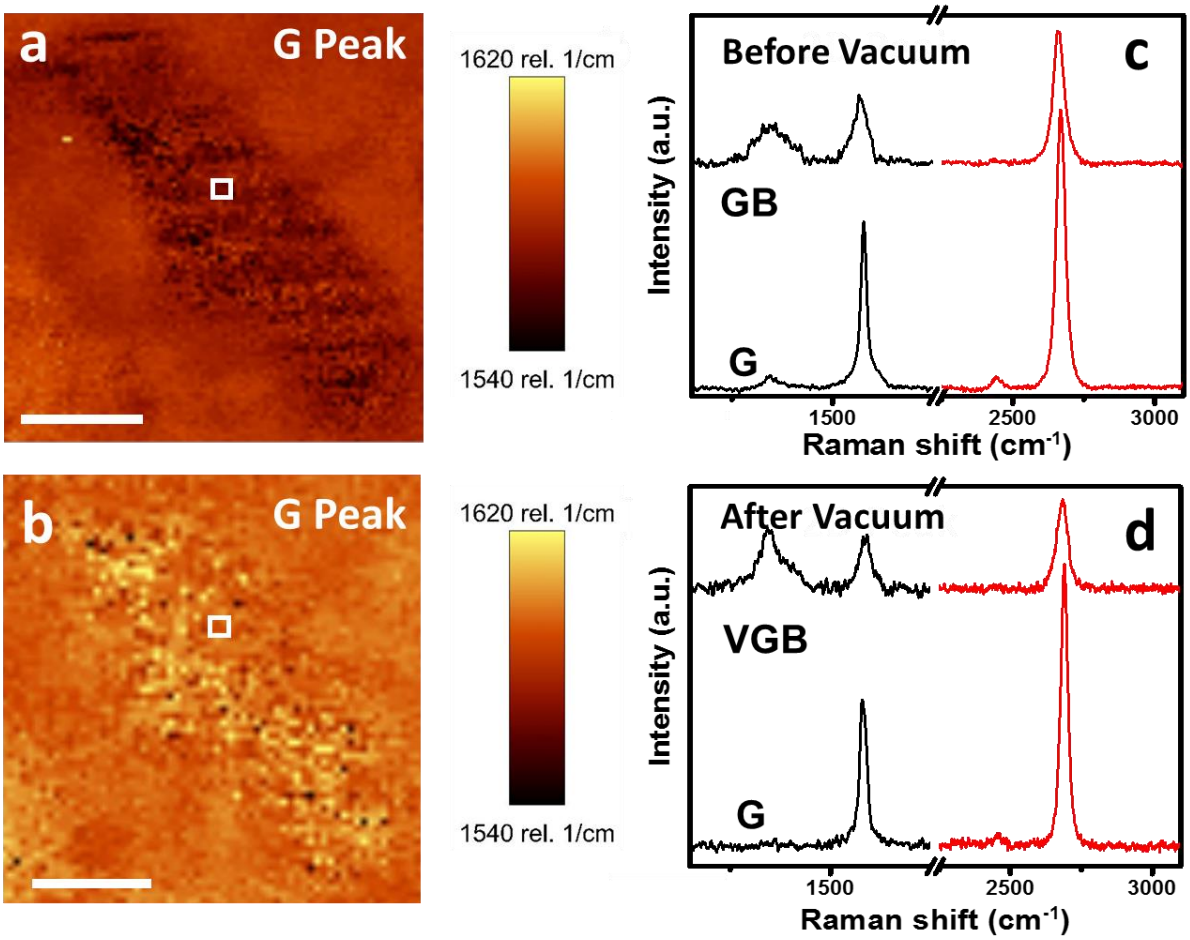

Figure 28. Raman spatial mapping of G peaks on same position before and after vacuum treatment. (a) G peak position mapping of graphene-on-bacteria surface before vacuum; (b) G peak position mapping of graphene-on-bacteria surface after vacuum; (c) Raman spectrum of typical position of graphene on SiO_2/Si substrate (G) and on position of white square showing in (a) before vacuum (GB); (d) Raman spectrum of typical position of graphene on SiO_2/Si substrate (G) and on position of white square showing in (b) after vacuum (VGB). Scale bars in (a) and (b) is 1 μm. Copyright 2016 American Chemical Society.

4.2.4 Properties and mechanism investigation

4.2.4.1 Anisotropic carrier mobility and conductivity

To study the electrical properties of the wrinkled graphene, we electrophoretically positioned the bacterial cells between two Au electrodes. Briefly, a droplet of diluted

bacterial suspension (in deionized water) is carefully placed in the region between pointed Au electrodes (~ 5-10 μm apart) while applying an AC field (Electric field = 1 V/μm and frequency = 5 MHz) for 5 min. The bacterial cells experience a force towards positive field gradient (higher field intensity) and thus are directed towards the electrode junction, where they immobilize, bridging the electrode-gap. This is followed by transfer and placement of monolayer graphene atop the bacterial cells.

In order to study the effect of graphenic wrinkles' orientation on the carrier transport, we fabricated a 'plus-shaped' wrinkled-graphene-on-bacterium device (van der Pauw structure) with bacteria placed parallel and perpendicular to a pair of respective electrodes (Figure 29b and Figure 29c). It is important to note that the devices did not produce cracks, presumably due to pores formed during the post UV-lithography O_2 plasma etching step. The FESEM and AFM micrographs confirm that the graphene-wrinkles are oriented in the longitudinal direction (along with the bacteria). Current-voltage (*I-V*) studies under vacuum (in order to ensure graphene wrinkles) exhibited lower conductivity in the transverse direction (T-direction) versus the longitudinal direction (L-direction) (at all the gate voltages). Out of the 10 devices tested, the doping levels were varied and the Dirac point (with p-doping) was observed for only two devices (one shown in Figure 29d). At respective Dirac points (zero net doping, n=p), the conductivity in the L-direction was higher than that in the T-direction, representing an anisotropic electrical transport. Further, the Dirac point for L-transport was ~8 V higher than that for T-transport or in other words, L-transport had more carriers ($<1.46 \times 10^4$ holes/μm^2 (as carrier concentration, $n = 2C_{SiO2}DV/e$)). This represents the difference in the participating doped

charges from bacteria along the two conduction pathways: The least resistive path in the L-direction has more bacteria (thus more doping) than in the T-direction. This also explains the sharper Dirac point in L-direction. Clearly, the bacterium significantly p-dopes the over-laying graphene sheet. It is important to note that the net gate capacitance will include the capacitance from SiO_2 and the bacterial dielectric ($C_{gate\text{-}net}^{-1} = C_{SiO2}^{-1} + C_{bacterium}^{-1}$). The other eight devices exhibited a reduction in current with an increase in gate voltage from - 85 to + 85 V (Figure 29a) for temperatures ranging from 10 K to 300 K (beyond 85 V, dielectric breakdown started). The variation in doping is attributed to bacteria having different ages which have different surface potentials.(*245*) Further work is required to obtain measurements by using a different cell (for example, a non-charged Gram-negative cell with no peptidoglycan membrane) to study the modification in the band-structure of wrinkled graphene.

To extrapolate the activation barrier, temperature studies were conducted at reduced doping levels at the maximum gate voltage (85 V). Two conduction regimes were identified: (i) high temperature (120 K to 300 K) and (ii) low temperature (10 K to 120 K). The activation energies ($G \propto exp(-E_A/kT)$) for the high temperature regime in T-direction was 1.69±0.01 meV higher than that in the L-direction (G is the conductance). The Schotkky barriers at the electrode-graphene junctions are expected to be similar for L- and T- transport; indicating a slightly increased barrier for transverse transport. Note that the barrier must not be affected by the carrier concentration. Therefore, the anisotropic wrinkles lead to suppressed carrier mobility in the T-direction.(*53*) This is speculatively attributed to the additional barrier due to longitudinal electron-hole puddles (potential

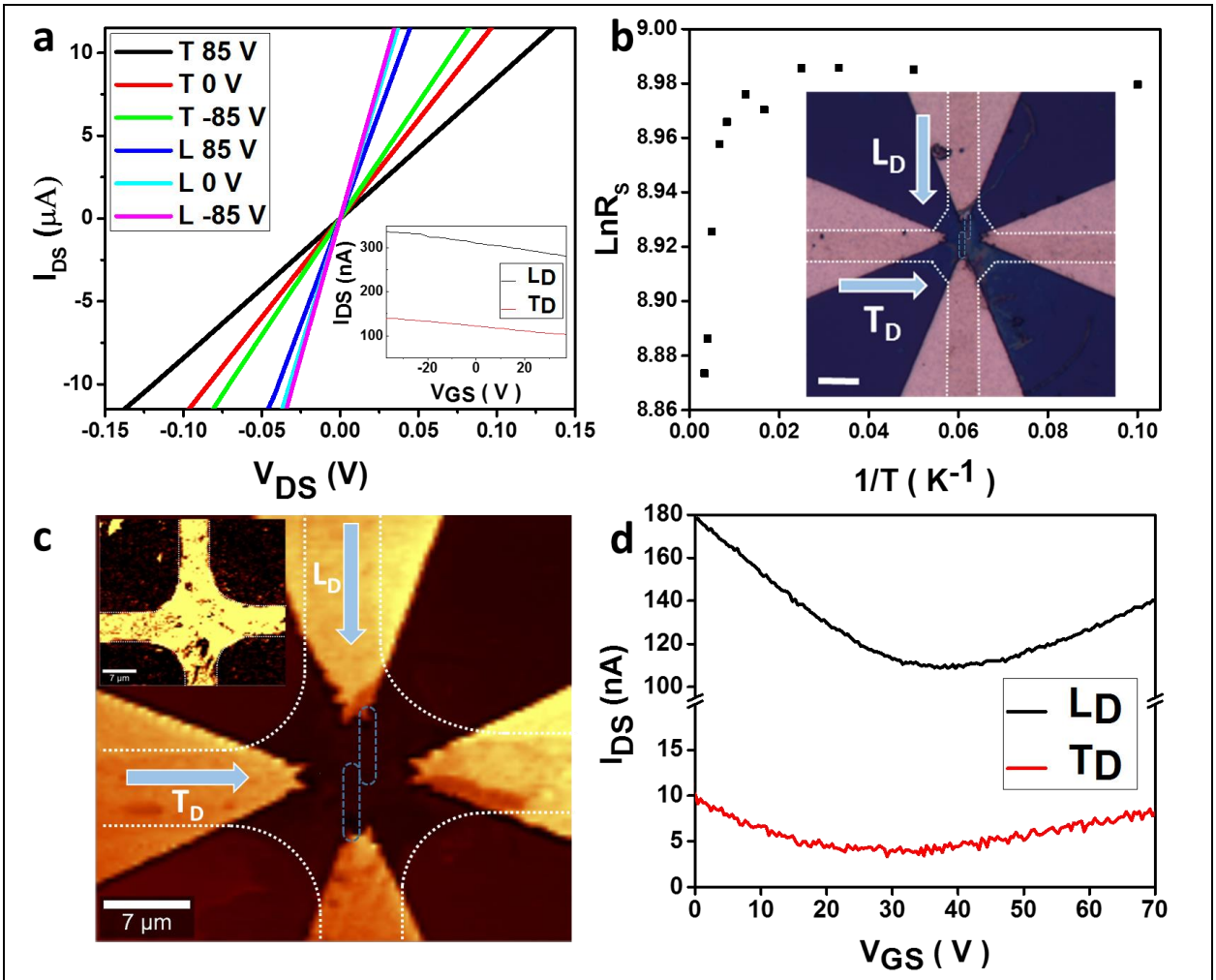

Figure 29. Longitudinal and Transverse carrier-transport measurements of wrinkled graphene on bacteria. (a) Schematic of graphene on bacteria FET device, and a typical optical image of device design after graphene placement via electrophoretic deposition with subsequent lithography technique: longitudinal direction (L_D) and transverse direction (T_D) are depicted with arrows. The scale bar is 10 mm. (b) Activation Energy: Resistances (at gate voltage of 85 V) at different temperatures were measured to determine the activation energy carrier transport. The inset figure shows Rayleigh scattering mapping of device, inset figure is Raman intensity mapping of graphene-2D peak. (c) I_{DS} - V_{DS} study at 10 K for L- and T- directions at different gate voltages shows the higher conductivity in the L-direction. Inset shows the FET characteristics of drain-source current (I_{DS}) vs. the gate–source voltage (V_{GS}) at 1 mV (V_{DS}). (d) FET transport characteristics of I_{DS} vs. V_{GS} at 10 K with clear demonstration of Dirac points.

barriers) expected to be parallel to the wrinkles. It is important to note that for folds, the

T-conductivity is expected to be higher.(*53*) This is a further confirmation of this being a wrinkle-only device. It must also be noted that at reduced temperature, thermal expansion of graphene is expected (–ve thermal expansion(*42*)), which might lead to relaxation of wrinkles. This is consistent with the significantly reduced activation energy for the low-temperature regime.

4.2.4.2 Mechanism studies: wrinkle attributions and pattern analysis

In order to theoretically calculate the wrinkle wavelength (λ) and amplitude (A), we applied the Föppl-von Kármán relationship for the thin film on the elastic substrate.(*28*) Equation (22) has been modified to include a pre-stretch factor (S) to incorporate the relative displacement of graphene with respect to the bacterial surface:

$$\lambda = 2\pi t\left(\frac{\bar{E}_g}{3S\bar{E}_B}\right)^{1/3} \tag{22}$$

$$A = \frac{\bar{L}t}{\lambda}\left(\frac{8v}{3(1-v)^2}\right)^{1/2} \tag{23}$$

$$P = \frac{w\bar{E}_B}{2t\left(\frac{\bar{E}_g}{3S\bar{E}_B}\right)^{1/3}} \tag{24}$$

Where the Young's modulus and Poisson's ratio of the graphene are $E_g = 1\,TPa$, and $v_g = 0.165$, respectively. $\bar{L}$ is the effective length of wrinkles and $\bar{L} = L/3$, where L is the length of bacteria. w is the perpendicular displacement of the graphene; P is the stress component by the bacterial cell wall acting perpendicular on graphene. See more detail in the Appendix for the calculation of S.

It is important to note that bacteria possess a cell-wall atop its membrane for which the Föppl-von Kármán equation may be applied; however, the wavelength obtained is more than 2 μm which is greater than the diameter of bacteria, and therefore bacterial cell wall does not show wrinkles. Graphene wrinkles can also be compared with wrinkles on raisins, λ = 1.5 mm (Figure 1), where with the grape skin being 30 times(*82*) stronger than the grape pulp implies a skin thickness of 111 μm. Remarkably, graphene being ~370,000 times thinner than grape skin is able to retain its mechanical characteristics while interacting with shrinking bacterium.

The deposited graphene experiences tensile strain in the radial direction due to stress from the curved bacterium. This causes graphenic compression in the perpendicular direction (axial direction) due to graphene's high Poisson's ratio (v= 0.165 = $-\Delta_y/\Delta_x$),(*42, 45*) leading to radial (or transverse) wrinkles on graphene (about 500 nm of length and 70 nm in width) (Figure 27a).(*42*) The observation was also validated by coarse-grained molecular dynamics (CGMD) and extended finite element method (XFEM) simulations. Here, a graphene model is laid on a bacterium on the substrate. The graphene sheet is pulled by the curved bacterium creating transverse wrinkles consistent with the experimental observation (Figure 27a. Clearly, the presence of radial wrinkles implies pre-tension in the graphene membrane on bacterium.(*19, 246*)

To create longitudinal wrinkles on the graphene sheets, bacterial shrinkage or water expulsion is required. However, the impermeability(*247*) and strength(*32*) of graphene does not allow the release of bacterial water. Therefore, a graphenic crack as an escape pathway was created under vacuum (10^{-5} Torr) and high temperature (~250 °C). Here,

the bacterium's volatile components vaporize, expand, and apply pressure on graphene (Figure 14a), which subsequently unzips(*248*) a crack. These unzipped cracks are clearly observed in the field-emission scanning electron microscopy (FESEM) micrographs. The crack formation on graphene is attributed to two mechanisms: (a) opposite polarity of thermal expansion coefficient between the graphene (-ve thermal expansion coefficient) and bacteria (+ve thermal expansion coefficient)(*249*), and (b) radial force due to applied pressure (estimated to be ~100 Bar). The region where graphene transitions from bacterium to SiO_2/Si substrate experiences a high differential strain due to a change in curvature (bacterium – SiO_2/Si boundary) and high tensile stress due to the large pressure difference across graphene (pressurized volatile cellular matter to vacuum). This causes longitudinal crack nucleation at the inflection points near the substrate as suggested by simulations: the crack is formed perpendicular to stress direction. The length of cracks (speculatively zig-zag edged(*248*)) is proportional to the length of bacteria or their chains; while the widths were mostly independent of the bacterial size at about 200 nm. In some cases, the graphene/bacteria system under vacuum did not have to be heated to form cracks (attributed to defects), which were always on the bacterium/substrate interface. With crack present, a pathway is created for volatile cellular content to escape causing (energetically favored) radial shrinkage of the bacterium. This induces strain on the interfaced graphene sheet, a resultant resistive force balancing the stress on bacterium cell wall to create wrinkles.

4.3 Wrinkled MoS_2 Characterization and Properties

Transferring MoS_2 thin film on a pre-stretched elastomeric substrate has been extensively applied to induce wrinkles in MoS_2,(*66, 67, 186, 250*) however, because of the weak

adhesion of MoS_2/elastomer interface (about an order of magnitude less than MoS_2/SiO_2 interface), slippage between MoS_2 and their elastomeric substrates limits the device applications.(*193*) The experimental investigation of the wrinkling effect on electronic properties based on transistor device measurements is still in its infancy. Here, we demonstrate that MoS_2 (on SiO_2 substrates) with wrinkles of different sizes can be found after mechanical exfoliation of MoS_2 flakes. The geometric shapes of the wrinkles (symmetric, asymmetric, and folded) affect the magnitude of strain, and in turn, influence the properties of MoS_2 as confirmed by Raman and photoluminescence spectra. We further show that by forming MoS_2 wrinkles, it is possible to modify the electron band structures, and manipulate the transport properties and optoelectronic response.

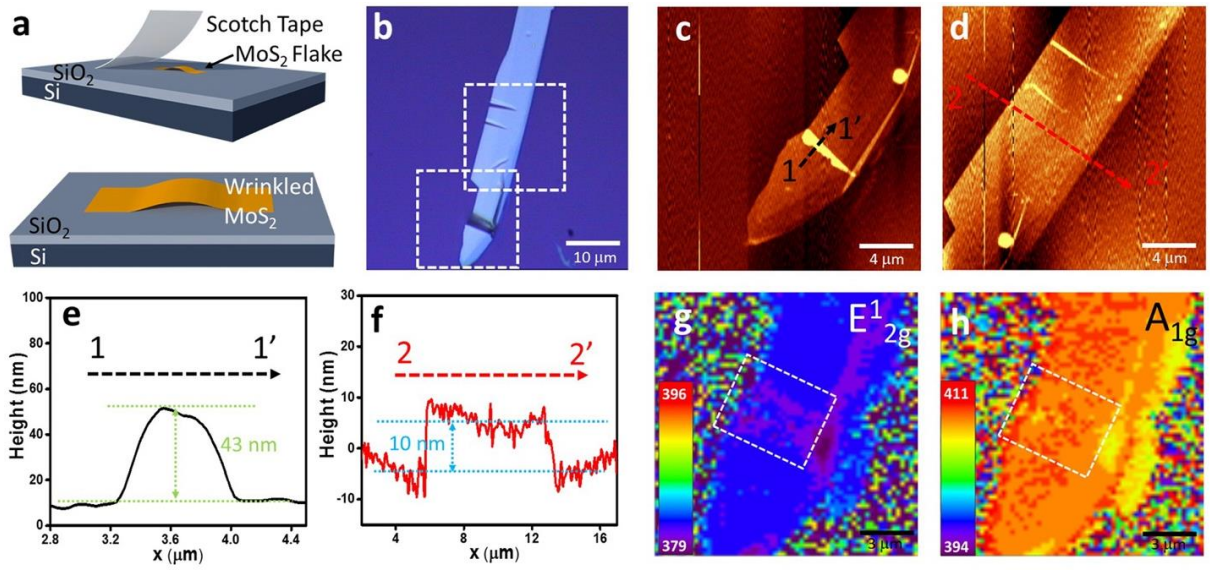

Figure 30. Wrinkled MoS_2 on SiO_2. (a) Schematic illustration of wrinkled MoS_2 on SiO_2 substrate. (b) Optical image of a wrinkled MoS_2. (c) and (d) AFM characterization of the wrinkled MoS_2 in (b). (e)Wrinkle's height profile along the black dashed line (1-1') in (c). (f) Thickness profile of MoS_2 flake along the red dashed line (2-2') in (d). (g) and (h) Raman position mapping of E^1_{2g} mode and A_{1g} mode, respectively. The A_{1g} mode is less affected than the E^1_{2g}. White dashed squares are wrinkled regions. The units of the scale bars in (g) and (h) are cm^{-1}.

Samples of wrinkled MoS_2 flakes on SiO_2 substrates were found after exfoliation (one in ten times the sheet had wrinkles), as shown in Figure 30a, Figure 31, and Figure 33. The adhesion between MoS_2 and the SiO_2 substrate can cause the separation of thin MoS_2 flakes from the bulk MoS_2 in the exfoliation process.(*68*) During the release of the tape, its adhesion with MoS_2 induces partial delamination of MoS_2 from the substrate leading to the bending and wrinkling of MoS_2. The interplay between the interfacial adhesion of SiO_2 with MoS_2 and the bending energy of the MoS_2 flake results in a stable partially detached, wrinkled MoS_2. It is important to note that the adhesive tape (Scotch tape) retains some unpeeled MoS_2 and therefore has no contact with the peeled MoS_2 flake. Therefore, there is no tape-induced electrostatic charge at the interface of MoS_2 flakes.

4.3.1 Optical and AFM characterization

A typical wrinkled MoS_2 film on SiO_2 as observed under an optical microscope is shown in Figure 30b. Three-dimensional profiles of wrinkles in MoS_2 obtained via atomic force microscope (AFM) is shown in Figure 30c and 30d. Both the height of the wrinkle (~43 nm with a wavelength of ~0.8 μm) and the thickness of this MoS_2 film (~10 nm) were measured (Figure 30e and 30f). Interestingly, in most of the cases, the wrinkles were stable and did not slip on SiO_2. This is attributed to the relatively strong interfacial adhesion between MoS_2 and SiO_2 surface. However, in some cases (usually small area flakes), the wrinkles were flattened by the slipping of MoS_2 (Figure 33). It is important to note that slipping/sliding limits the uniform uniaxial strain load on atomically thin 2D crystals (e.g. graphene, MoS_2) in experimental bending geometries.

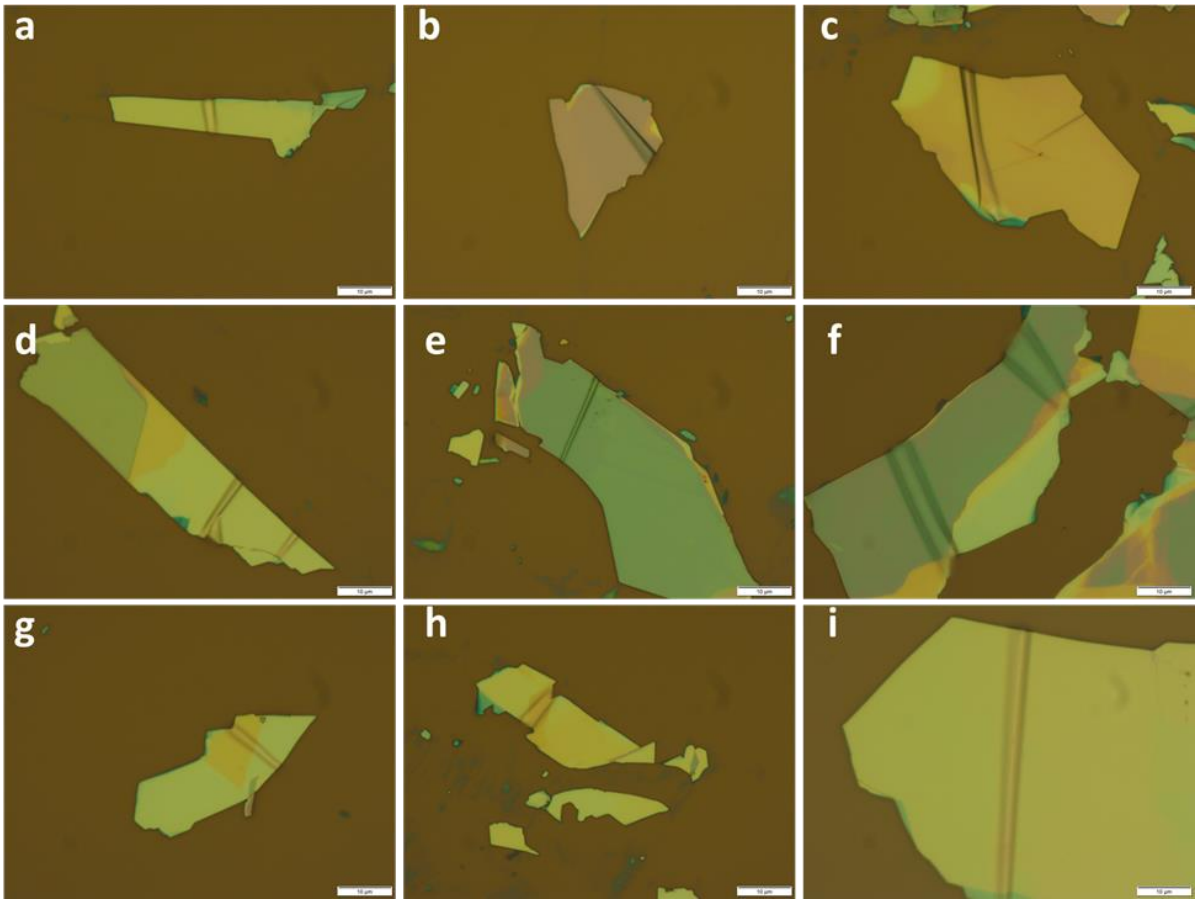

Figure 31. Optical images of some wrinkles in MoS_2.

We propose that the attributes of the wrinkles can be used to calculate the adhesion energies (γ) (between MoS_2 and its supporting substrates) and deformation ($\Delta = \frac{L_0 - L_p}{L_0}$) *via* force and energy balance:(*193*)

$$\gamma = \frac{\pi^4 E t^3 A^2}{6\lambda^4} \tag{26}$$

$$\Delta = \frac{3\gamma\lambda^3}{2\pi^2 E t^3 L_p} \tag{27}$$

Where E is the Young's modulus of the MoS_2, A is the amplitude and λ is the wavelength of the wrinkle, t is the thickness of the thin film, and L_0 and L_p are the length and projected length of the wrinkled MoS_2 on substrates, respectively. The height of the wrinkle is not required in the deformation calculation.

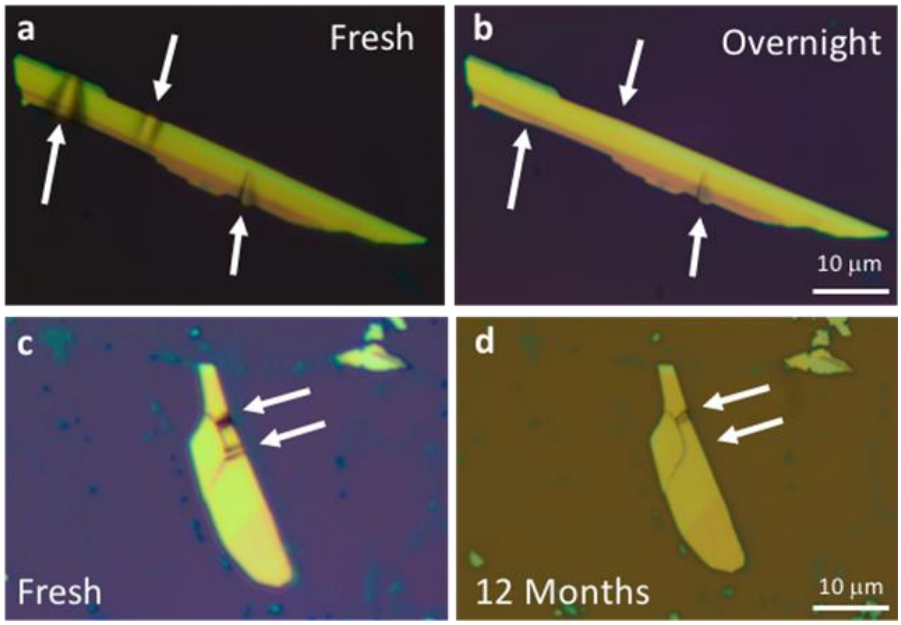

Figure 32. **Wrinkles flattening and disappearing through sliding. (**a) Optical image of a wrinkled MoS_2. (b) Same MoS_2 flakes in (a) after overnight without any treatment. (c) Optical image of a wrinkled MoS_2. (b) Same MoS_2 flakes in (c) after 12 months without any treatment. Arrows indicate the positions of wrinkles in fresh wrinkled MoS_2.

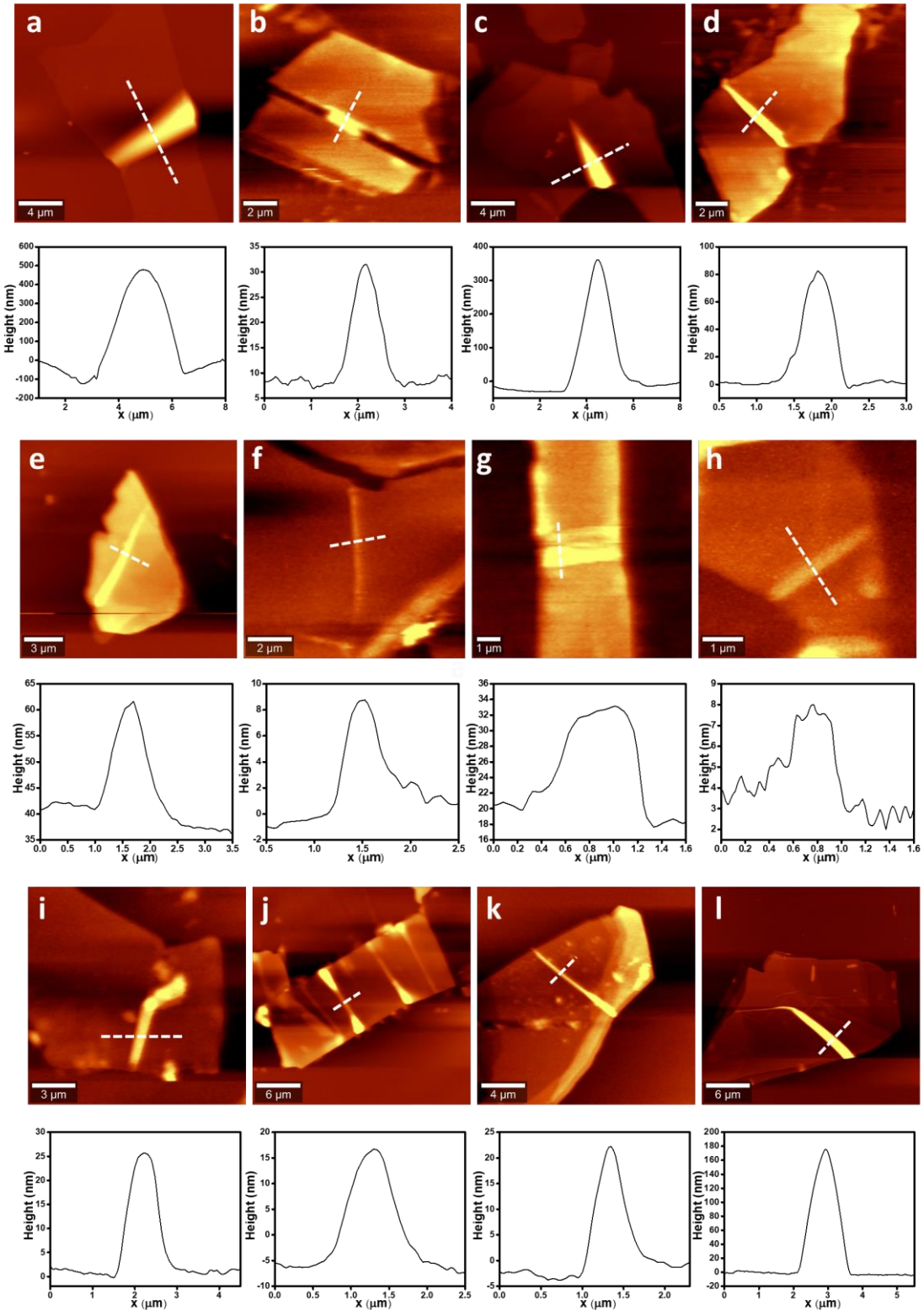

Figure 33. AFM characterization of wrinkles in MoS_2.

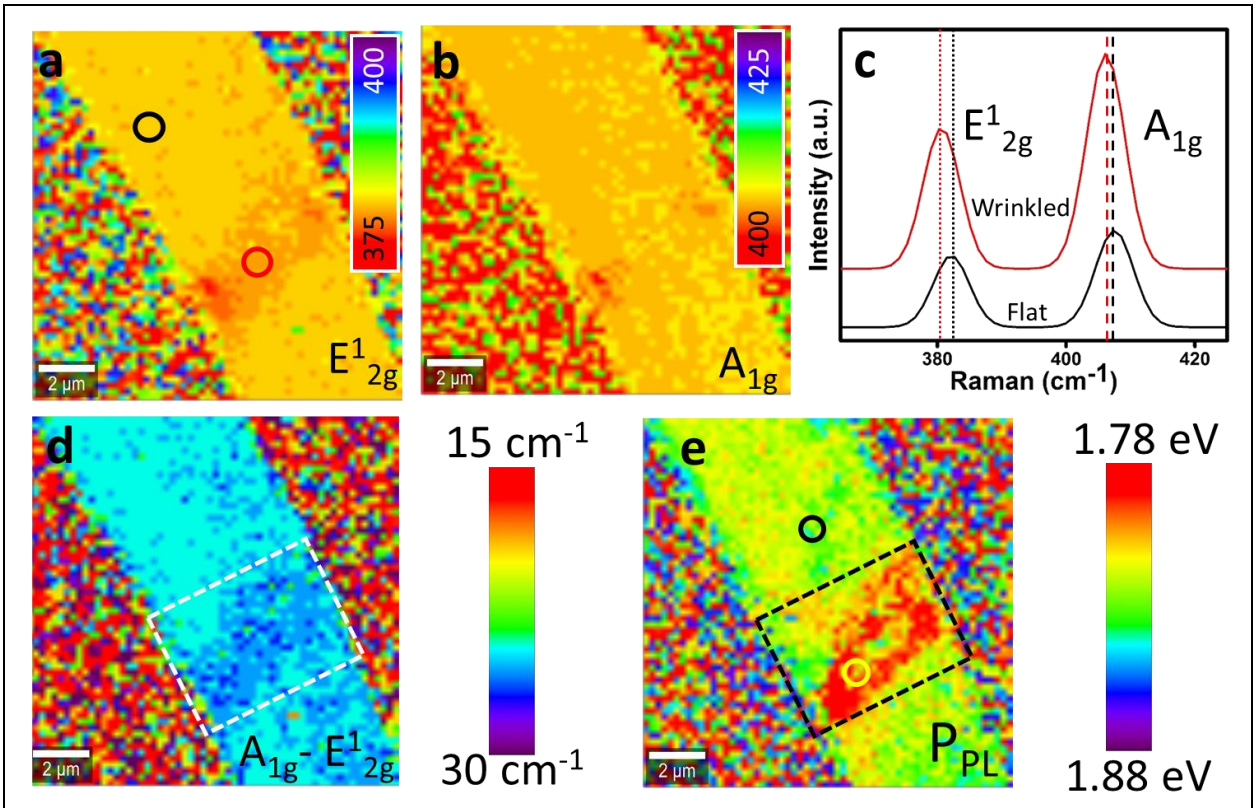

Figure 34.Raman and PL position mapping of symmetric wrinkles in MoS_2 on SiO_2. (a) and (b) Raman position mapping of E^1_{2g} mode and A_{1g} mode, respectively. The A_{1g} mode is less affected than the E^1_{2g}. White dashed squares are wrinkled regions. The units of the scale bars in (a) and (b) are cm^{-1}. (c) Typical Raman spectra for wrinkled (red) and flat (black) MoS_2. Dotted lines and dashed lines are the positions of E^1_{2g} mode and A_{1g} mode, respectively. (d) Raman position mapping difference between E^1_{2g} mode and A1g mode (A_{1g} - E^1_{2g}). White dashed rectangle is wrinkle effected region. (e) PL energy mapping of A exciton peak. Black dashed rectangle is wrinkle effected region.

4.3.2 Raman and PL spectra

A wrinkle in MoS_2 induces modification of its atomic structure, leading to a considerable change in the lattice-vibration (phonon frequency shift), which can be detected through Raman spectroscopy. In the wrinkled region, the two most prominent Raman peaks, E^1_{2g} mode (~384 cm^{-1}) and A_{1g} mode (~405 cm^{-1}), are red-shifted (vibrations softening)

compared to the flat region as shown in Figure 30g and 30h. The A_{1g} mode (corresponding to the sulfur atoms vibration along out-of-plane direction) is less sensitive to wrinkling than the E^1_{2g} (sulfur and molybdenum atoms vibration in the crystal plane). However, in some samples, there is a negligible shift in A_{1g} peak in the wrinkled region (Figure 30h). This is attributed to the existence of doping-induce red shift in flat region of A_{1g} position. However, the doping effect is weaker as less doping in the wrinkled region, as shown later. Both theoretical and experimental results show that the shift in the Raman peaks linearly depends on the applied strain,(*66-68*) therefore, the deformation of the sample can be quantified through Raman spectra. The shift of E^1_{2g} peak position for this wrinkle is ~ 1.1 cm^{-1} as shown in Figure 30g. Plugging this into the relationship between strain and mode position shift,(*66-68*) the estimated deformation is ~ 0.55 %. This is consistent with the deformation obtained from the Equation (27) (also ~0.55%). Further, the shift of E^1_{2g} peak position for this wrinkle is ~ 2 cm^{-1} as shown in Figure 25. Plugging this into the relationship between deformation and mode position shift (2 cm^{-1}/% deformation), the estimated deformation is ~ 1%. This is consistent with the deformation obtained from the Equation 26, which is ~1.11%.

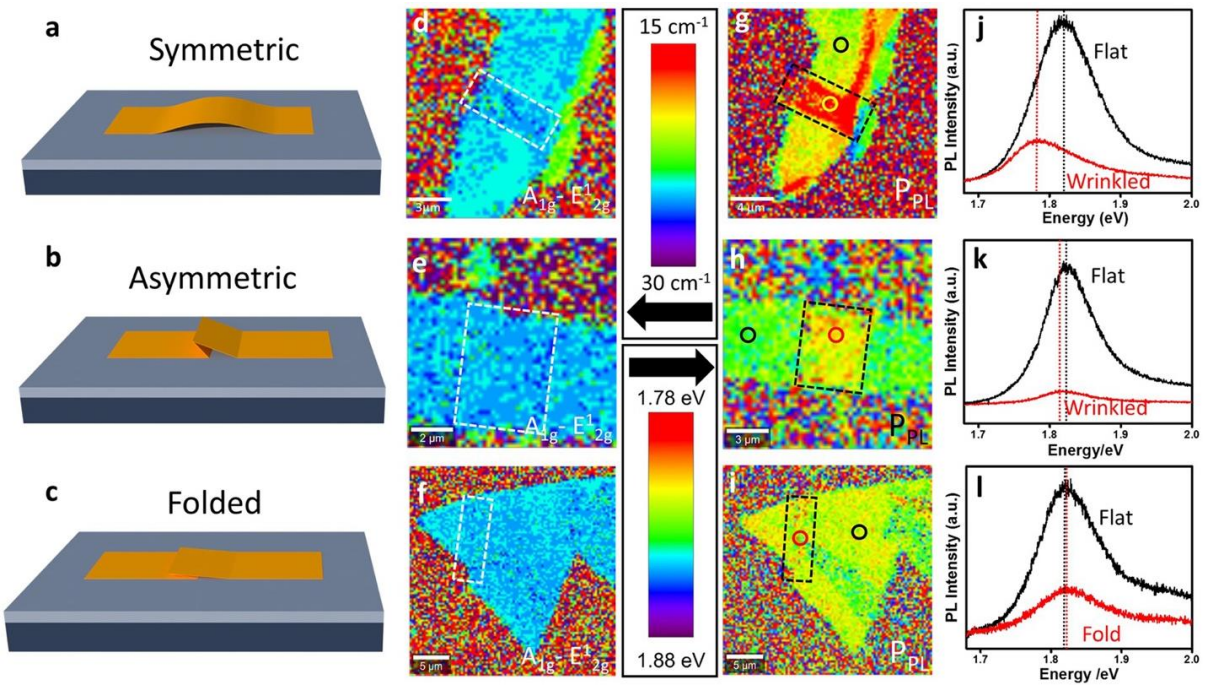

Figure 35. Raman and photoluminescence (PL) characterization of different kinds of wrinkled MoS_2. (a) to (c) Schematic illustrations of symmetric (a), asymmetric (b) and folded (c) wrinkles in MoS_2. (d) to (f) Raman position difference between E^1_{2g} mode and A_{1g} mode (A_{1g} - E^1_{2g}) of symmetric (d), asymmetric (e) and folded (f) wrinkles in MoS_2. White dashed rectangles are wrinkle effected regions. The scale bar is from 15 to 30 cm^{-1} for all three Raman position mappings. (g) to (i) PL A peak position mappings of A exciton peak for the symmetric (g), asymmetric (h) and folded sample (i) wrinkles in MoS_2. The scale bar is from 1.78 to 1.88 eV for all three energy mappings. The black dashed rectangles are wrinkle effected regions. (j) to (l) Typical PL spectra profiles measured on flat (black circles) and on a wrinkled (yellow or red circles) regions. (j) The A peak of symmetric wrinkled MoS_2 has an obvious red shift to that of flat MoS_2. (k) The A peak of symmetric wrinkled MoS_2 has a slight red shift to that of flat MoS_2. (l) The A peak of folded MoS_2 has same position to that of flat MoS_2.

Via the exfoliation process, we observed three different kinds of geometric shapes of wrinkles: symmetric (> 30 samples), asymmetric (> 10 samples) and folded (> 3 samples), as depicted in Figure 30e, Figure 34a to c, and Figure 25, Figure 31, and Figure 33. Although most samples were symmetric wrinkles, it is challenging to controllably form a

defined shape of a wrinkle by this method. Asymmetric and folded wrinkles were typically observed in thinner flakes, attributed to reduced stiffness and instability.

The larger red-shift of the E^1_{2g} peak than A_{1g} peak in the wrinkled region of symmetric wrinkles leads to slight increase in the difference between the two peaks positions (A_{1g} - E^1_{2g}) (Figure 35d). However, in asymmetrical and folded MoS_2, the difference between these two peak-positions remains nominally unchanged as shown in the A_{1g} - E^1_{2g} mappings (Figure 35e and 35f). This indicates that there is no obvious strain in the wrinkled region in asymmetrical and folded MoS_2. This is attributed to stronger wrinkle-induced strain in symmetric wrinkles than in the asymmetric or folded wrinkles, where a part of the bending energy is compensated by the sharp peak in the asymmetrical regions. Further, the Raman peaks do not change on the small wrinkles on the relatively thick MoS_2 flakes as shown in Figure 36 and 37. This is due to the wrinkle sizes being too small to have obvious strain effects.

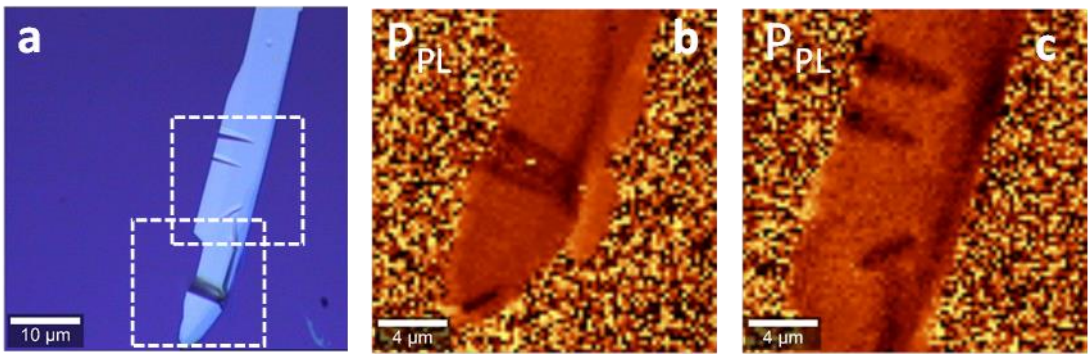

Figure 36. Wrinkled MoS_2 on SiO_2 and photoluminescence spectroscopy of wrinkled MoS_2. (a) Optical image of a MoS_2 flake with several wrinkles. (b) and (c) PL energy mappings of A exciton peak of square regions in (a). The wrinkled induced reduction of optical band gap is clear shown in (b) and (c). And the widths of band gap modified regions are much larger than the wavelength of the wrinkles.

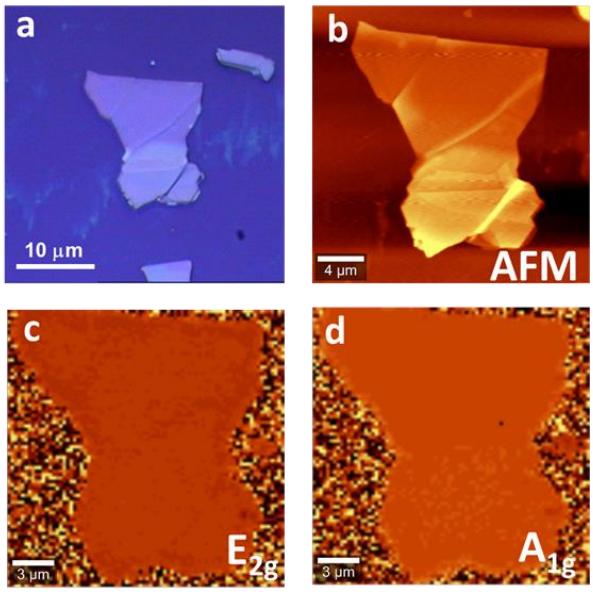

Figure 37. Small wrinkles in MoS_2 on SiO_2. (a) Optical image of a small wrinkle in MoS_2. (b) AFM characterization image of the same wrinkled in (a). (c) and (d) Raman position mapping of E^1_{2g} mode and A_{1g} mode, respectively.

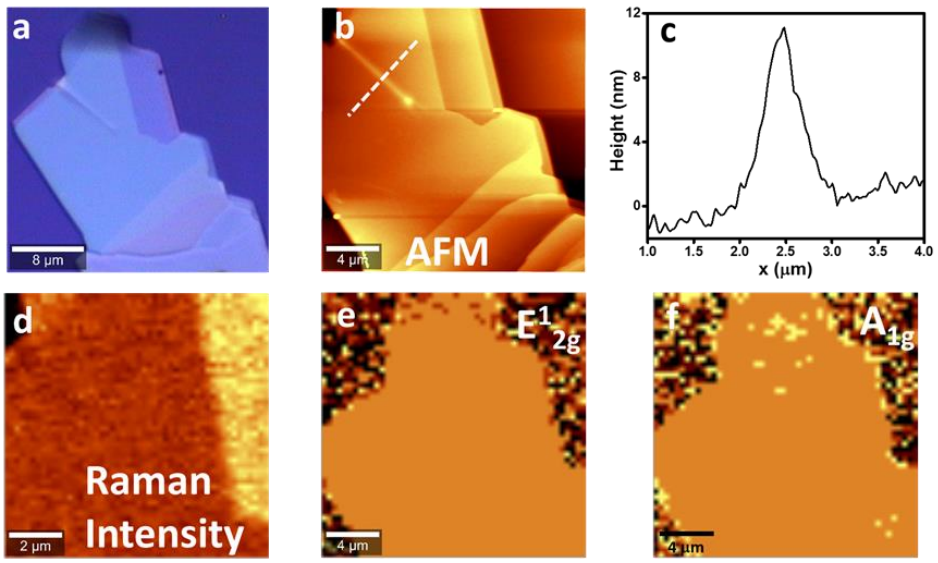

Figure 38. Small wrinkles in MoS_2 on SiO_2. (a) Optical image of a small wrinkle in MoS2. (b) Atomic force microscopy characterization image of the same wrinkled in (a). (c) Height profile of along the dashed line in (b). (d) Raman intensity of wrinkled region in MoS_2. Raman position mapping of E^1_{2g} (e) and A_{1g} (f).

Although multilayer MoS_2 is an indirect bandgap semiconductor, its photoluminescence (PL) spectrum is determined by the direct bandgap. The indirect bandgap transition originating from hot luminescence (part of energy consumed by phonon vibration for momentum conservation)(*179*) only contributes to a very weak photoluminescence peak.(*178*) A pronounced redshift of PL peak in the wrinkled region exists in comparison to that of the flat region in the same flake as shown in Figure 35g. This indicates that the uniaxial strain reduces the energy of the direct bandgap transition (optical band structure around the K point).(*66*) These dissimilar shapes of the wrinkles lead to different strain distribution and have dissimilar photoluminescence responses. The red shift of the PL peak for symmetric wrinkles is much larger than that for the asymmetric and folded wrinkles, as shown in Figures 35g to 35i, consistent with a previous study on a decrease in direct bandgap with an increase in strain.(*67*) Although the asymmetric wrinkle (Figure 25) shows a higher mechanical plane deformation than the symmetric one (Figure 30e), the red shift of the A peak (30 meV) in symmetric wrinkle is higher than that (10 meV) in the asymmetric one (Figure 35j, 35k). Consistent with the previous studies on thin-layer MoS_2 films,[8] the optical bandgap reduction is about 40~60 meV/% deformation (See Appendix for more details, Table VI and Figure 39). Here, the PL peak position of A exciton is thickness-insensitive, since K points consist of strongly localized d orbitals of Molybdenum atoms.[34] The PL peak position shows no change for the case of folded wrinkles (Figure 35l). Further, the photoluminescence-modification is localized in asymmetric wrinkles (4.5 μm, as shown in Figure 35), however, the photoluminescence is modified (4 μm) in a region 2-5 times larger than the symmetric wrinkle (0.8 μm), as

shown in Figure 35g, 34, and 36. Further, the deformation of the wrinkle in Figure 30 is ~ 0.55 %, and the reduction of optical band gap in this wrinkle is ~ 33.9 meV or 61 meV% deformation. More PL versus deformation data are shown in Figure 39.

It should be pointed out that the shape-induced modifications of Raman spectra and the photoluminescence response of MoS_2 wrinkles implies that the phonon softening and optical bandgap reduction is dominated by the strain instead of surface doping of MoS_2. If the doping variation in MoS_2 (due to partial separation from the substrate) was predominant towards Raman and PL responses, the symmetric and asymmetric samples should have behaved similarly (there is no surface-induced doping in the wrinkled regions of any shape of wrinkles). Note that the intensity of photoluminescence in the wrinkled regions is lower than the intensity on the flat regions. This is expected since the focal plane of the confocal laser was on the flat MoS_2 surfaces (not on the wrinkles with varying height) and due to the Fresnel effect (less light back to detector from edges of wrinkles, as shown in Figure 31). The bandgap determined by photoluminescence spectroscopy differs from the bandgap determined by the electrical transport with the difference of the exciton binding energy. Recent theoretical studies have shown that the exciton binding energy is strain-insensitive and is of the order of 100 meV; therefore, the magnitude of transport bandgap is also expected to be reduced with strain.(*203, 251*)

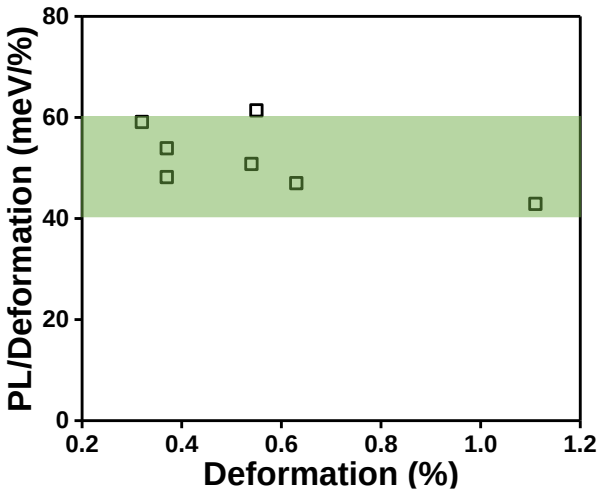

Figure 39. PL versus deformation in MoS_2 flakes.

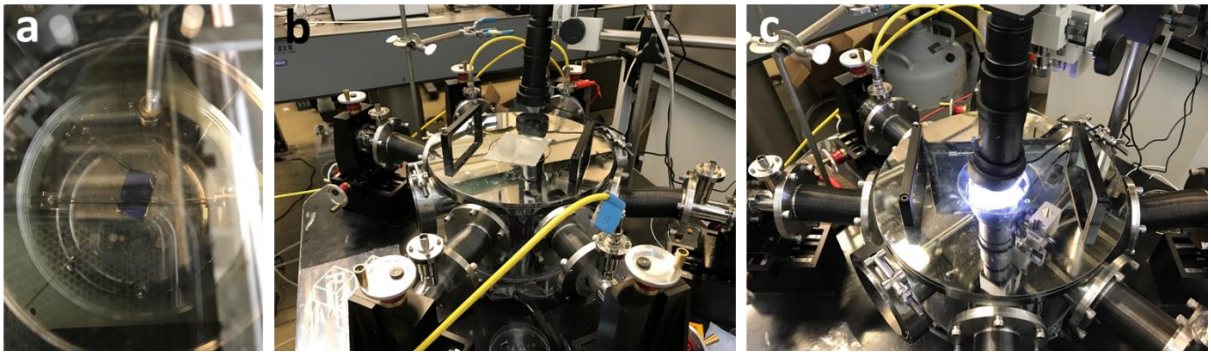

Figure 40. Electrical characterization experiment setup. (a) Electrodes Connection on the device. (b) and (c) Electrical characterization in dark and light conditions, respectively.

4.3.3 Electrical characterization and device performance

To study the effect of wrinkle-induced doping variation on the charge-carrier transport, we prepared wrinkled and non-wrinkled (flat) MoS_2 field-effect transistors (Figure 41a to 41c). Only symmetric wrinkles were studied in these devices since the asymmetry and/or folds in wrinkles introduce extra barriers at the sharp curvature regions in comparison to the

symmetric wrinkles. The wrinkles are oriented in the transverse direction to the current flow (current across the wrinkle). To determine the transport-barrier, the temperature dependence of the electrical conductivity at different gate voltages was analyzed (Figure 41g and 41h). The conduction behavior was found to be different for high temperature (100 to 300 K) and low temperature (15 to 100 K) ranges. This is because that the charge transport is thermal activated and the transport is dominated by hopping of localized states (smooth temperature-dependence at low temperature region). The activation energy ($G \propto exp(\frac{E_A}{kT})$) was 80 ± 13.3 meV and 18 ± 6.4 meV (at $V_{DS} = 0\ V$) for the wrinkled and flat MoS_2 devices at high temperature regions (100 to 300 K), respectively. This indicates a >100 meV increase of barrier for the carriers to flow across the wrinkle (see Figure 41i and Figure 41j). The Schottky barrier was excluded from consideration due to the ohmic I_{DS}-V_{DS} behavior at small V_{DS} values (Figure 41j insert). This ohmic behavior is attributed to doping in flat MoS_2 as shown later.(*252*) The electrode-MoS_2 junctions are expected to be similarly doped for wrinkled and flat devices, since the electrode-MoS_2 junctions are on flat MoS_2 and far away (~ 2 μm) from the wrinkled region. It should be noted that the transport-barrier is minimally affected by contact resistance, which is much smaller than the channel resistance.(*253*) The higher barrier across the wrinkle is attributed to the local carrier-concentration redistribution due to the surface doping variation induced built-in potentials, as shown later.

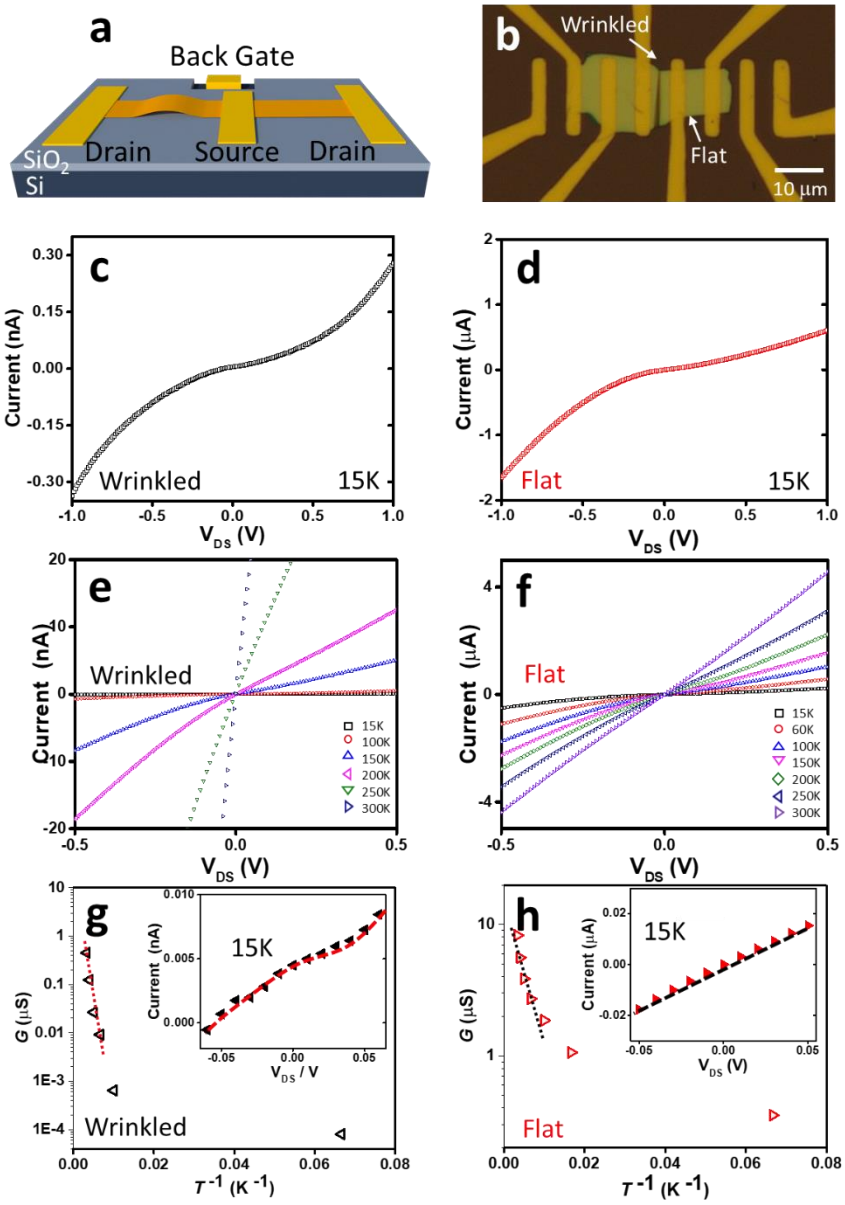

Figure 41. I_{DS}-V_{DS} (source-drain current versus source-drain voltage) characterization and temperature study of wrinkled and flat MoS_2 devices. (a) Schematic illustration of the wrinkled device. (b) Optical image of typical wrinkled and flat MoS2 devices. (c) and (d) Source-drain current (I_{DS}) versus source-drain voltage (V_{DS}) at different temperatures for wrinkled and flat MoS_2 devices, respectively. (g) and (h) Activation energy studies of wrinkled and flat MoS_2 devices, respectively. The inserts are the typical I_{DS} versus V_{DS} at 15K for wrinkled and flat MoS_2 devices, respectively.

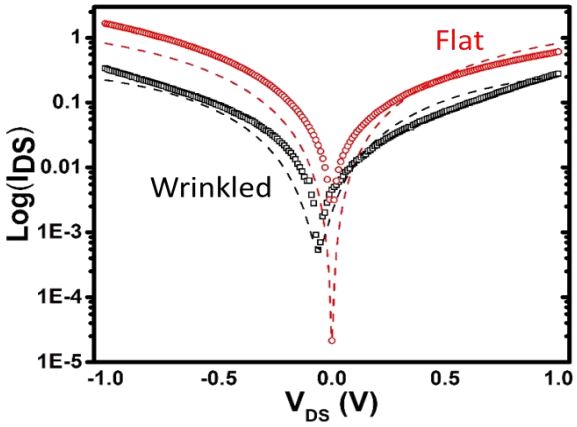

Figure 42.Typical log(I_{DS})-V_{DS} characterization (dashed lines are fitting of data).

The back gated field-effect mobility of these MoS_2 devices can be estimated based on the equation:(*197*)

$$\mu = \frac{L}{W\left(\frac{\varepsilon_r \varepsilon_0}{D}\right)V_{DS}} \frac{dI_{DS}}{dV_{BG}} \tag{28}$$

Where, L and W are the length and width of MoS_2 channel, respectively; ε_r is relative permittivity and ε_0 is vacuum permittivity (8.854×10^{-12} F·m^{-1}), and D is the gate-oxide thickness. The mobility in wrinkled part of MoS_2 (estimated by two-plate model (with two dielectric layers in series (285 nm of SiO_2 and an averaged 300 nm of air) and cylinder on a conducting plate model) is 1.4~16.3 cm^{2}V^{-1}S$^{-1,}$ which is larger than the values of flat-MoS_2 devices (1.03 cm^{2}V^{-1}S^{-1}) (Figure 5c and 5d in dark condition at 300K with $V_{DS} = 1V$) (See the calculation details in Appendix). The higher mobility in the wrinkled MoS_2 could be due to the suppression of electron-phonon coupling by the tensile strain (lower lattice scattering) and low doping concentration (reducing impurities scattering) in the wrinkles.(*222, 254*)

Thin flakes of MoS_2 in contact with SiO_2 are known to electron-dope (n-dope).(*87*) This is consistent with the behavior of our MoS_2 devices as shown in the carrier transport behavior in Figure 43a and 43b, where the electron transport is dominant over the entire range of gating voltage (-40 to 40 V). This n doping effect in the flat MoS_2 also results in a higher conductivity of carriers than that of the wrinkled MoS_2 devices (higher resistance in wrinkled devices). The wrinkled samples show an improvement in subthreshold swing (Figure 43c and 43d). Instead of one type of resistance (R_F) in a flat-MoS_2 device, wrinkled-

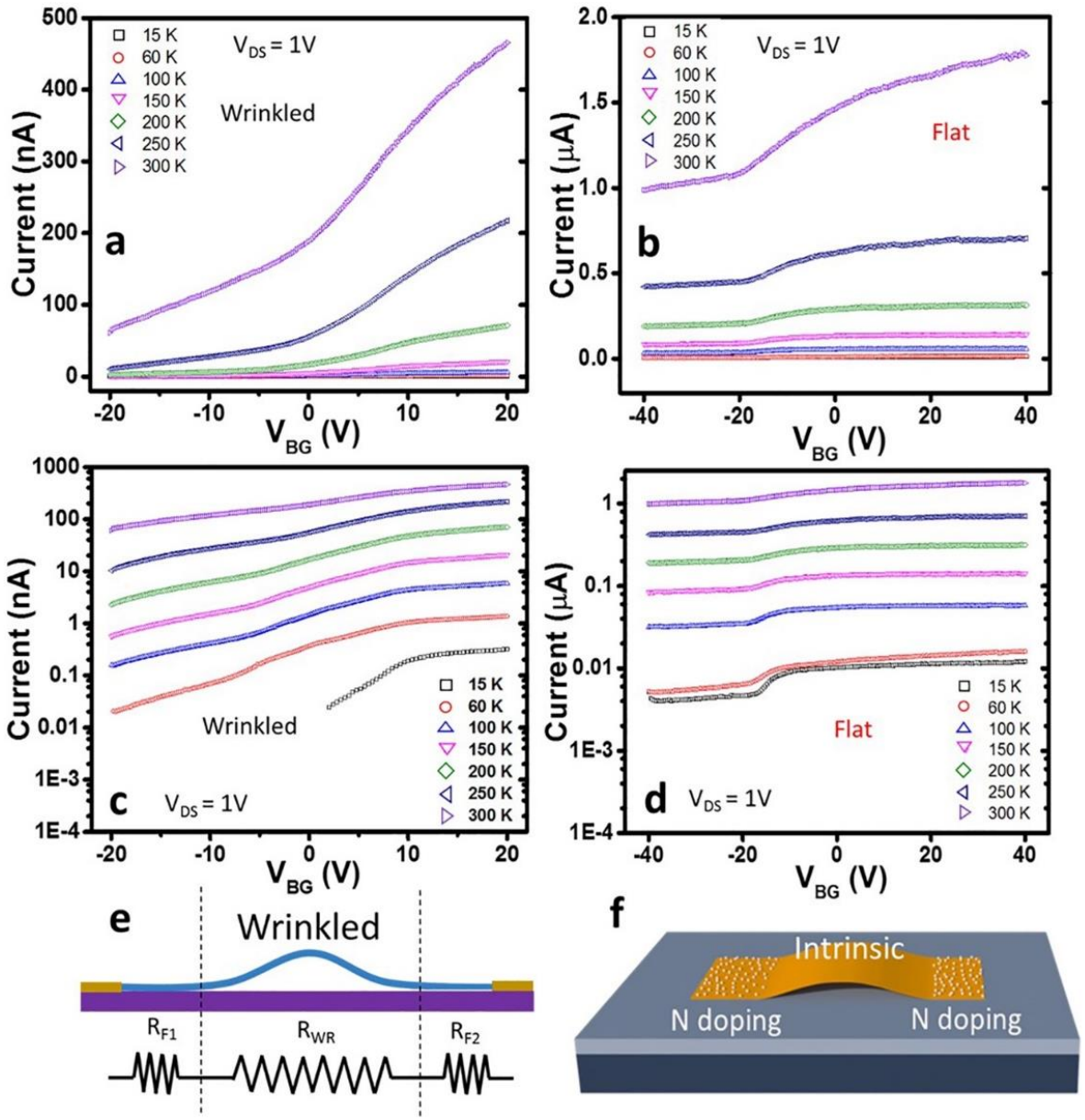

Figure 43. I_{DS}-V_{BG} (source-drain current versus back gating voltage) characterization and temperature studies of wrinkled and flat MoS_2 devices. (a) and (b) I_{DS} in linear scale versus V_{BG} at different temperatures for wrinkled and flat MoS_2 devices, respectively. (c) and (d) I_{DS} in $\log_{10}$ scale versus V_{BG} at different temperatures for wrinkled and flat MoS_2 devices, respectively. The current for wrinkled MoS_2 device at 15K in voltage lower than 12V is very small and negative (instrument error), thus, only the current in the 12 to 20 V range is shown in $\log_{10}$ scale in (c). (e) Schematic side-view wrinkled MoS_2 device showing the wrinkled MoS_2 resistor (R_{wR}) and two flat MoS_2 resistors in series (R_{F1} and R_{F2}). (f) Schematic illustration of wrinkled MoS_2 with n-doping (white spheres) from substrate in the flat parts, and the wrinkled part is suspended and intrinsic.

MoS_2 devices can be considered as having three resistances in series: $R_W = R_{F1} + R_{WR} + R_{F2}$, where $R_{F1}$and R_{F2} are the resistance of flat regions on the left and right sides of the wrinkle, respectively, and R_{WR} is the resistance of the wrinkled region, as shown in Figure 43e. At 300K, the resistance of a flat-MoS_2 device is about one-twentieth of ($\frac{R_F}{R_W} = \frac{1}{20}$) the effective resistance of the wrinkled one. The resistance can be written as: $R = \frac{L}{ne\mu A}$, where L is the length of MoS_2 between two electrodes, n is the carrier concentration of the channel, e is the elementary charge, μ is the mobility of the carriers, and A is the area of the channel. We assume that the difference between channel areas is negligible, and the carrier-mobility on the wrinkled region of MoS_2 is $1.4 \sim 16.3$ times larger than the carrier-mobility on the flat MoS_2 ($\mu_W \approx 1.4 \sim 16.3\,\mu_F$). This yields: $\frac{R_F}{R_W} = \frac{\frac{L_F}{n_F}}{\frac{L_{F1}}{n_F}+\frac{L_{F2}}{n_F}+\frac{L_{WR}}{7.5\,n_{WR}}} \approx \frac{1}{20}$ (with $V_{DS} = 1V$and $V_{BG} = 0V$ at 300K). From the experimental data, we obtained $L_F \approx 5\,L_{WR}$; therefore, $n_F \approx 134 \sim 1564\,n_{WR}$ (see detail in Appendix The doping concentration in SiO_2 supported MoS_2 is about $n_F = 10^{13}$,(*255-259*) which brings the carrier concentration in the suspended part of MoS_2 $n_{WR} \approx 6\times10^9 \sim 7\times10^{10}$ cm^{-2}. Since the wrinkled part is suspended in the air without surface induced doping, n_{WR} is expected to be closed to intrinsic carrier concentration ($n_{WR} \approx 10^{10}$ cm^{-2} at 300K),(*253*) as schematically shown in Figure 43f.

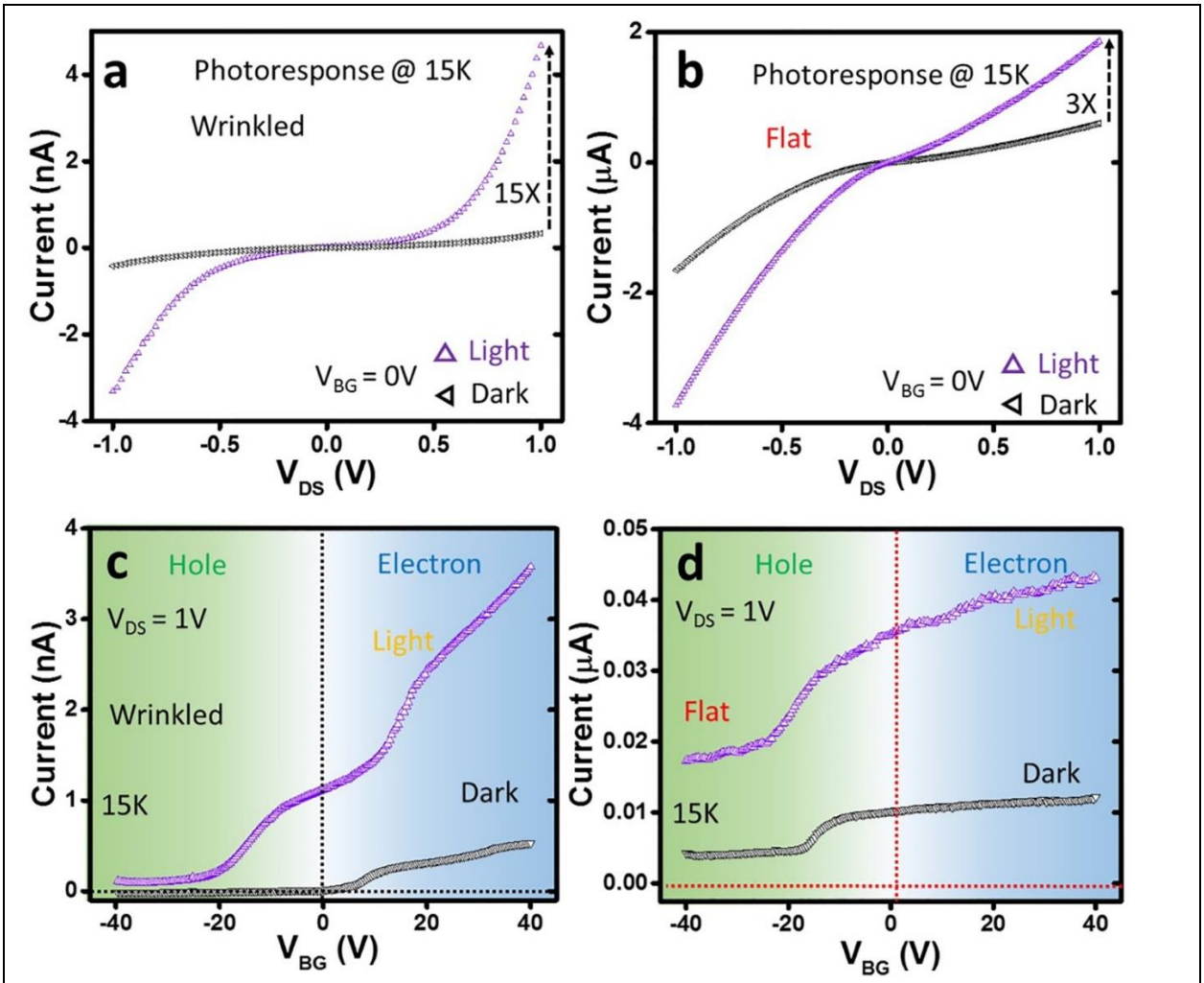

Figure 44. Photo-response studies of wrinkled and flat MoS_2 devices. (a) and (b) Photo-response measurements of wrinkled and flat MoS_2 devices without gating at 15 K, respectively. (c) and (d) Typical source-drain current (I_{DS}) versus back gating voltage (V_{BG}) at 15 K for wrinkled and flat MoS_2 devices, respectively.

The wrinkle-induced strain and doping variation in MoS_2 significantly modify the photo-response of the MoS_2 devices. The photo-response studies were conducted on the both wrinkled and flat devices (Figure 44). The photocurrent was 3-fold higher than dark current (V_{DS} = 1 V and V_{BG} = 0 V) for the flat MoS_2 devices, which is consistent with previous photo-switching studies in similar conditions.(*197*) Interestingly, this photo/dark current ratio in wrinkled MoS_2 devices was much higher (15-fold) (Figure 44a and 44b).

The gate-induced on/off ratio of dark current in flat MoS_2 device (3 for the ±20 V range of back gating) was much lower than that of wrinkled MoS_2 device (3500 for the ±20 V range of back gating) (Figures 44c and Figure 45). This is more than 1000-fold enhanced current-rectification. Built-in potentials (V_{bi}) induced by different doping levels within the

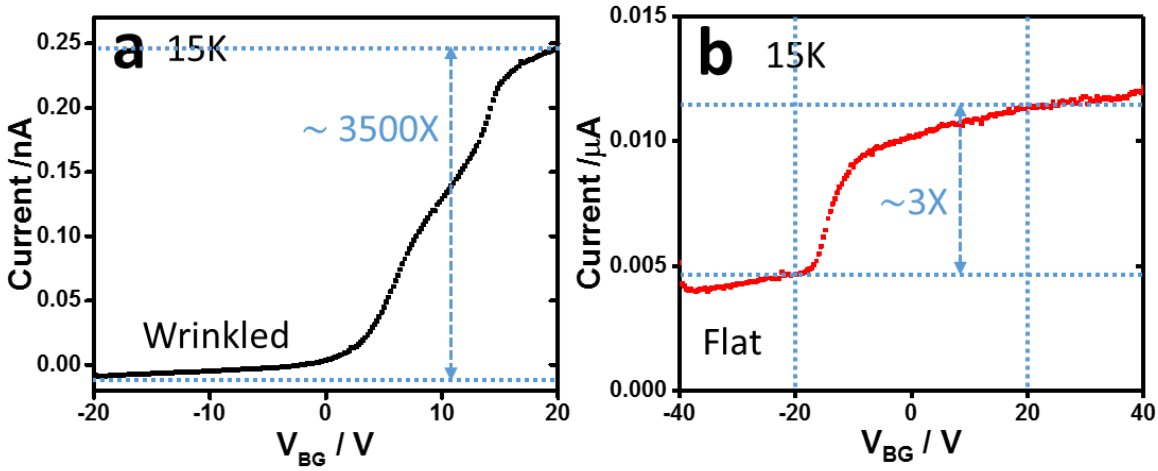

Figure 45. I_{DS}-V_{BG} characterization of wrinkled and flat MoS_2 devices in dark condition. (a) and (b) Source-drain current (I_{DS}) versus back gating voltage (V_{DS}) at 15 K for wrinkled and flat MoS_2 devices, respectively.

wrinkled MoS_2 (interfaced region (n-doped from the substrate) and suspended intrinsic regions) suppress the current under small bias (Figure 46a and 46b). However, a large voltage bias ($V_{DS} \gg V_{bi}$ and $V_{BG} = +20V$) is expected to allow electron tunneling in the depletion region (Zener process), which greatly enhances the flow of electron and provide a considerable improvement in the on/off ratio (Figure 44c). We noticed that there is anomalous gate modulation (change of slope) in wrinkled devices (both in light and dark conditions, as shown in Figure 44c and Figure 45a). This also can be seen as the evidence of the doping variation and barriers in wrinkled devices: at low gate voltages, the low chance for Zener process is the limitation factor for currant flow (small slopes in

the small gating voltage region in transfer curves), while the tunneling limitation is overcome as the carrier concentration increase at higher gating voltage (large slopes in the high gating voltage). Under light exposure, the wrinkled devices exhibited more than 10-fold higher gating-induced on/off ratio than flat devices (Figure 44d and 46c). Higher doping density is supposed to enhance photo-responsivity,(*197*) however, this is not the case here. The increased light response for the wrinkled device in comparison to the flat devices is attributed to the following reasons: (a) the wrinkles induce a reduction in the bandgap in MoS_2, which provides a wider range of band-transitions for the incident photons; thus enabling a wider energy-range for light absorption;(*17*) (b) the reduced optical bandgap profile generates exciton funneling (a distortion in the energy band, enabling photo-induced excitons to move to lower bandgap region(*203*)) for photo-generated excitons with lower energy in the wrinkled MoS_2 region, as shown in photoluminescence mapping; and (c) the potential in the depletion regions enables photo-induced excitons to be separated and reduces the recombination probability (Figure 46). The fraction of unrecombined photo-generated electrons in wrinkled samples is much larger than that in the flat MoS_2, which leads to more efficient drift of photo-generated electrons. Therefore, much higher photoresponsivity was exhibited by wrinkled MoS_2.

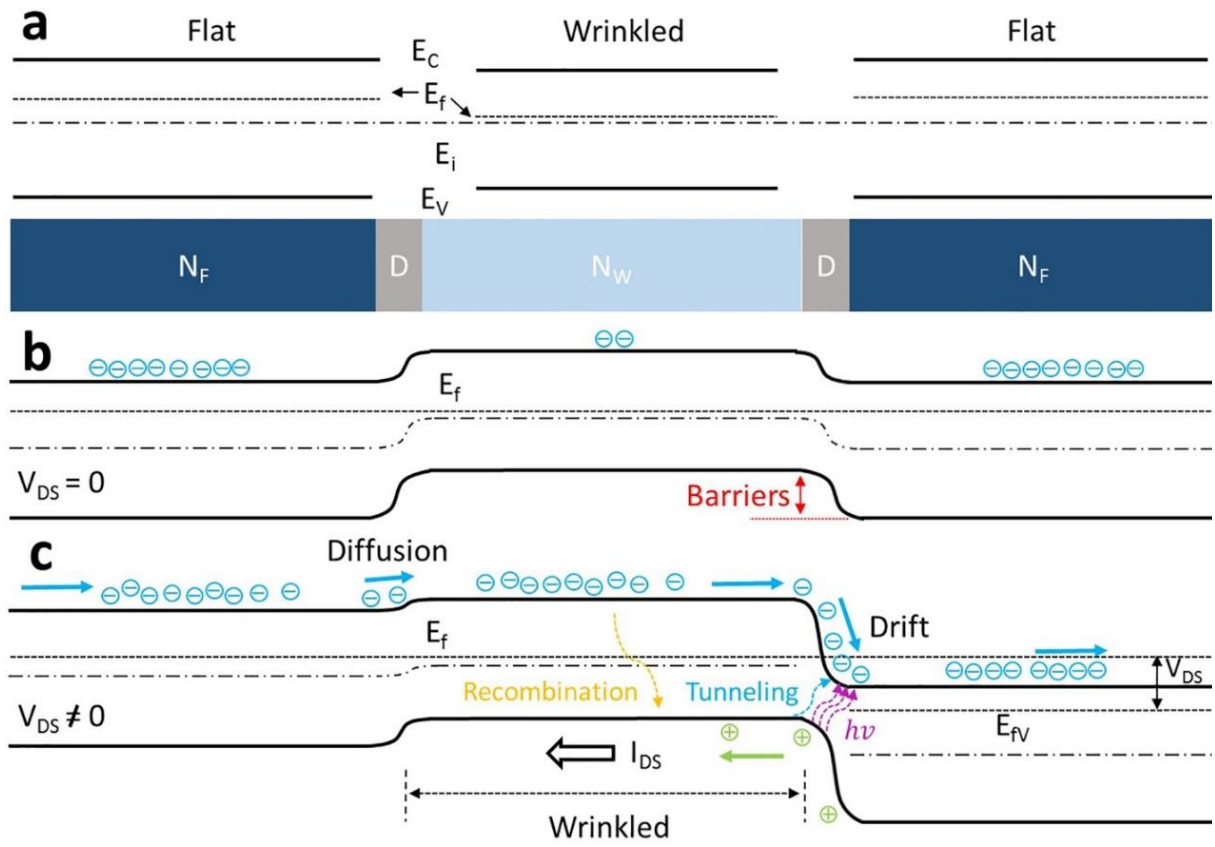

Figure 46. Energy band diagrams of wrinkled MoS_2 devices. (a) Individual flat and wrinkled MoS_2; (b) device at no bias; and (c) wrinkled MoS_2 device under bias. Blue and green spheres are electrons and holes, respectively. And the filled arrows are the directions of carriers' movements direction and the unfilled arrow represents the current directions (I_{DS}).

5. SUMMARY

This dissertation providers detailed understanding of the wrinkles formation mechanism in thin two-dimensional nanomaterials and explains the effect of structure and strain engineering on the properties of graphene and MoS_2. First, a hierarchical wrinkle patterns formation mechanism on thin metal film deposited on a liquid meniscus edge and bulk was described by incorporating surface energy within the typical bending, stretching, thermal, and gravitational energy considerations. The thermal contraction of liquid meniscus postdeposition caused up to five hierarchical transitions in wrinkle wavelength. We modified the wrinklon theory by defining a hierarchical length $L = L(C) + L(T)$ to model the global wrinkle pattern with constant wavelength region ($L(C)$). Interestingly, the size of the self-similar multiscale structure as well as the penetration of surface energy can be estimated by the evolution of amplitude of wrinkles ($L(\lambda) \sim A(\lambda)$). The theory also shows a model for hierarchical length as a function of wavelength of wrinkles. And, wrinkled MoS_2 can be used to determine the adhesion energy between MoS_2 and rigid substrates (SiO_2 and Si_3N_4). The adhesion energies of 0.170 ± 0.033 J m^{-2} for MoS_2 on SiO_2 and 0.252 ± 0.041 J m^{-2} for MoS_2 on Si_3N_4 were obtained. The different values on these two substrates are attributed to the roughness of the surfaces. This method is suitable for wrinkles with $A/t \geq 3.4$. The adhesion method and results shown here may benefit studies on the surface interactions, 2DN interfacial properties, and thin-film device fabrication. Further, we show that the bacterium scaffold can be employed to achieve selectively patterned, aligned, confined, and electrically anisotropic graphene wrinkles. This is realized by flap-valve operation of graphene, which functions as a mass-transfer diode.

The longitudinal (high-texture aspect ratio) graphenic wrinkles with ultrasmall wavelength (32–34 nm) controllably aligned between electrodes exhibit an anisotropic barrier (ΔE = 1.69 meV). This study can be extrapolated for formation of confined wrinkles on other 2DNs and for reduced wrinkle wavelengths *via* bacterial cells with a higher Young's modulus (or *via* hygroscopic polymer patterns). The work could also evolve advances in cytoelectronics and 2D electronic circuitry with controlled wrinkle placement. Wrinkles in MoS_2 thin films on SiO_2 produced by mechanical exfoliation exhibit uniaxial strains and doping variation, which can lead to phonon softening, energy band deformations (exciton funneling), mobility improvement and built-in potentials to separate excitons for enhanced photo-responsivity. Wrinkled MoS_2 FET studies at cryogenic temperatures show a larger barrier (ΔE_A=106.6 meV) in the transverse direction of the wrinkle compared to the flat MoS_2 device. With this work, we reveal that wrinkling semiconducting 2DNMs can enable control of the transport properties and electronic band-structure in 2DNMs and potentially their heterostructures. Such capability can lead to engineering the optical transitions and electronic transport mechanisms in these flexible structures, which might hold promise in future electronics, optoelectronics, and sensors applications.

6. REFERENCES

1. K. S. Novoselov *et al.*, Electric Field Effect in Atomically Thin Carbon Films. *Science* **306**, 666-669 (2004).
2. K. S. Novoselov *et al.*, Two-dimensional atomic crystals. *Proceedings of the National Academy of Sciences of the United States of America* **102**, 10451-10453 (2005).
3. K. I. Bolotin *et al.*, Ultrahigh electron mobility in suspended graphene. *Solid State Communications* **146**, 351-355 (2008).
4. R. R. Nair *et al.*, Fine Structure Constant Defines Visual Transparency of Graphene. *Science* **320**, 1308 (2008).
5. A. A. Balandin *et al.*, Superior Thermal Conductivity of Single-Layer Graphene. *Nano Letters* **8**, 902-907 (2008).
6. C. Lee, X. D. Wei, J. W. Kysar, J. Hone, Measurement of the elastic properties and intrinsic strength of monolayer graphene. *Science* **321**, 385-388 (2008).
7. A. K. Geim, K. S. Novoselov, The rise of graphene. *Nat Mater* **6**, 183-191 (2007).
8. A. Reina *et al.*, Large Area, Few-Layer Graphene Films on Arbitrary Substrates by Chemical Vapor Deposition. *Nano Letters* **9**, 30-35 (2008).
9. X. Li *et al.*, Large-Area Synthesis of High-Quality and Uniform Graphene Films on Copper Foils. *Science* **324**, 1312-1314 (2009).
10. K. S. Kim *et al.*, Large-scale pattern growth of graphene films for stretchable transparent electrodes. *Nature* **457**, 706-710 (2009).

11. C. Berger *et al.*, Electronic Confinement and Coherence in Patterned Epitaxial Graphene. *Science* **312**, 1191-1196 (2006).

12. H. C. Schniepp *et al.*, Functionalized Single Graphene Sheets Derived from Splitting Graphite Oxide. *The Journal of Physical Chemistry B* **110**, 8535-8539 (2006).

13. P. W. Sutter, P. M. Albrecht, E. A. Sutter, Graphene growth on epitaxial Ru thin films on sapphire. *Applied Physics Letters* **97**, - (2010).

14. C. Mattevi, H. Kim, M. Chhowalla, A review of chemical vapour deposition of graphene on copper. *Journal of Materials Chemistry* **21**, 3324-3334 (2011).

15. J. A. Wilson, A. D. Yoffe, The transition metal dichalcogenides discussion and interpretation of the observed optical, electrical and structural properties. *Advances in Physics* **18**, 193-335 (1969).

16. A. D. Yoffe, Low-dimensional systems: quantum size effects and electronic properties of semiconductor microcrystallites (zero-dimensional systems) and some quasi-two-dimensional systems. *Advances in Physics* **42**, 173-262 (1993).

17. Q. H. Wang, K. Kalantar-Zadeh, A. Kis, J. N. Coleman, M. S. Strano, Electronics and optoelectronics of two-dimensional transition metal dichalcogenides. *Nature Nanotechnology* **7**, 699-712 (2012).

18. J. Huang, B. Davidovitch, C. D. Santangelo, T. P. Russell, N. Menon, Smooth Cascade of Wrinkles at the Edge of a Floating Elastic Film. *Physical Review Letters* **105**, 038302 (2010).

19. J. Huang *et al.*, Capillary Wrinkling of Floating Thin Polymer Films. *Science* **317**, 650-653 (2007).

20. H. King, R. D. Schroll, B. Davidovitch, N. Menon, Elastic sheet on a liquid drop reveals wrinkling and crumpling as distinct symmetry-breaking instabilities. *Proceedings of the National Academy of Sciences* **109**, 9716-9720 (2012).

21. Y. Ni, D. Yang, L. He, Spontaneous wrinkle branching by gradient stiffness. *Physical Review E* **86**, 031604 (2012).

22. L. Pocivavsek *et al.*, Stress and Fold Localization in Thin Elastic Membranes. *Science* **320**, 912-916 (2008).

23. R. D. Schroll, E. Katifori, B. Davidovitch, Elastic Building Blocks for Confined Sheets. *Physical Review Letters* **106**, 074301 (2011).

24. K. B. Toga, J. Huang, K. Cunningham, T. P. Russell, N. Menon, A drop on a floating sheet: boundary conditions, topography and formation of wrinkles. *Soft Matter* **9**, 8289-8296 (2013).

25. S. Deng, V. Berry, Wrinkled, rippled and crumpled graphene: an overview of formation mechanism, electronic properties, and applications. *Mater Today* **19**, 197-212 (2016).

26. N. Bowden, S. Brittain, A. G. Evans, J. W. Hutchinson, G. M. Whitesides, Spontaneous formation of ordered structures in thin films of metals supported on an elastomeric polymer. *Nature* **393**, 146-149 (1998).

27. X. Chen, J. W. Hutchinson, A family of herringbone patterns in thin films. *Scripta Materialia* **50**, 797-801 (2004).

28. X. Chen, J. W. Hutchinson, Herringbone Buckling Patterns of Compressed Thin Films on Compliant Substrates. *Journal of Applied Mechanics* **71**, 597-603 (2004).

29. J. Genzer, J. Groenewold, Soft matter with hard skin: From skin wrinkles to templating and material characterization. *Soft Matter* **2**, 310-323 (2006).

30. M. Pineirua, N. Tanaka, B. Roman, J. Bico, Capillary buckling of a floating annulus. *Soft Matter* **9**, 10985-10992 (2013).

31. R. D. Schroll *et al.*, Capillary Deformations of Bendable Films. *Physical Review Letters* **111**, 014301 (2013).

32. C. Lee, X. Wei, J. W. Kysar, J. Hone, Measurement of the Elastic Properties and Intrinsic Strength of Monolayer Graphene. *Science* **321**, 385-388 (2008).

33. J. S. Cameron, D. S. Ashley, J. S. Andrew, G. S. Joseph, T. G. Christopher, Accurate thickness measurement of graphene. *Nanotechnology* **27**, 125704 (2016).

34. P. Nemes-Incze, Z. Osváth, K. Kamarás, L. P. Biró, Anomalies in thickness measurements of graphene and few layer graphite crystals by tapping mode atomic force microscopy. *Carbon* **46**, 1435-1442 (2008).

35. S. Deng *et al.*, Confined, Oriented, and Electrically Anisotropic Graphene Wrinkles on Bacteria. *ACS Nano* **10**, 8403-8412 (2016).

36. J.-W. Jiang, T. Chang, X. Guo, H. S. Park, Intrinsic Negative Poisson's Ratio for Single-Layer Graphene. *Nano Letters* **16**, 5286-5290 (2016).

37. A. Fasolino, J. H. Los, M. I. Katsnelson, Intrinsic ripples in graphene. *Nat Mater* **6**, 858-861 (2007).

38. J. C. Meyer *et al.*, The structure of suspended graphene sheets. *Nature* **446**, 60-63 (2007).

39. V. B. Shenoy, C. D. Reddy, A. Ramasubramaniam, Y. W. Zhang, Edge-Stress-Induced Warping of Graphene Sheets and Nanoribbons. *Physical Review Letters* **101**, 245501 (2008).

40. D. B. Zhang, E. Akatyeva, T. Dumitrică, Bending Ultrathin Graphene at the Margins of Continuum Mechanics. *Physical Review Letters* **106**, 255503 (2011).

41. F. Banhart, J. Kotakoski, A. V. Krasheninnikov, Structural Defects in Graphene. *ACS Nano* **5**, 26-41 (2011).

42. W. Bao *et al.*, Controlled ripple texturing of suspended graphene and ultrathin graphite membranes. *Nat Nano* **4**, 562-566 (2009).

43. L. Meng *et al.*, Hierarchy of graphene wrinkles induced by thermal strain engineering. *Applied Physics Letters* **103**, - (2013).

44. V. E. Calado, G. F. Schneider, A. M. M. G. Theulings, C. Dekker, L. M. K. Vandersypen, Formation and control of wrinkles in graphene by the wedging transfer method. *Applied Physics Letters* **101**, (2012).

45. J. Zang *et al.*, Multifunctionality and control of the crumpling and unfolding of large-area graphene. *Nat Mater* **12**, 321-325 (2013).

46. N. Mohanty, V. Berry, Graphene-Based Single-Bacterium Resolution Biodevice and DNA Transistor: Interfacing Graphene Derivatives with Nanoscale and Microscale Biocomponents. *Nano Letters* **8**, 4469-4476 (2008).

47. N. Liu *et al.*, The origin of wrinkles on transferred graphene. *Nano Res.* **4**, 996-1004 (2011).

48. W. Yan *et al.*, Strain and curvature induced evolution of electronic band structures in twisted graphene bilayer. *Nat Commun* **4**, (2013).

49. V. M. Pereira, A. H. Castro Neto, H. Y. Liang, L. Mahadevan, Geometry, Mechanics, and Electronics of Singular Structures and Wrinkles in Graphene. *Physical Review Letters* **105**, 156603 (2010).

50. K.-K. Bai *et al.*, Creating One-Dimensional Nanoscale Periodic Ripples in a Continuous Mosaic Graphene Monolayer. *Physical Review Letters* **113**, 086102 (2014).

51. H. Lim, J. Jung, R. S. Ruoff, Y. Kim, Structurally driven one-dimensional electron confinement in sub-5-nm graphene nanowrinkles. *Nat Commun* **6**, (2015).

52. L. Tapaszto *et al.*, Breakdown of continuum mechanics for nanometre-wavelength rippling of graphene. *Nat Phys* **8**, 739-742 (2012).

53. W. Zhu *et al.*, Structure and Electronic Transport in Graphene Wrinkles. *Nano Letters* **12**, 3431-3436 (2012).

54. A. H. Castro Neto, F. Guinea, N. M. R. Peres, K. S. Novoselov, A. K. Geim, The electronic properties of graphene. *Reviews of Modern Physics* **81**, 109-162 (2009).

55. W. H. Duan, K. Gong, Q. Wang, Controlling the formation of wrinkles in a single layer graphene sheet subjected to in-plane shear. *Carbon* **49**, 3107-3112 (2011).

56. D. Jariwala, V. K. Sangwan, L. J. Lauhon, T. J. Marks, M. C. Hersam, Emerging Device Applications for Semiconducting Two-Dimensional Transition Metal Dichalcogenides. *ACS Nano* **8**, 1102-1120 (2014).

57. B. Radisavljevic, A. Radenovic, J. Brivio, V. Giacometti, A. Kis, Single-layer MoS2 transistors. *Nature Nanotechnology* **6**, 147-150 (2011).

58. M. Chhowalla *et al.*, The chemistry of two-dimensional layered transition metal dichalcogenide nanosheets. *Nature Chemistry* **5**, 263-275 (2013).

59. S. Bertolazzi, J. Brivio, A. Kis, Stretching and Breaking of Ultrathin MoS2. *ACS Nano* **5**, 9703-9709 (2011).

60. B. Sipos *et al.*, From Mott state to superconductivity in 1T-TaS2. *Nat Mater* **7**, 960-965 (2008).

61. A. Kuc, N. Zibouche, T. Heine, Influence of quantum confinement on the electronic structure of the transition metal sulfide TS2. *Physical Review B* **83**, 245213 (2011).

62. R. A. Gordon, D. Yang, E. D. Crozier, D. T. Jiang, R. F. Frindt, Structures of exfoliated single layers of WS2,MoS2,MoSe2 in aqueous suspension. *Physical Review B* **65**, 125407 (2002).

63. T. Cao *et al.*, Valley-selective circular dichroism of monolayer molybdenum disulphide. *Nat Commun* **3**, 887 (2012).

64. H. Zeng, J. Dai, W. Yao, D. Xiao, X. Cui, Valley polarization in MoS2 monolayers by optical pumping. *Nature Nanotechnology* **7**, 490-493 (2012).

65. K. F. Mak, K. He, J. Shan, T. F. Heinz, Control of valley polarization in monolayer MoS2 by optical helicity. *Nat Nano* **7**, 494-498 (2012).

66. D. Lloyd *et al.*, Band Gap Engineering with Ultralarge Biaxial Strains in Suspended Monolayer MoS2. *Nano Letters*, (2016).

67. A. Castellanos-Gomez *et al.*, Local Strain Engineering in Atomically Thin MoS2. *Nano Letters* **13**, 5361-5366 (2013).

68. C. Rice *et al.*, Raman-scattering measurements and first-principles calculations of strain-induced phonon shifts in monolayer MoS2. *Physical Review B* **87**, 081307 (2013).

69. Q. Peng, S. De, Outstanding mechanical properties of monolayer MoS2 and its application in elastic energy storage. *Phys Chem Chem Phys* **15**, 19427-19437 (2013).

70. K. Liu *et al.*, Elastic Properties of Chemical-Vapor-Deposited Monolayer MoS2, WS2, and Their Bilayer Heterostructures. *Nano Letters* **14**, 5097-5103 (2014).

71. J. Li, N. V. Medhekar, V. B. Shenoy, Bonding Charge Density and Ultimate Strength of Monolayer Transition Metal Dichalcogenides. *The Journal of Physical Chemistry C* **117**, 15842-15848 (2013).

72. J. Kang, S. Tongay, J. Zhou, J. Li, J. Wu, Band offsets and heterostructures of two-dimensional semiconductors. *Applied Physics Letters* **102**, 012111 (2013).

73. L. H. Li, Y. Chen, Atomically Thin Boron Nitride: Unique Properties and Applications. *Advanced Functional Materials* **26**, 2594-2608 (2016).

74. L. Zhang *et al.*, Structural and Electronic Properties of Germanene on MoS2. *Physical Review Letters* **116**, 256804 (2016).

75. F. Zeng, W.-B. Zhang, B.-Y. Tang, Electronic structures and elastic properties of monolayer and bilayer transition metal dichalcogenides MX 2 (M = Mo, W; X = O, S, Se, Te): A comparative first-principles study. *Chinese Phys B* **24**, 097103 (2015).

76. S. Manzeli, A. Allain, A. Ghadimi, A. Kis, Piezoresistivity and Strain-induced Band Gap Tuning in Atomically Thin MoS2. *Nano Letters* **15**, 5330-5335 (2015).

77. Y. Yang *et al.*, Brittle Fracture of 2D MoSe2. *Advanced Materials* **29**, 1604201-n/a (2017).

78. V. Iberi *et al.*, Nanoforging Single Layer MoSe2 Through Defect Engineering with Focused Helium Ion Beams. *Scientific Reports* **6**, 30481 (2016).

79. R. Zhang, V. Koutsos, R. Cheung, Elastic properties of suspended multilayer WSe2. *Applied Physics Letters* **108**, 042104 (2016).

80. W. Liu *et al.*, Role of Metal Contacts in Designing High-Performance Monolayer n-Type WSe2 Field Effect Transistors. *Nano Letters* **13**, 1983-1990 (2013).

81. H. Li *et al.*, Mechanical Exfoliation and Characterization of Single- and Few-Layer Nanosheets of WSe2, TaS2, and TaSe2. *Small* **9**, 1974-1981 (2013).

82. J. Yin, Z. Cao, C. Li, I. Sheinman, X. Chen, Stress-driven buckling patterns in spheroidal core/shell structures. *Proceedings of the National Academy of Sciences* **105**, 19132-19135 (2008).

83. H. Vandeparre *et al.*, Wrinkling Hierarchy in Constrained Thin Sheets from Suspended Graphene to Curtains. *Physical Review Letters* **106**, 224301 (2011).

84. H. Jiang *et al.*, Finite deformation mechanics in buckled thin films on compliant supports. *Proceedings of the National Academy of Sciences of the United States of America* **104**, 15607-15612 (2007).

85. S.-J. Yu *et al.*, Spontaneous formation of hierarchical wrinkles in Cr films deposited on silicone oil drops with constrained edges. *Physical Review E* **88**, 042401 (2013).

86. K. Zhang *et al.*, Manganese Doping of Monolayer MoS2: The Substrate Is Critical. *Nano Letters* **15**, 6586-6591 (2015).

87. S. Behura, P. Nguyen, S. Che, R. Debbarma, V. Berry, Large-Area, Transfer-Free, Oxide-Assisted Synthesis of Hexagonal Boron Nitride Films and Their Heterostructures with MoS2 and WS2. *Journal of the American Chemical Society* **137**, 13060-13065 (2015).

88. L. Britnell *et al.*, Field-Effect Tunneling Transistor Based on Vertical Graphene Heterostructures. *Science* **335**, 947 (2012).

89. T. R. Hull, J. S. Colligon, A. E. Hill, Measurement of thin film adhesion. *Vacuum* **37**, 327-330 (1987).

90. M. J. Cordill, D. F. Bahr, N. R. Moody, W. W. Gerberich, Recent developments in thin film adhesion measurement. *IEEE Transactions on Device and Materials Reliability* **4**, 163-168 (2004).

91. D. S. Rickerby, A review of the methods for the measurement of coating-substrate adhesion. *Surface and Coatings Technology* **36**, 541-557 (1988).

92. M. D. Thouless, An analysis of spalling in the microscratch test. *Engineering Fracture Mechanics* **61**, 75-81 (1998).

93. R. H. Dauskardt, M. Lane, Q. Ma, N. Krishna, Adhesion and debonding of multi-layer thin film structures. *Engineering Fracture Mechanics* **61**, 141-162 (1998).

94. A. Bagchi, G. E. Lucas, Z. Suo, A. G. Evans, A new procedure for measuring the decohesion energy for thin ductile films on substrates. *Journal of Materials Research* **9**, 1734-1741 (1994).

95. M. P. De Boer, W. W. Gerberich, Microwedge indentation of the thin film fine line—I. Mechanics. *Acta Materialia* **44**, 3169-3175 (1996).

96. S. P. Koenig, N. G. Boddeti, M. L. Dunn, J. S. Bunch, Ultrastrong adhesion of graphene membranes. *Nat Nano* **6**, 543-546 (2011).

97. Z. Zong, C. L. Chen, M. R. Dokmeci, K. T. Wan, Direct measurement of graphene adhesion on silicon surface by intercalation of nanoparticles. *Journal of Applied Physics* **107**, (2010).

98. T. Yoon *et al.*, Direct Measurement of Adhesion Energy of Monolayer Graphene As-Grown on Copper and Its Application to Renewable Transfer Process. *Nano Letters* **12**, 1448-1452 (2012).

99. D. Lloyd *et al.*, Adhesion, Stiffness, and Instability in Atomically Thin MoS2 Bubbles. *Nano Letters*, (2017).

100. Z. Cao, L. Tao, D. Akinwande, R. Huang, K. M. Liechti, Mixed-Mode Interactions Between Graphene and Substrates by Blister Tests. *Journal of Applied Mechanics* **82**, 081008-081008 (2015).

101. Z. Cao, L. Tao, D. Akinwande, R. Huang, K. M. Liechti, Mixed-mode traction-separation relations between graphene and copper by blister tests. *International Journal of Solids and Structures* **84**, 147-159 (2016).

102. S. Kumar, D. Parks, K. Kamrin, Mechanistic Origin of the Ultrastrong Adhesion between Graphene and a-SiO2: Beyond van der Waals. *ACS Nano* **10**, 6552-6562 (2016).

103. W. Gao, K. M. Liechti, R. Huang, Wet adhesion of graphene. *Extreme Mechanics Letters* **3**, 130-140 (2015).

104. S. Yang *et al.*, Tuning the Optical, Magnetic, and Electrical Properties of ReSe2 by Nanoscale Strain Engineering. *Nano Letters* **15**, 1660-1666 (2015).

105. B. Wang, S. Wang, Adhesion-governed buckling of thin-film electronics on soft tissues. *Theoretical and Applied Mechanics Letters* **6**, 6-10 (2016).

106. A. P. M. Barboza *et al.*, Dynamic Negative Compressibility of Few-Layer Graphene, h-BN, and MoS2. *Nano Letters* **12**, 2313-2317 (2012).

107. P. Xu *et al.*, Unusual ultra-low-frequency fluctuations in freestanding graphene. *Nat Commun* **5**, (2014).

108. R. E. Peierls, Quelques proprietes typiques des corpses solides. *Ann. I. H. Poincare* **5**, 177-222 (1935).

109. L. D. Landau, Zur Theorie der phasenumwandlungen II. *Phys. Z. Sowjetunion* **11**, 26-35 (1937).

110. A. S. Barnard, I. K. Snook, Ripple induced changes in the wavefunction of graphene: an example of a fundamental symmetry breaking. *Nanoscale* **4**, 1167-1170 (2012).

111. K. Eun-Ah, A. H. C. Neto, Graphene as an electronic membrane. *EPL (Europhysics Letters)* **84**, 57007 (2008).

112. S. Jung *et al.*, Evolution of microscopic localization in graphene in a magnetic field from scattering resonances to quantum dots. *Nat Phys* **7**, 245-251 (2011).

113. A. G. Kvashnin, P. B. Sorokin, B. I. Yakobson, Flexoelectricity in Carbon Nanostructures: Nanotubes, Fullerenes, and Nanocones. *The Journal of Physical Chemistry Letters* **6**, 2740-2744 (2015).

114. Q. H. Wang *et al.*, Understanding and controlling the substrate effect on graphene electron-transfer chemistry via reactivity imprint lithography. *Nat Chem* **4**, 724-732 (2012).

115. D. R. Nelson, L. Peliti, Fluctuations in membranes with crystalline and hexatic order. *J. Phys. France* **48**, 1085-1092 (1987).

116. N. D. Mermin, Crystalline Order in Two Dimensions. *Physical Review* **176**, 250-254 (1968).

117. Y. Kantor, M. Kardar, D. R. Nelson, Statistical Mechanics of Tethered Surfaces. *Physical Review Letters* **57**, 791-794 (1986).

118. H. S. Seung, D. R. Nelson, Defects in flexible membranes with crystalline order. *Physical Review A* **38**, 1005-1018 (1988).

119. A. N. Obraztsov, E. A. Obraztsova, A. V. Tyurnina, A. A. Zolotukhin, Chemical vapor deposition of thin graphite films of nanometer thickness. *Carbon* **45**, 2017-2021 (2007).

120. J.-S. Yu *et al.*, Structural analysis of graphene synthesized by chemical vapor deposition on copper foil using nematic liquid crystal texture. *Carbon* **76**, 113-122 (2014).

121. S. J. Chae *et al.*, Synthesis of Large-Area Graphene Layers on Poly-Nickel Substrate by Chemical Vapor Deposition: Wrinkle Formation. *Advanced Materials* **21**, 2328-2333 (2009).

122. C. Vecchio *et al.*, Nanoscale structural characterization of epitaxial graphene grown on off-axis 4H-SiC (0001). *Nanoscale Research Letters* **6**, 269 (2011).

123. L. B. Biedermann, M. L. Bolen, M. A. Capano, D. Zemlyanov, R. G. Reifenberger, Insights into few-layer epitaxial graphene growth on $4H\text{-SiC}(000\overline{1})$ substrates from STM studies. *Physical Review B* **79**, 125411 (2009).

124. V. E. Calado, G. F. Schneider, A. M. M. G. Theulings, C. Dekker, L. M. K. Vandersypen, Formation and control of wrinkles in graphene by the wedging transfer method. *Applied Physics Letters* **101**, - (2012).

125. M. Lanza *et al.*, Tuning graphene morphology by substrate towards wrinkle-free devices: Experiment and simulation. *Journal of Applied Physics* **113**, - (2013).

126. N. Levy *et al.*, Strain-Induced Pseudo–Magnetic Fields Greater Than 300 Tesla in Graphene Nanobubbles. *Science* **329**, 544-547 (2010).

127. J.-K. Lee *et al.*, Modification of Electrical Properties of Graphene by Substrate-Induced Nanomodulation. *Nano Letters* **13**, 3494-3500 (2013).

128. M. I. Katsnelson, A. K. Geim, *Electron scattering on microscopic corrugations in graphene*. (2008), vol. 366, pp. 195-204.

129. L. Meng *et al.*, Strain-induced one-dimensional Landau level quantization in corrugated graphene. *Physical Review B* **87**, 205405 (2013).

130. J. Hu, Z. Kang, F. Li, X. Huang, Graphene with three-dimensional architecture for high performance supercapacitor. *Carbon* **67**, 221-229 (2014).

131. Y. Wang *et al.*, Super-Elastic Graphene Ripples for Flexible Strain Sensors. *ACS Nano* **5**, 3645-3650 (2011).

132. M. Schriver *et al.*, Graphene as a Long-Term Metal Oxidation Barrier: Worse Than Nothing. *ACS Nano* **7**, 5763-5768 (2013).

133. T. Chen, Y. Xue, A. K. Roy, L. Dai, Transparent and Stretchable High-Performance Supercapacitors Based on Wrinkled Graphene Electrodes. *ACS Nano* **8**, 1039-1046 (2013).

134. D. W. Boukhvalov, M. I. Katsnelson, Enhancement of Chemical Activity in Corrugated Graphene. *The Journal of Physical Chemistry C* **113**, 14176-14178 (2009).

135. S. Cranford, D. Sen, M. J. Buehler, Meso-origami: Folding multilayer graphene sheets. *Applied Physics Letters* **95**, - (2009).

136. J. Martin *et al.*, Observation of electron-hole puddles in graphene using a scanning single-electron transistor. *Nat Phys* **4**, 144-148 (2008).

137. P. Partovi-Azar, N. Nafari, M. R. R. Tabar, Interplay between geometrical structure and electronic properties in rippled free-standing graphene. *Physical Review B* **83**, 165434 (2011).

138. X. Zhou *et al.*, Tin Dioxide@Carbon Core–Shell Nanoarchitectures Anchored on Wrinkled Graphene for Ultrafast and Stable Lithium Storage. *ACS Applied Materials & Interfaces* **6**, 7434-7443 (2014).

139. RamanathanT *et al.*, Functionalized graphene sheets for polymer nanocomposites. *Nat Nano* **3**, 327-331 (2008).

140. S. Das Sarma, S. Adam, E. H. Hwang, E. Rossi, Electronic transport in two-dimensional graphene. *Reviews of Modern Physics* **83**, 407-470 (2011).

141. M. I. Katsnelson, A. K. Geim, Electron scattering on microscopic corrugations in graphene. *Philosophical Transactions of the Royal Society A: Mathematical, Physical and Engineering Sciences* **366**, 195-204 (2008).

142. K. Xu, P. Cao, J. R. Heath, Scanning Tunneling Microscopy Characterization of the Electrical Properties of Wrinkles in Exfoliated Graphene Monolayers. *Nano Letters* **9**, 4446-4451 (2009).

143. S. V. Morozov *et al.*, Strong Suppression of Weak Localization in Graphene. *Physical Review Letters* **97**, 016801 (2006).

144. J. Park, G. He, R. M. Feenstra, A.-P. Li, Atomic-Scale Mapping of Thermoelectric Power on Graphene: Role of Defects and Boundaries. *Nano Letters* **13**, 3269-3273 (2013).

145. A. L. Vázquez de Parga *et al.*, Periodically Rippled Graphene: Growth and Spatially Resolved Electronic Structure. *Physical Review Letters* **100**, 056807 (2008).

146. S. Martin, W. B. Piet, Quantum corrections to transport in graphene: a trajectory-based semiclassical analysis. *New Journal of Physics* **16**, 073015 (2014).

147. P. A. Lee, T. V. Ramakrishnan, Disordered electronic systems. *Reviews of Modern Physics* **57**, 287-337 (1985).

148. B. L. Altshuler, A. G. Aronov, P. A. Lee, Interaction Effects in Disordered Fermi Systems in Two Dimensions. *Physical Review Letters* **44**, 1288-1291 (1980).

149. A. Deshpande, W. Bao, F. Miao, C. N. Lau, B. J. LeRoy, Spatially resolved spectroscopy of monolayer graphene on SiO2. *Physical Review B* **79**, 205411 (2009).

150. M. L. Teague *et al.*, Evidence for Strain-Induced Local Conductance Modulations in Single-Layer Graphene on SiO2. *Nano Letters* **9**, 2542-2546 (2009).

151. Y. Zhang, V. W. Brar, C. Girit, A. Zettl, M. F. Crommie, Origin of spatial charge inhomogeneity in graphene. *Nat Phys* **5**, 722-726 (2009).

152. A. T. Costa, M. S. Ferreira, H. Toby, S. D. Georg, A. H. C. Neto, Origami-based spintronics in graphene. *EPL (Europhysics Letters)* **104**, 47001 (2013).

153. G.-X. Ni *et al.*, Quasi-Periodic Nanoripples in Graphene Grown by Chemical Vapor Deposition and Its Impact on Charge Transport. *ACS Nano* **6**, 1158-1164 (2012).

154. C. Wang, Y. Liu, L. Li, H. Tan, Anisotropic thermal conductivity of graphene wrinkles. *Nanoscale* **6**, 5703-5707 (2014).

155. J. R. Miller, R. A. Outlaw, B. C. Holloway, Graphene Double-Layer Capacitor with ac Line-Filtering Performance. *Science* **329**, 1637-1639 (2010).

156. J. Zang, C. Cao, Y. Feng, J. Liu, X. Zhao, Stretchable and High-Performance Supercapacitors with Crumpled Graphene Papers. *Sci. Rep.* **4**, (2014).

157. Q. Li *et al.*, Superior flexibility of a wrinkled carbon shell under electrochemical cycling. *J Mater Chem A* **2**, 4192-4197 (2014).

158. S. Zhu, T. Li, Wrinkling Instability of Graphene on Substrate-Supported Nanoparticles. *Journal of Applied Mechanics* **81**, 061008-061008 (2014).

159. G. Fisichella, S. Di Franco, F. Roccaforte, S. Ravesi, F. Giannazzo, Microscopic mechanisms of graphene electrolytic delamination from metal substrates. *Applied Physics Letters* **104**, - (2014).

160. Z. Pan, N. Liu, L. Fu, Z. Liu, Wrinkle Engineering: A New Approach to Massive Graphene Nanoribbon Arrays. *Journal of the American Chemical Society* **133**, 17578-17581 (2011).

161. G. Eda *et al.*, Photoluminescence from Chemically Exfoliated MoS2. *Nano Letters* **11**, 5111-5116 (2011).

162. G. Cunningham *et al.*, Solvent Exfoliation of Transition Metal Dichalcogenides: Dispersibility of Exfoliated Nanosheets Varies Only Weakly between Compounds. *Acs Nano* **6**, 3468-3480 (2012).

163. G. Eda *et al.*, Coherent Atomic and Electronic Heterostructures of Single-Layer MoS2. *Acs Nano* **6**, 7311-7317 (2012).

164. P. May, U. Khan, J. M. Hughes, J. N. Coleman, Role of Solubility Parameters in Understanding the Steric Stabilization of Exfoliated Two-Dimensional Nanosheets by Adsorbed Polymers. *J Phys Chem C* **116**, 11393-11400 (2012).

165. R. J. Smith *et al.*, Large-Scale Exfoliation of Inorganic Layered Compounds in Aqueous Surfactant Solutions. *Advanced Materials* **23**, 3944-+ (2011).

166. Z. Y. Zeng *et al.*, An Effective Method for the Fabrication of Few-Layer-Thick Inorganic Nanosheets. *Angewandte Chemie-International Edition* **51**, 9052-9056 (2012).

167. Z. Y. Zeng *et al.*, Single-Layer Semiconducting Nanosheets: High-Yield Preparation and Device Fabrication. *Angewandte Chemie-International Edition* **50**, 11093-11097 (2011).

168. J. N. Coleman *et al.*, Two-Dimensional Nanosheets Produced by Liquid Exfoliation of Layered Materials. *Science* **331**, 568-571 (2011).

169. P. Joensen, R. F. Frindt, S. R. Morrison, Single-layer MoS2. *Materials Research Bulletin* **21**, 457-461 (1986).

170. K.-K. Liu *et al.*, Growth of Large-Area and Highly Crystalline MoS2 Thin Layers on Insulating Substrates. *Nano Letters* **12**, 1538-1544 (2012).

171. Y. Zhan, Z. Liu, S. Najmaei, P. M. Ajayan, J. Lou, Large-Area Vapor-Phase Growth and Characterization of MoS2 Atomic Layers on a SiO2 Substrate. *Small* **8**, 966-971 (2012).

172. Y.-H. Lee *et al.*, Synthesis of Large-Area MoS2 Atomic Layers with Chemical Vapor Deposition. *Advanced Materials* **24**, 2320-2325 (2012).

173. Y.-C. Lin *et al.*, Wafer-scale MoS2 thin layers prepared by MoO3 sulfurization. *Nanoscale* **4**, 6637-6641 (2012).

174. Y. Yoon, K. Ganapathi, S. Salahuddin, How Good Can Monolayer MoS2 Transistors Be? *Nano Letters* **11**, 3768-3773 (2011).

175. A. Castellanos-Gomez *et al.*, Elastic Properties of Freely Suspended MoS2 Nanosheets. *Advanced Materials* **24**, 772-775 (2012).

176. C. Lee *et al.*, Anomalous Lattice Vibrations of Single- and Few-Layer MoS2. *Acs Nano* **4**, 2695-2700 (2010).

177. A. Molina-Sánchez, L. Wirtz, Phonons in single-layer and few-layer MoS2 and WS2. *Physical Review B* **84**, 155413 (2011).

178. K. F. Mak, C. Lee, J. Hone, J. Shan, T. F. Heinz, Atomically Thin MoS2: A New Direct-Gap Semiconductor. *Physical Review Letters* **105**, (2010).

179. A. Splendiani *et al.*, Emerging Photoluminescence in Monolayer MoS2. *Nano Letters* **10**, 1271-1275 (2010).

180. A. Carladous *et al.*, Light emission from spectral analysis of Au/MoS2 nanocontacts stimulated by scanning tunneling microscopy. *Physical Review B* **66**, 045401 (2002).

181. R. Coehoorn, C. Haas, R. A. de Groot, Electronic structure of MoSe2, MoS2, and WSe2. II. The nature of the optical band gaps. *Physical Review B* **35**, 6203-6206 (1987).

182. A. Polman, H. A. Atwater, Photonic design principles for ultrahigh-efficiency photovoltaics. *Nat Mater* **11**, 174-177 (2012).

183. J. Brivio, D. T. L. Alexander, A. Kis, Ripples and Layers in Ultrathin MoS2 Membranes. *Nano Letters* **11**, 5148-5153 (2011).

184. P. Miró, M. Ghorbani-Asl, T. Heine, Spontaneous Ripple Formation in MoS2 Monolayers: Electronic Structure and Transport Effects. *Advanced Materials* **25**, 5473-5475 (2013).

185. K. He, C. Poole, K. F. Mak, J. Shan, Experimental Demonstration of Continuous Electronic Structure Tuning via Strain in Atomically Thin MoS2. *Nano Letters* **13**, 2931-2936 (2013).

186. H. J. Conley *et al.*, Bandgap Engineering of Strained Monolayer and Bilayer MoS2. *Nano Letters* **13**, 3626-3630 (2013).

187. Y. Y. Hui *et al.*, Exceptional Tunability of Band Energy in a Compressively Strained Trilayer MoS2 Sheet. *ACS Nano* **7**, 7126-7131 (2013).

188. P. Gerd *et al.*, Control of biaxial strain in single-layer molybdenite using local thermal expansion of the substrate. *2D Materials* **2**, 015006 (2015).

189. X. Peng, Q. Wei, A. Copple, Strain-engineered direct-indirect band gap transition and its mechanism in two-dimensional phosphorene. *Physical Review B* **90**, 085402 (2014).

190. K. M. McCreary *et al.*, The Effect of Preparation Conditions on Raman and Photoluminescence of Monolayer WS2. *Scientific Reports* **6**, 35154 (2016).

191. S. J. Kim *et al.*, Large-Area Buckled MoS2 Films on the Graphene Substrate. *ACS Applied Materials & Interfaces* **8**, 13512-13519 (2016).

192. H. Li *et al.*, Optoelectronic crystal of artificial atoms in strain-textured molybdenum disulphide. *Nature Communications* **6**, 7381 (2015).

193. S. Deng, E. Gao, Z. Xu, V. Berry, Adhesion Energy of MoS2 Thin Films on Silicon-Based Substrates Determined via the Attributes of a Single MoS2 Wrinkle. *ACS Applied Materials & Interfaces* **9**, 7812-7818 (2017).

194. Y.-p. Miao, F. Ma, Y.-h. Huang, K.-w. Xu, Strain effects on electronic states and lattice vibration of monolayer MoS2. *Physica E: Low-dimensional Systems and Nanostructures* **71**, 1-6 (2015).

195. C. R. Zhu *et al.*, Strain tuning of optical emission energy and polarization in monolayer and bilayer MoS2. *Physical Review B* **88**, 121301 (2013).

196. C.-H. Chang, X. Fan, S.-H. Lin, J.-L. Kuo, Orbital analysis of electronic structure and phonon dispersion in MoS2, MoSe2, WS2, and WSe2 monolayers under strain. *Physical Review B* **88**, 195420 (2013).

197. Z. Yin *et al.*, Single-Layer MoS2 Phototransistors. *ACS Nano* **6**, 74-80 (2012).

198. T. Shen, A. V. Penumatcha, J. Appenzeller, Strain Engineering for Transition Metal Dichalcogenides Based Field Effect Transistors. *ACS Nano* **10**, 4712-4718 (2016).

199. T. Cheiwchanchamnangij, W. R. L. Lambrecht, Quasiparticle band structure calculation of monolayer, bilayer, and bulk MoS2. *Physical Review B* **85**, 205302 (2012).

200. T. Li, Ideal strength and phonon instability in single-layer MoS2. *Physical Review B* **85**, 235407 (2012).

201. P. Johari, V. B. Shenoy, Tuning the Electronic Properties of Semiconducting Transition Metal Dichalcogenides by Applying Mechanical Strains. *ACS Nano* **6**, 5449-5456 (2012).

202. E. Scalise, M. Houssa, G. Pourtois, V. Afanas'ev, A. Stesmans, Strain-induced semiconductor to metal transition in the two-dimensional honeycomb structure of MoS2. *Nano Res.* **5**, 43-48 (2012).

203. J. Feng, X. Qian, C.-W. Huang, J. Li, Strain-engineered artificial atom as a broad-spectrum solar energy funnel. *Nat Photon* **6**, 866-872 (2012).

204. M. Acerce, D. Voiry, M. Chhowalla, Metallic 1T phase MoS2 nanosheets as supercapacitor electrode materials. *Nat Nano* **10**, 313-318 (2015).

205. K.-A. N. Duerloo, Y. Li, E. J. Reed, Structural phase transitions in two-dimensional Mo- and W-dichalcogenide monolayers. *Nature Communications* **5**, 4214 (2014).

206. Y. Li, K.-A. N. Duerloo, K. Wauson, E. J. Reed, Structural semiconductor-to-semimetal phase transition in two-dimensional materials induced by electrostatic gating. *Nature Communications* **7**, 10671 (2016).

207. R. Kappera *et al.*, Phase-engineered low-resistance contacts for ultrathin MoS2 transistors. *Nat Mater* **13**, 1128-1134 (2014).

208. D. Voiry *et al.*, Enhanced catalytic activity in strained chemically exfoliated WS2 nanosheets for hydrogen evolution. *Nat Mater* **12**, 850-855 (2013).

209. H.-L. Tsai, J. Heising, J. L. Schindler, C. R. Kannewurf, M. G. Kanatzidis, Exfoliated−Restacked Phase of WS2. *Chem Mater* **9**, 879-882 (1997).

210. D. Voiry, A. Mohite, M. Chhowalla, Phase engineering of transition metal dichalcogenides. *Chemical Society Reviews* **44**, 2702-2712 (2015).

211. J. Berry, S. Zhou, J. Han, D. J. Srolovitz, M. P. Haataja, Dynamic Phase Engineering of Bendable Transition Metal Dichalcogenide Monolayers. *Nano Letters* **17**, 2473-2481 (2017).

212. S. Song *et al.*, Room Temperature Semiconductor–Metal Transition of MoTe2 Thin Films Engineered by Strain. *Nano Letters* **16**, 188-193 (2016).

213. P. V. Yudin, A. K. Tagantsev, Fundamentals of flexoelectricity in solids. *Nanotechnology* **24**, 432001 (2013).

214. W. Wu *et al.*, Piezoelectricity of single-atomic-layer MoS2 for energy conversion and piezotronics. *Nature* **514**, 470-474 (2014).

215. L. Kou, A. Du, C. Chen, T. Frauenheim, Strain engineering of selective chemical adsorption on monolayer MoS2. *Nanoscale* **6**, 5156-5161 (2014).

216. H. Li *et al.*, Activating and optimizing MoS2 basal planes for hydrogen evolution through the formation of strained sulphur vacancies. *Nat Mater* **15**, 48-53 (2016).

217. X. Chen, G. Wang, Tuning the hydrogen evolution activity of MS2 (M = Mo or Nb) monolayers by strain engineering. *Phys Chem Chem Phys* **18**, 9388-9395 (2016).

218. N. Muralidharan, R. Carter, L. Oakes, A. P. Cohn, C. L. Pint, Strain Engineering to Modify the Electrochemistry of Energy Storage Electrodes. *Scientific Reports* **6**, 27542 (2016).

219. Y. Wang, Y. Ding, Strain-induced self-doping in silicene and germanene from first-principles. *Solid State Communications* **155**, 6-11 (2013).

220. A. A. Kistanov, Y. Cai, K. Zhou, S. V. Dmitriev, Y.-W. Zhang, Large Electronic Anisotropy and Enhanced Chemical Activity of Highly Rippled Phosphorene. *The Journal of Physical Chemistry C* **120**, 6876-6884 (2016).

221. M. Hosseini, M. Elahi, M. Pourfath, D. Esseni, Strain-Induced Modulation of Electron Mobility in Single-Layer Transition Metal Dichalcogenides MX2 (M = Mo, W; X = S, Se). *Ieee T Electron Dev* **62**, 3192-3198 (2015).

222. H. Manouchehr, E. Mohammad, P. Mahdi, E. David, Strain induced mobility modulation in single-layer MoS 2. *Journal of Physics D: Applied Physics* **48**, 375104 (2015).

223. H. Li *et al.*, Optoelectronic crystal of artificial atoms in strain-textured molybdenum disulphide. *Nat Commun* **6**, (2015).

224. S.-J. Yu *et al.*, Stress relief patterns of Co films deposited on circular silicone oil substrates. *Thin Solid Films* **520**, 5683-5690 (2012).

225. S. Conti, A. DeSimone, S. Müller, Self-similar folding patterns and energy scaling in compressed elastic sheets. *Computer Methods in Applied Mechanics and Engineering* **194**, 2534-2549 (2005).

226. C. M. Stafford *et al.*, A buckling-based metrology for measuring the elastic moduli of polymeric thin films. *Nat Mater* **3**, 545-550 (2004).

227. E. Cerda, K. Ravi-Chandar, L. Mahadevan, Thin films: Wrinkling of an elastic sheet under tension. *Nature* **419**, 579-580 (2002).

228. Z. H. Aitken, R. Huang, Effects of mismatch strain and substrate surface corrugation on morphology of supported monolayer graphene. *Journal of Applied Physics* **107**, 123531 (2010).

229. J. E. Castle, P. A. Zhdan, Characterization of surface topography by SEM and SFM: problems and solutions. *Journal of Physics D: Applied Physics* **30**, 722 (1997).

230. A. A. Volinsky, N. R. Moody, W. W. Gerberich, Interfacial toughness measurements for thin films on substrates. *Acta Materialia* **50**, 441-466 (2002).

231. A. P. S. Gaur *et al.*, Surface Energy Engineering for Tunable Wettability through Controlled Synthesis of MoS2. *Nano Letters* **14**, 4314-4321 (2014).

232. S. Wang *et al.*, Mechanics of curvilinear electronics. *Soft Matter* **6**, 5757-5763 (2010).

233. V. Berry, R. F. Saraf, Self-Assembly of Nanoparticles on Live Bacterium: An Avenue to Fabricate Electronic Devices. *Angewandte Chemie International Edition* **44**, 6668-6673 (2005).

234. I. R. McFarlane, J. R. Lazzari-Dean, M. Y. El-Naggar, Field effect transistors based on semiconductive microbially synthesized chalcogenide nanofibers. *Acta Biomaterialia* **13**, 364-373 (2015).

235. P. Nguyen, V. Berry, Graphene Interfaced with Biological Cells: Opportunities and Challenges. *The Journal of Physical Chemistry Letters* **3**, 1024-1029 (2012).

236. T. S. Sreeprasad *et al.*, Graphene Quantum Dots Interfaced with Single Bacterial Spore for Bio-Electromechanical Devices: A Graphene Cytobot. *Sci. Rep.* **5**, (2015).

237. T. Cohen-Karni, Q. Qing, Q. Li, Y. Fang, C. M. Lieber, Graphene and Nanowire Transistors for Cellular Interfaces and Electrical Recording. *Nano Letters* **10**, 1098-1102 (2010).

238. J. Janata, Graphene Bio-Field-Effect Transistor Myth. *ECS Solid State Letters* **1**, M29-M31 (2012).

239. G. J. Tortora, B. R. Funke, C. L. Case, *Microbiology: An Introduction*. (Pearson Education, 2016).

240. B. Andreea Irina, S. Iuliana, H. Camelia. (2012).

241. Z. H. Ni *et al.*, Uniaxial Strain on Graphene: Raman Spectroscopy Study and Band-Gap Opening. *ACS Nano* **2**, 2301-2305 (2008).

242. N. Melanitis, P. L. Tetlow, C. Galiotis, Characterization of PAN-based carbon fibres with laser Raman spectroscopy. *J Mater Sci* **31**, 851-860 (1996).

243. J. E. Lee, G. Ahn, J. Shim, Y. S. Lee, S. Ryu, Optical separation of mechanical strain from charge doping in graphene. *Nat Commun* **3**, 1024 (2012).

244. S. Reich, H. Jantoljak, C. Thomsen, Shear strain in carbon nanotubes under hydrostatic pressure. *Physical Review B* **61**, R13389-R13392 (2000).

245. Y. H. An, R. J. Friedman, Concise review of mechanisms of bacterial adhesion to biomaterial surfaces. *Journal of Biomedical Materials Research* **43**, 338-348 (1998).

246. E. Cerda, L. Mahadevan, Geometry and Physics of Wrinkling. *Physical Review Letters* **90**, 074302 (2003).

247. V. Berry, Impermeability of graphene and its applications. *Carbon* **62**, 1-10 (2013).

248. N. Mohanty *et al.*, Nanotomy-based production of transferable and dispersible graphene nanostructures of controlled shape and size. *Nat Commun* **3**, 844 (2012).

249. P. K. Schelling, P. Keblinski, Thermal expansion of carbon structures. *Physical Review B* **68**, 035425 (2003).

250. A. Castellanos-Gomez, H. S. J. van der Zant, G. A. Steele, Folded MoS2 layers with reduced interlayer coupling. *Nano Res.* **7**, 572-578 (2014).

251. H.-P. Komsa, A. V. Krasheninnikov, Effects of confinement and environment on the electronic structure and exciton binding energy of MoS${}_{2}$ from first principles. *Physical Review B* **86**, 241201 (2012).

252. L. Yang *et al.*, Chloride Molecular Doping Technique on 2D Materials: WS2 and MoS2. *Nano Letters* **14**, 6275-6280 (2014).

253. C.-C. Wu *et al.*, Elucidating the Photoresponse of Ultrathin MoS2 Field-Effect Transistors by Scanning Photocurrent Microscopy. *The Journal of Physical Chemistry Letters* **4**, 2508-2513 (2013).

254. Y. Ge, W. Wan, W. Feng, D. Xiao, Y. Yao, Effect of doping and strain modulations on electron transport in monolayer MoS2. *Physical Review B* **90**, 035414 (2014).

255. K. Kaasbjerg, K. S. Thygesen, K. W. Jacobsen, Phonon-limited mobility in n-type single-layer MoS${}_{2}$ from first principles. *Physical Review B* **85**, 115317 (2012).

256. B. Chakraborty *et al.*, Symmetry-dependent phonon renormalization in monolayer MoS${}_{2}$ transistor. *Physical Review B* **85**, 161403 (2012).

257. K. F. Mak *et al.*, Tightly bound trions in monolayer MoS2. *Nat Mater* **12**, 207-211 (2013).

258. X. Cui *et al.*, Multi-terminal transport measurements of MoS2 using a van der Waals heterostructure device platform. *Nat Nano* **10**, 534-540 (2015).

259. B. Radisavljevic, A. Kis, Mobility engineering and a metal–insulator transition in monolayer MoS2. *Nat Mater* **12**, 815-820 (2013).

260. G. Lan, C. W. Wolgemuth, S. X. Sun, Z-ring force and cell shape during division in rod-like bacteria. *Proceedings of the National Academy of Sciences* **104**, 16110-16115 (2007).

261. D. R. Khanal, J. Wu, Gate Coupling and Charge Distribution in Nanowire Field Effect Transistors. *Nano Letters* **7**, 2778-2783 (2007).

262. E. Lind, A. I. Persson, L. Samuelson, L.-E. Wernersson, Improved Subthreshold Slope in an InAs Nanowire Heterostructure Field-Effect Transistor. *Nano Letters* **6**, 1842-1846 (2006).

7. APPENDIX

7.1 Bacteria-induced wrinkles in graphene

Poisson's ratio for most materials ranges between 0 and 0.5 (under a small strain, a perfectly incompressible material deformed elastically can be described as Poisson's ratio equals to 0.5). We used the semi-rigid cell wall with Poisson's ratio value of 0.25. As the volume of the bacterial cell reduces, so does the surface area and the transverse diameter of graphene-on-bacteria. Therefore,

$$S = (1 + (1 + \varepsilon)^3)/2(1 + \varepsilon) \quad \text{(A1)}$$

From FESEM image analysis, $S = 2.657$. The value of ε determined from the diameter obtained from FESEM and the height from AFM is 1.219. The experimental average wrinkle-wavelength from the FESEM and AFM micrographs (32.4 and 34.3 nm, respectively commensurate with simulations (34 nm); thus underpinning the intimate contact between graphene and bacteria. Combining Equation (22) and experimental wavelengths, we estimate the Young's modulus of bacterial cell wall to be between 35.7 and 42.2 MPa, consistent with other measurements (39 MPa(*260*)). Therefore, studying the wrinkling of interfaced 2DNs may be route to determine the mechanical properties of bacteria. Further, we calculate the average amplitude of wrinkles as $A = w_{max} = 7.3$ nm from Equation (22), consistent with AFM measurements (10 nm). The maximum perpendicular stress (p_{max}) acting on graphene is 40.18 MPa. Based on AFM data:

Average height of graphene covered bacteria before vacuum: $H = 0.279$ μm

Average height of graphene covered bacteria after vacuum: $h = 0.186$ μm

Average weight of wrinkles region D_C = 1.1 μm

$R_C{}^2 = (R_C - D_C)^2 + (\frac{D_C}{2})^2$

$R_C = 0.682$ μm

Arcsine $(\frac{D_C}{2R})$ = 0.938 R

Length of curve before vacuum: $L_C = 2\times0.938\times0.682 = 1.513$ μm

Average width of wrinkles region D_w = 0.628 μm

Pythagorean Theorem: $R_W{}^2 = (R_W - D_w)^2 + (\frac{D_w}{2})^2$

$R_W = 0.358$ μm

Arcsine $(\frac{D_w}{2R})$ = 1.069 R

The length of the curve after vacuum: $L_W = 2\times1.069\times0.358 = 0.765$ μm

The compressive strain in the graphene film along the relaxed direction: ε_0

and $\varepsilon_g = (L_C - L_w)/L_C$, as $L_C = 1.513$ μm $\quad and \quad$ $L_w = 0.765$ μm

So: $\varepsilon_g = 0.494$

The strain of the substrate: ε

$\varepsilon_g = \varepsilon/(\varepsilon + 1)$

$\varepsilon = \frac{\varepsilon_g}{1-\varepsilon_g} = 0.977$

λ is the stretch of bacteria substrate after vacuum compare to before vacuum

So: $\varepsilon = \lambda - 1$

Pre-stretch factor:$S = \Lambda = \frac{1}{2}\lambda^{\frac{1}{2}}\left(1+\lambda^{\frac{3}{2}}\right) = \frac{1}{2}(1+\varepsilon)^{\frac{1}{2}}\left(1+(1+\varepsilon)^{\frac{3}{2}}\right) = 2.657$

$E_g = 1TPa$, $v_g = 0.165$

Plane-strain modulus: $\bar{E} = E/(1-v^2)$

We approximated the semi-rigid cell wall with Poisson's ratio value of 0.25. As the volume of the bacterial cell reduces, so does the surface area and the transverse diameter of graphene-on-bacteria.

Plane-strain modulus of the graphene film: $\bar{E}_g = \frac{E_g}{1-{v_g}^2} = \frac{10^{12}}{1-0.165^2} = 1.028\times10^{12}$

t is the thickness of the graphene: t = 0.355 nm

We have the wavelength modulus related equation: $\lambda = 2\pi t(\frac{\bar{\bar{E}}_g}{3S\bar{E}_B})^{1/3}$

$E_B = \bar{E}_B\times(1-{v_B}^2) = \left(\frac{\lambda}{2\pi t}\right)^{-3}\times\frac{\bar{E}_g}{3S}$

Since the wavelength we get from FESEM and AFM is 32.4 and 34.3 nm respectively. The range of E_B is 35.74 t0 42.40Mpa.

Average length of bacteria: L = 2.478 μm

Effective wavelength of wrinkles: $\bar{L} = \frac{L}{3} = 0.826$ μm

We have the wavelength modulus related equation: $A = \frac{\bar{L}t}{\lambda}\left(\frac{8v}{3(1-v)^2}\right)^{1/2}$

So we have: $A = \frac{\bar{\bar{L}}t}{\lambda}\left(\frac{8v}{3(1-v)^2}\right)^{1/2} =$ 7.279 nm ≅ 7.3 nm

The linearization of pre-buckling state in classical buckling analysis showed:

$$\mathrm{D}\nabla^4 w + \sigma_0 t\nabla^2 w = -p$$

D is the bending stiffness of the plate with $\mathrm{D} = \mathrm{E}t^3/[12(1-v^2)]$, ∇^4 is the bi-harmonic operator, and σ_0 is the compressive equi-biaxial pre-stress.

The periodic solution of this linearization and the exact solution for the normal deflection of the surface in classical buckling model based on von Karman plate equations gives the following periodic relationship:

The maximum perpendicular stress: $w = 2p/(\bar{\bar{E}}_S k)$ (in magnitude) and k is wave number and is equal to $2\pi/\lambda$.

At $w \approx A$

$$p_{max} \sim \frac{w_{max}\bar{\bar{E}}_S}{2t\left(\frac{\bar{\bar{E}}_g}{3S\bar{\bar{E}}_S}\right)^{1/3}} = \frac{10\times 39\times 10^6}{2\times 0.355\times(1-0.25^2)\times 2.657\times\left(\frac{1.028\times 10^{12}}{3\times 4.160\times 10^7}\right)^{1/3}} = 40.18\ Mpa$$

Where w is the perpendicular displacement of the graphene, *P* is the stress component by the bacterial cell wall acting perpendicularly on graphene.

The young's modulus of the cell membrane was estimated on the order of 1000 Pa. So the range of wavelength of wrinkles formatted on bacterial cell wall is 2738.08 nm (at 10000 Pa) to 5903.2 nm (at 1000 Pa).

($\lambda = 2\pi t\left(\frac{\bar{\bar{E}}_B}{3S\bar{\bar{E}}_{Cell\ membrane}}\right)^{1/3}$)

The wavelength on raisin: $\lambda = 2\pi t(\frac{\bar{\bar{E}}_g}{3\bar{E}_B})^{1/3} = 2\pi \times 0.1mm \times (\frac{30}{3})^{1/3} = 1.354\ mm$

Table A1. Calculation of wrinkle wavelength form FESEM results

Number of Peak on each line								
Line	**Bacteria1**	**Bacteria2**	**Bacteria3**	**Bacteria4**	**Bacteria5**	**Bacteria6**	**Bacteria7**	**Bacteria8**
1	22	20	17	23	17	18	16	22
2	23	19	17	17	18	16	20	21
3	26	19	19	24	16	17	21	25
4	22	18	16	21	17	18	18	22
5	22	21	17	19	16	16	16	22
6	24	17	16	18	17	18	17	20
7	22	22	17	23	18	18	19	19
8	23	19	16	22	20	20	20	18
9	21	19	19	20	20	18	19	20
10	22	19	21	21	19	22	17	17
11	25	19	17	19	21	17	19	18
12	21	20	17	19	21	17	20	18
13	24	22	18	18	21	20	22	20

14	23	18	18	17	21	18	21	20
15	22	20	18	20	22	20	18	18
Average	22.800	19.467	17.533	20.067	18.933	18.200	18.867	20.000

Table A2. Average wavelength in AFM image

Number of Peak Each Range					
Range/nm	**200-400**	**400-600**	**600-800**	**800-1000**	
Line 1	6	6	6	4	36.364
Line 2	5	6	6	5	36.364
Line 3	6	6	5	5	36.364
Line 4	7	6	6	6	32.000
Line 5	5	6	6	6	34.783
Line 6	7	5	6	6	33.333
Line 7	5	6	7	5	34.783
Line 8	7	6	6	7	30.769

Table A3. Wrinkles wavelength (λ) versus diameters of bacteria (D_B)

	1	2	3	4	5	6	7	8
Diameter of Bacteria (D_B)/μm	0.936	0.897	0.909	0.953	0.926	0.924	0.834	1.034
Diameter of Wrinkles (D_w)/ μm	0.652	0.621	0.661	0.621	0.603	0.593	0.566	0.710
D_w/D_B	0.696	0.692	0.727	0.652	0.652	0.642	0.678	0.687
Wavelengths (λ/ μm)	0.029	0.032	0.038	0.031	0.032	0.033	0.030	0.036

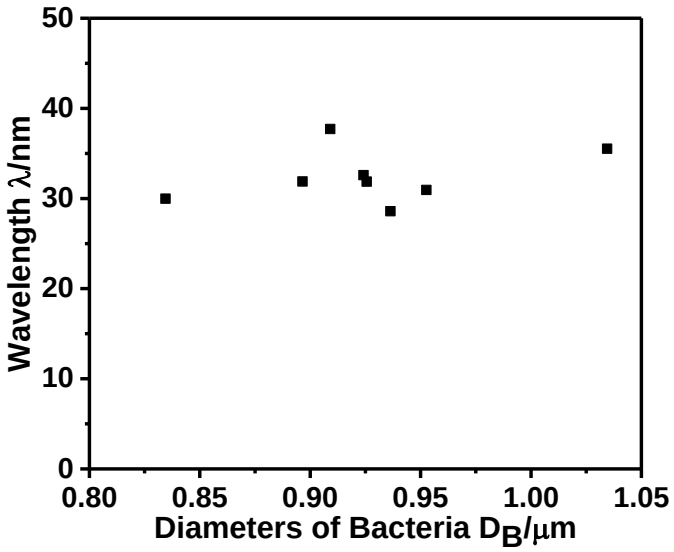

Figure A1. Wrinkles wavelength (λ) versus size of bacteria (diameters of bacteria D_B).

7.2 Wrinkled MoS_2 calculation

The mobility in flat devices:

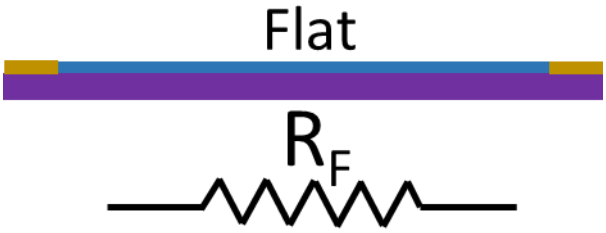

$V_{DS} = 1V$

$I_F = I_0$

$$\mu_F = \frac{L}{W\left(\frac{\varepsilon_{sio2}\varepsilon_0}{D}\right)V_{DS}}\frac{dI_{DS}}{dV_{BG}} = \frac{20}{20\left(\frac{3.9\times8.854\times10^{-12}}{285\times10^{-9}}\right)1}\times12.466\times10^{-9}\times10^{4}$$

$$= 1.029\ \ \mathrm{cm^2V^{-1}S^{-1}}$$

The mobility in wrinkled MoS_2:

The resistant of flat parts (R_{F1} and R_{F2}) in wrinkled device compared to the resistance of flat device:

$$R = \frac{L}{ne\mu A} \tag{29}$$

Assume the flat parts of MoS_2 and MoS_2 in flat devices have same (n, μ and A), also $L_{F1} + L_{F2} = 0.8\,L_F$, so we have:

$$\frac{R_{F1} + R_{F2}}{R_F} = \frac{0.8}{1}$$

Combine the current relationship in two kinds of devices ($I_F = 10I_W$ under $V_{DS} = 1V$ at 300K), so the voltage drops of wrinkled part (R_W) is: $\Delta V_W = V_{DS} - 0.8\times0.05 = 0.96V$;

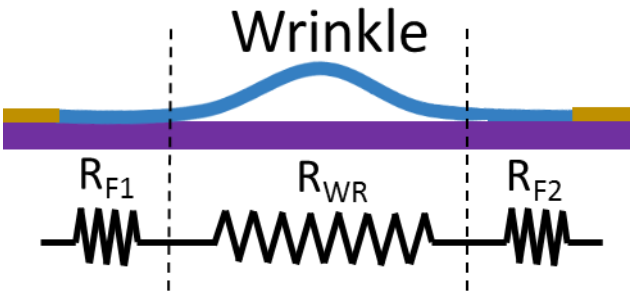

$V_{DS} = 1V$

$I_W = 0.05I_0$

We can apply different models to calculate the capacitance of the gate in the wrinkled MoS_2 devices:

(1) Considering the wrinkled parts as two dielectric layers in series (parallel-plate capacitor model : 285 nm of SiO_2 and averaged 300 nm of air):

$$\mu_W = \frac{L_W}{W\left(\frac{1}{\frac{1}{\frac{\varepsilon_{sio2}\varepsilon_0}{D_{Sio2}}}+\frac{1}{\frac{\varepsilon_{air}\varepsilon_0}{D_{air}}}}\right)\Delta V_W}\frac{dI_{DS}}{dV_{BG}} = \frac{4}{20\left(\frac{1}{\frac{1}{\frac{3.9\times8.854\times10^{-12}}{285\times10^{-9}}}+\frac{1}{\frac{1\times8.854\times10^{-12}}{300\times10^{-9}}}}\right)0.955}\times16.588\times10^{-9}\times10^{4}$$

$= 1.464\ \mathrm{cm^2V^{-1}S^{-1}}$

So $\mu_W \approx 1.4\,\mu_F$

(2) Considering the wrinkled MoS_2 as a cylinder on a conducting plate:(*261, 262*)

$$\mu_W = \frac{2L_W W}{\Delta V_W C_g}\frac{dI_{DS}}{dV_{BG}} \quad (30)$$

Where L_W is the length of the wrinkle, and $2L_W$ is the wrinkled affect length, W is the width of the channel, C_g is the capacitance of the gate.

Back gate capacitance per unit length in this cylinder on a plate model:

$$\frac{C_g}{W} = \frac{2\pi\varepsilon_{ox}\varepsilon_0}{cosh^{-1}(\frac{r+h}{r})} \quad (31)$$

where r is the wrinkles radius (300 nm), h is the SiO_2 thickness (285 nm), and ε_{ox} is the SiO_2 dielectric constant (ε_{ox}= 3.9).

$$\mu_W = \frac{L_W}{\Delta V_W \frac{2\pi\varepsilon_{ox}\varepsilon_0}{cosh^{-1}\left(\frac{r+h}{r}\right)}} \frac{dI_{DS}}{dV_{BG}} = \frac{4\times10^{-6}}{0.96\times\frac{2\pi\times3.9\times8.854\times10^{-12}}{cosh^{-1}\left(\frac{300+285}{285}\right)}} \times 16.588\times10^{-9}\times10^{4} =$$

$$16.741\ \mathrm{cm^2V^{-1}S^{-1}} = 16.741\ \mathrm{cm^2V^{-1}S^{-1}}$$

$\mu_W \approx 16.3\ \mu_F$

Therefore: $\mu_W \approx\ (1.4 \sim 16.3)\ \mu_F$

Table A4. Photoluminescence versus deformation

Wavelength (nm)	**Thickness (nm)**	**Projection Length (nm)**	**Deformation (%)**	**PL Shift (meV)**	**PL Shift /Deformation (meV/%)**
1157	13.9	10000	0.55	33.9	61.4
629	10.1	3620	0.63	30	47.0
526	10.6	3620	0.32	19.1	59.1
2082	19.8	30000	0.37	20	53.9
385	10	998	0.54	27.8	50.8

2206	21	10000	1.11	47.6	42.9
721	10.5	5788	0.37	25.8	48.2

Table A5. Temperature study for activitation energy in MoS_2

T	**1/kT**	**R_F**	**R_W**	**Ln(R_F)**	**Ln(R_W)**
K	$(eV)^{-1}$	Ω	Ω		
15	773.6348343	989728.2641	12454700000	14.85650492	23.2453639
60	193.4087086	453025.3623	--	13.75627543	--
100	116.0452251	285250.6702	1559388100	13.19497065	21.16755934
150	77.36348343	220696.3506	109318000	12.81717505	18.50977162
200	58.02261257	180294.8917	37743500	12.46423667	17.44632383
250	46.41809006	145240.1696	8082200	12.09480529	15.90517467
300	38.68174172	114055.0526	2224000	11.70528729	14.61481793

Title:	Wrinkled, rippled and crumpled graphene: an overview of formation mechanism, electronic properties, and applications
Author:	Shikai Deng,Vikas Berry
Publication:	Materials Today
Publisher:	Elsevier
Date:	May 2016

RightsLink®

Home | Create Account | Help

Title:	Confined, Oriented, and Electrically Anisotropic Graphene Wrinkles on Bacteria
Author:	Shikai Deng, Enlai Gao, Yanlei Wang, et al
Publication:	ACS Nano
Publisher:	American Chemical Society
Date:	Sep 1, 2016

LOGIN

If you're a copyright.com user, you can login to RightsLink using your copyright.com credentials. Already **a RightsLink user** or want to learn more?

PERMISSION/LICENSE IS GRANTED FOR YOUR ORDER AT NO CHARGE

This type of permission/license, instead of the standard Terms & Conditions, is sent to you because no fee is being charged for your order. Please note the following:

- Permission is granted for your request in both print and electronic formats, and translations.
- If figures and/or tables were requested, they may be adapted or used in part.
- Please print this page for your records and send a copy of it to your publisher/graduate school.
- Appropriate credit for the requested material should be given as follows: "Reprinted (adapted) with permission from (COMPLETE REFERENCE CITATION). Copyright (YEAR) American Chemical Society." Insert appropriate information in place of the capitalized words.
- One-time permission is granted only for the use specified in your request. No additional uses are granted (such as derivative works or other editions). For any other uses, please submit a new request.

BACK | CLOSE WINDOW

Title: Increased Hierarchical Wrinklons on Stiff Metal Thin Film on a Liquid Meniscus

Author: Shikai Deng, Vikas Berry

Publication: Applied Materials

Publisher: American Chemical Society

Date: Sep 1, 2016

PERMISSION/LICENSE IS GRANTED FOR YOUR ORDER AT NO CHARGE

This type of permission/license, instead of the standard Terms & Conditions, is sent to you because no fee is being charged for your order. Please note the following:

- Permission is granted for your request in both print and electronic formats, and translations.
- If figures and/or tables were requested, they may be adapted or used in part.
- Please print this page for your records and send a copy of it to your publisher/graduate school.
- Appropriate credit for the requested material should be given as follows: "Reprinted (adapted) with permission from (COMPLETE REFERENCE CITATION). Copyright (YEAR) American Chemical Society." Insert appropriate information in place of the capitalized words.
- One-time permission is granted only for the use specified in your request. No additional uses are granted (such as derivative works or other editions). For any other uses, please submit a new request.

Title: Adhesion Energy of MoS2 Thin Films on Silicon-Based Substrates Determined via the Attributes of a Single MoS2 Wrinkle

Author: Shikai Deng, Enlai Gao, Zhiping Xu, et al

Publication: Applied Materials

Publisher: American Chemical Society

Date: Mar 1, 2017

PERMISSION/LICENSE IS GRANTED FOR YOUR ORDER AT NO CHARGE

This type of permission/license, instead of the standard Terms & Conditions, is sent to you because no fee is being charged for your order. Please note the following:

- Permission is granted for your request in both print and electronic formats, and translations.
- If figures and/or tables were requested, they may be adapted or used in part.
- Please print this page for your records and send a copy of it to your publisher/graduate school.
- Appropriate credit for the requested material should be given as follows: "Reprinted (adapted) with permission from (COMPLETE REFERENCE CITATION). Copyright (YEAR) American Chemical Society." Insert appropriate information in place of the capitalized words.
- One-time permission is granted only for the use specified in your request. No additional uses are granted (such as derivative works or other editions). For any other uses, please submit a new request.

BACK CLOSE WINDOW

VITA

Education

Ph.D. Candidate in Chemical Engineering, GPA: 4.0/4.0 Advisor: Dr. Vikas Berry

University of Illinois at Chicago (UIC), Chicago, IL Aug, 2014 - Present

(Kansas State University (KSU), Manhattan, KS Aug, 2012 - Aug, 2014)

B.E. in Chemical Engineering, Beijing University of Chemical Technology (BUCT), Beijing, China Jun, 2012

Honors & Awards

Argonne National Laboratory Graduate Research Program 2017

Invited Reviewer for Carbon 2017

UIC Provost's Award for Graduate Research 2016

UIC Graduate College Student Presenter's Award 2016

UIC GSC Travel Award 2015

Invited Reviewer for Scientific Report (Nature Publishing Group) 2015, 2016

Invited Reviewer for MRS Advances 2015

Borouge Scholarship (9 out of 285) 2011

Award for Outstanding Student of BUCT (1 out of 32) (Twice) 2009, 2011

People's Scholarship (Top 5%) (Four Times) 2009 - 2011

Publications

1. Shikai Deng, Enlai Gao, Zhiping Xu and Vikas Berry, "Direct Measurement of Adhesion Energy of MoS2 Thin Film on Solid Surfaces through Wrinkled MoS2", ACS Appl. Mater. Interfaces, 2017, 9, 7812–7818.

2. Shikai Deng, Enlai Gao, Yanlei Wang, Soumyo Sen, T. S. Sreeprasad, Sanjay Behura, Petr Král, Zhiping Xu, and Vikas Berry, "Confined, Oriented, and Electrically Anisotropic Graphene Wrinkles on Bacteria", ACS Nano, 2016, 10, 8403–8412. (Research featured in The Economist, Science Daily, AZONano, The Engineer, The Microbe and several others)

3. Shikai Deng and Vikas Berry, "Increased Hierarchical Wrinklons on Stiff Metal Thin Film on a Liquid Meniscus", ACS Appl. Mater. Interfaces, 2016, 8, 24956−24961.

4. Shikai Deng and Vikas Berry, "Wrinkled, Rippled and Crumpled Graphene: An Overview of Formation Mechanism, Electronic Properties, and Applications", Materials Today, 2016, 19, 197−212.

5. Donovan Briggs, Shikai Deng and Vikas Berry, "Wrinkling Graphene and Functionalization of MoS2 for Electronic Applications", ECS Transactions, 2014, 64, 479−489.

6. S. Behura, K. Chang, Y. Wen, R. Debbarma, P. Nguyen, S. Che, S. Deng, M. Seacrist and V. Berry, "Photovoltaic and spectral response of WS2/silicon heterojunction solar cells," IEEE Nanotechnology Magazine, 2017.

7. Shikai Deng and Vikas Berry, ” Wrinkled MoS_2 Field-Effect Transistor: Strain and Doping Variation Induced Photo-response Enhancement”, Submitted.

8. Shikai Deng, Anirudha V. Sumant, and Vikas Berry, ” Strain Engineering In Two-Dimensional Nanomaterials Beyond Graphene”, Submitted.

Disclosure

“Nano-scale Graphene Check Valve”, Shikai Deng and Vikas Berry, UIC Research Disclosure 2016-036.

Research Experience

Research Assistant, UIC & KSU Aug, 2012 - Dec,2017

Graduate Research Program, Argonne National Laboratory Feb, 2017 - Dec,2017

Teaching Experience

Teaching Assistant, UIC & KSU Aug, 2012 - Dec, 2016

Selected Presentations

1. “Wrinkled MoS2 Field-Effect Transistors”, 2016 MRS Fall Meeting & Exhibit, Oral Presentation, Boston, MA, December 2016

2. “Confined, Oriented and Electrically Anisotropic Graphene Wrinkles on Bacteria”, 2016 MRS Fall Meeting & Exhibit, Poster Presentation, Boston, MA, December 2016

3. “Electrical Properties of Controlled, Longitudinal Wrinkles on Graphene Produced”, 2015 MRS Fall Meeting & Exhibit, Oral Presentation, Boston, MA, December 2015

4., “Electrical Properties of Controlled, Longitudinal Wrinkles on Graphene Produced”, Oral Presentation, 2015 MRS Fall Meeting & Exhibit, Boston, MA, December 2015

5. “Electrical Properties of Controlled, Longitudinal Wrinkles on Graphene Produced via Bacterial-Scaffold Shrinkage”, 2015 Postdoctoral Research Symposium, Poster Presentation, Argonne, IL, October 2015

6. “Longitudinal Wrinkles on Graphene Produced via Bacterial-Scaffold Shrinkage”, 227th ECS Meeting, Oral Presentation, Chicago, IL, May 2015

7. “Longitudinal Wrinkles on Graphene Produced via Bacterial-Scaffold Shrinkage”, 2015 UIC Research Forum, Poster Presentation, UIC, April 2015

8. “Electronic control via precise wrinkling of graphene with bacterial cells”, 2014 MRS Spring Meeting & Exhibit, Poster Presentation, San Francisco, CA, April 2014